DESIGN AND DEVELOPMENT OF A SYNERGETIC CONTROLLER FOR A PERMANENT MAGNET SYNCHRONOUS MOTOR DRIVE SYSTEM

by

Andrew Ayman Adib

Thesis Proposal
A Thesis Presented to the Faculty of the
American University of Sharjah
College of Engineering
in Partial Fulfillment
of the Requirements
for the Degree of

Master of Science in
Mechatronics Engineering

Sharjah, United Arab Emirates

December 2017

Approval Signatures

We, the undersigned, approve the Master's Thesis of Andrew Ayman Adib.

Thesis Title: Design and Development of a Synergetic Controller for a Permanent Magnet Synchronous Motor Drive System.

Signature	**Date of Signature** (dd/mm/yyyy)
_____	_____
Dr. Rached Bin H'mida Dhaouadi Professor, Department of Mechatronics Engineering Thesis Advisor	
_____	_____
Dr. Shayok Mukhopadhyay Assistant Professor, Department of Mechatronics Engineering Thesis Committee Member	
_____	_____
Dr. Habibur Rehman Associate Professor, Department of Electrical Engineering Thesis Committee Member	
_____	_____
Dr. Lotfi Romdhane Head, Department of Mechatronics Engineering	
_____	_____
Dr. Ghaleb Husseini Associate Dean for Graduate Affairs and Research College of Engineering	
_____	_____
Dr. Richard T. Schoephoerster Dean, College of Engineering	
_____	_____
Dr. Mohamed El-Tarhuni Vice Provost for Graduate Studies	

Acknowledgements

Firstly, I would like to start off with how grateful I am for my family whom I would not have been able to complete this study without their support and sacrifices. They have looked after me and my best interests every single day of my life. For that, it is always my goal to make them proud. I would also like to thank my thesis advisor, Dr. Rached Dhaouadi, for his guidance, support and advice throughout this journey. Moreover, I would like to offer my sincere gratitude for the College of Engineering and the Graduate Program for giving me the opportunity to complete this study by funding my research and offering me the graduate teaching assistantship. In addition, I would like to thank our lab engineer, Mr. Kent Roferos, for his assistance in the lab. My thanks also go to my best friend, Nour Ghaly, for her constant support and encouragement from the very first day. Finally, I would like to thank my friends Aly, Adil, Daniyal and all the people I met throughout the course of these two years for making this journey unforgettable.

Dedicated to the Lord . . .

Abstract

Electric vehicles are gaining increasing attention by automotive manufacturers in an attempt to reduce carbon footprint and produce more eco-friendly vehicles. Electric vehicles are powered by electric motor drives instead of the conventional combustion engine. Permanent Magnet Synchronous Motor (PMSM) drives receive most interest in this field for their powerful torque profiles that are suitable for vehicle traction. This study explores a new non-linear controller, the synergetic controller, and evaluates its performance in motor drives applications and particularly for the PMSM. Firstly, the new controller is presented and the controller design is explained. A new macro-variable is proposed to improve the performance of the controller. The effect of each of the controller's gains is studied separately. Finally, the controller's performance is compared with the field oriented controller, which is the most robust and reliable control technique in motor drives applications. This work also investigates the regenerative braking phenomenon in PMSM. Regenerative braking is crucial for electric vehicle applications since the mechanical energy of the motor during deceleration or braking periods can be harvested and used to charge the vehicle's battery or a proper energy storage unit designed for such purpose. Regenerative braking is implemented using two techniques; speed control and torque control. The different algorithms are validated through experiments using a PMSM drive system developed in the Mechatronics (MTR) lab. The experimental results show that the proposed macro-variable improves the performance of the synergetic controller significantly. The synergetic controller is able to overcome non-linearities in the system, such as static friction, faster than the field oriented controller. The system also experiences fewer harmonics under the synergetic controller. Synergetic controller is also more prone to wide signal variations. As for regenerative braking, the speed control mode of operation is suitable for harvesting more energy. On the other hand, the torque control mode generates more power and higher current values flow back to the DC source. Synergetic controller improves the performance of the PMSM drive.

Search Terms: ***Permanent Magnet Synchronous Motor, Field Oriented Control, Synergetic Control, SPWM, Regenerative Braking***

Table of Contents

List of Figures

List of Tables

Chapter 1: Introduction and Literature Review

Alternating Current (AC) motor drives are used in several industrial applications, such as electric vehicles (EV), industrial drives, military applications and aviation. These motors are known for their rugged constant speed and high-power density performances. They are also not affected by environmental factors. These are all limitations of the previously used Direct Current (DC) motor drives [1]. There are multiple motor drives technologies available in the market; for instance, induction machines (IM), permanent magnet synchronous machines (PMSM) and switched reluctance machines (SRM). For electric vehicle purposes, manufacturers seek a motor drive that is capable of providing a high overall efficiency within a large range of torque-speed characteristics, high overload capacity, compact space and weight and, of course, low cost in production [2]. Studies show that the demand on IM and PMSM for electric and hybrid electric vehicles (HEV) is the highest among other motor drives. They also indicate that the demand on DC motors is decreasing, and SRM are gaining more interest [3–6]. Studying the advantages and disadvantages of each motor, the IM and PMSM compete over which motor is most suitable for HEV applications. SRM follow the previously mentioned motors, and the DC motor trails at the end as the least suitable motor drive for such applications. IM with squirrel-cage is also known for its compact size that is very convenient for HEV applications. It provides a wide speed range with good efficiencies due to low magnetization current in the range of field weakening. However, at higher nominal speeds, these magnetization currents and copper losses in the rotor decrease the efficiency of the motor [3]. With the increase in losses, the rotor heats up and thus requires cooling systems. This will in turn increase the cost. It also requires smaller air gaps to decrease the magnetization current which will also increase production costs. PMSM are excited by permanent magnets fixed on the rotor, which allows the machine to have a high energy density. Without the need for excitation current, PMSM provide less losses and higher efficiencies for a given nominal speed. Losses in PMSM are exhibited in iron losses in the stator. Therefore, PMSM provide higher power density and efficiency than IM. Another advantage of PMSM is their smaller volumes and lesser weights for a given power density level.

However, PMSM have some disadvantages. One of their main drawbacks is the expensive rare-earth magnets used in their structure which increases the cost of these machines. Another disadvantage is the demagnetization of the permanent magnet which is caused by over-heating the magnet and high stator currents which can be caused by field weakening. Therefore, PMSM are highly restrictive when considering field weakening; this does not give much room for overloading the machine and extending its speed ranges. On the other hand, SRM are gaining more interest with the development of power electronics. They are widely known for their rugged constructions that allow for better thermal characteristics, cost efficiency and low maintenance. SRM are also characterized by their long constant-power range. However, these motors also have a number of disadvantages that prevent them from competing with IM or PMSM. One of their main disadvantages is the generation of acoustic noise due to high air-gap induction needed for higher power density. Moreover, at low speeds, these motors have high torque ripples. They also need special converter topology [2, 7]. Therefore, this work uses the PMSM drive for its advantages stated above, which are more convenient for EV and regenerative braking purposes.

Speed control of motor drives is a basic requirement in EV applications. It is realized by controlling the magnitude and frequency of the supplied voltage through a voltage source inverter (VSI). Pulse width modulation (PWM) is one of the most common techniques used to control a VSI and adjust the supplied voltage amplitudes and frequencies as desired for speed regulation. In this technique, PWM signals are generated to control the switching of each of the six switches of a two-level inverter. The most commonly used PWM techniques are the sinusoidal pulse width modulation (SPWM) and the space vector pulse width modulation (SVPWM). SPWM uses a sine wave as its modulation input and a triangular carrier signal since the output voltage is expected to be sinusoidal. The frequency of the modulation input wave is the same as the desired output frequency; whereas, the frequency of the carrier signal determines the switching frequency of the VSI and is usually much higher than the modulation frequency. SPWM reduces torque ripples, and has a wide range of operation and good starting performances. However, it has relatively high switching losses compared to other schemes. On the other hand, SVPWM aims at getting a round constant-magnitude rotating mag-

netic field for the motor to obtain a constant electromagnetic torque. It controls the switches of the three-bridge arms of a VSI. Since the switches of each arm are always reversed, and each switch has two possible states, 1 (ON) or 0 (OFF), this results into eight possible combinations of the bridge arms switch states: 000, 001, 010, 011, 100, 101, 110 and 111. These combinations result in eight corresponding voltage vectors, forming the so-called space vector in the two dimensional $\alpha - \beta$ plane. Each two adjacent vectors form a sector. The main principle of SVPWM is to form an approximation of the reference space voltage vector by switching between the two adjacent voltage vectors in a given sector. The desired sector is determined through calculations and a table of all possible states with their corresponding outputs. The switching is always done such that only one switch is changed in a given cycle to minimize switching losses in the VSI. The duty ratio of switching between two voltage vectors is also computed to obtain the closest approximation of the reference vector. SVPWM has several advantages such as its high utilization of DC bus voltage, its low losses, low torque ripples and ease of implementation using digital controllers [8–11].

Various control methods exist for speed regulating applications of AC drives. Mainly, control schemes are divided into open loop and closed loop control. Open loop control of PMSM requires no feedback of the system. Typically, such control scheme is adapted by applications that require no feedback or closed loop control schemes such as pumps of fans. An example of open loop control schemes is the Volts-per-hertz (V/f) control scheme, which is mainly used for scalar control applications. It is also used when the desired output speed is obtained from the input frequency and the equivalent required voltage is computed, controlling the VSI to operate the machine at such frequency. In synchronous machines, the motion of the rotor has to always be synchronized with the stator applied frequency to guarantee stable control and performance. Since open loop V/f control does not include a feedback loop in its control algorithm, the position of the rotor is not measured. To overcome this, some PMSMs include damper windings in their rotor to ensure the synchronization of the rotor with the stator applied frequency. In some cases, such as surface mounted PMSM, this is not easy to manufacture, and the cost of such design is very high. Therefore, most PMSM machines do not include damper windings in the rotor, which affects the performance of these

machines under open-loop V/f control schemes. To overcome this, other approaches are studied to ensure the synchronization between the rotor movement and the stator input frequency. Disturbances in the DC-link current are used to modulate the input frequency to sustain a stable operation of the PMSM. Some researchers, e.g.. [12, 13] aimed to keep the power input to the PMSM minimized by controlling the voltage using search algorithms. On the other hand, other studies, such as [14], aimed to control the voltage to maintain a unity power factor. These techniques showed improved stable performances but lacked versatility in low-speed drive performances. The researchers in [15] propose another V/f control method, where the voltage is calculated to maintain a constant stator flux linkage in the PMSM. This enables the machine to produce the same torque ratings over all operating frequency ranges. This allows overcoming the drawbacks of the previous control methods in low-speed performances. The input frequency is then modulated with a factor proportional to the disturbances in input power. This modulation will damp the rotor movement to ensure synchronization between the stator and the rotor.

Closed loop control, provides more robustness for various applications. Contrary to open loop control, closed loop control requires a feedback signal to determine the position of the rotor. This signal can be either measured using a sensor or can be estimated. Several control techniques are available to control motor drives, such as vector control, hysteresis current control (HCC) and direct torque control (DTC). The main principle of DTC is to adjust the stator voltage vector based on the errors between the actual torque and stator flux linkage and their references. This method does not require any current controllers or motor parameters except for stator resistances. Hence, it is insensitive to parameter variations of the machine. DTC also provides fast torque responses and simple implementation. However, it is known for high torque and flux ripples that cause vibrations and increase the losses [16, 17].

Vector control, also known as field oriented control (FOC), is the most commonly used control technique in AC motor drives. It is robust and reliable in most drive applications. The main role of field orientation is to decouple the machine's generated flux from the torque in order to control both separately as desired. This is done by replacing the three-phase stationary representation of the stator field with a dynamic

two-phase rotating d-q frame, where, the rotor magnetic field is aligned with the d-axis. In this process, the motor torque can be controlled separately by controlling the current in the quadrature (q) axis. Similarly, the flux is controlled independently by controlling the current in the direct (d) axis. Therefore, torque and flux are controlled separately. By analogy, operating a three-phase AC machine under field orientation is similar to the operation of a separately excited DC machine, where, the field circuit controls the generated flux while the armature circuit regulates the torque of the motor. In other words, the three-phase variables are simplified into two circuits that can be controlled independently [18]. There are two types of FOC; direct field oriented control (DFOC) and indirect field oriented control (IFOC). DFOC was introduced by Blaschke [19] in 1971. In DFOC, the machine's generated flux is measured directly through mounted sensors that measure the rotor's absolute position and generated flux. However, this method increases the cost of the drive system as it depends on expensive sensors. Mounting these sensors is also a challenge and this increases the cost furthermore [20]. For these reasons, IFOC is more common and is widely used in both research and industrial applications. IFOC, also known as sensorless FOC, was presented by Hasse [21] in 1968. As opposed to DFOC, neither the installation of expensive sensors nor measuring the flux is required in this method. Instead, the position of the generated rotor flux can be estimated from the measured currents. This reduces the cost and the drawbacks of DFOC and has proven to work efficiently. For these reasons, IFOC is probably the most popular and common control technique for AC drives. It doesn't require additional measurements, and controlling the motor flux and torque is decoupled, which provides flexibility in the control efforts depending on the required performance or application [20]. FOC consists of two control loops; an inner loop consisting of current regulators and an outer loop which controls the speed or position of the motor. In general, the torque or current regulators have to be tuned before tuning the speed controller, and the speed controller cannot be tuned without the assumption that the current regulators are tuned perfectly [22]. Due to its reliability and robustness, this study implements the speed control of PMSM using FOC as a benchmark to test and compare the performance of another proposed controller; the synergetic controller.

Synergetic control (SC) is a non-linear control technique that is well-suited for nonlinear systems. It overcomes the disadvantages of simple classical linear controllers such as the Proportional-Integral (PI) controller. The main disadvantage of these linear controllers in non-linear system dynamics is their operation in a region or set of solutions around an equilibrium point. Linear controllers do not perform well under large signal variations. Synergetic control theory overcomes these disadvantages as the system model with all of its non-linearity is used in the controller design process. This control theory is close to that of sliding mode controllers; both share similar properties and advantages, such as order reduction of the system and decoupling design procedure. Despite this, SC is still more advantageous compared to the sliding mode control, for it does not require high bandwidth to operate as opposed to the sliding mode control. This makes it suitable for digital implementation. Furthermore, contrary to sliding mode controllers, SC maintains constant switching frequencies. This leads to less noise in the system due to switching. Finally, synergetic control operates continuously as opposed to the sliding mode controller which is known for its discontinuity. As mentioned, the system model is used for the controller synthesis process. Although this leads to better control as it provides more information about the system dynamics, it also makes the controller sensitive to errors in system parameters considered in the model itself [23–25]. However, this can be overcome by proper selection of the macro-variables which is further discussed in chapter 3.1.2. The synergetic control has been previously used in motor drive applications [26–30]. It has been implemented as a non-linear speed control of multiple IM and PMSM drives. In [26], the authors derive a control law that reduces the order of the system and devise a simple method to select the closed loops poles of the system. However, they do not take into account any load variations applied on the system which will affect the steady state speed of the drive. On the other hand, researchers in [27] introduce an adaptive controller based on the synergetic approach to control a PMSM drive. Although, this controller takes into consideration any application of load torque on the motor, there remains some steady state error in the motor speed. In [28], the authors implement a synergetic controller to control the speed of an IM drive. They show the effect of changing some controller parameters on the response speed, transient behavior, steady state error and response to load applications.

However, they propose too many manifolds although the system has only two control inputs. In [29], the synergetic controller and vector control to control an IM drive. The proposed controller uses the synergetic control theory to control the speed and generate reference d-q currents. The motor currents are regulated using vector control, where a hysteresis current controller is implemented to regulate the motor currents. Finally, in [30], researchers compare between the synergetic and the sliding mode controllers in controlling the speed of an IM. The results show that the synergetic controller was able to reduce the effect of load torque application as well as vibration torques caused by the discontinuities presented by the sliding mode controller.

1.1. Work Contributions

This research aims to investigate a new method for speed control of a PMSM drive. The synergetic controller is designed and implemented on a physical setup in the lab. FOC is also implemented and used as a reference to test the synergetic controller's performance. This research also provides an experimental comparative study of the two controllers and studies their performance under different situations, such as response time, response to load torque variations and performance under regenerative braking. The design of the synergetic controller is crucial to the system behavior and affects the performance of the controller. Therefore, the following procedures have been done.

- A new macro-variable is designed and implemented to improve the performance of the SC. The macro-variable enhances the behavior of the d-axis current i_d and eliminates any steady state errors. The behavior of this controller is improved compared to the one in literature.
- A thorough study of the effect of each gain used in the controller design of the SC is conducted.
- A special macro-variable of the SC is designed and implemented to operate the motor under regenerative braking by controlling the motor torque.
- Regenerative braking under FOC and SC is investigated and implemented. Two techniques are used to operate the motor in regenerative mode; speed control mode and torque control mode.

1.2. Thesis Organization

The following chapters of this thesis are organized as follows. Chapter 2 demonstrates the theory behind field oriented control as well as simulation results of a FOC along with an SPWM modulator. The synergetic controller is presented in chapter 3. It discusses the design procedure of the SC as well as other different controllers designed through the course of this work. Simulation results are reported in chapter 3. Chapter 4 provides a brief introduction, background information and analysis previously done in the literature about regenerative braking. it also discusses the regenerative braking synergetic controller design. In chapter 5, the experimental setup and results are discussed. Finally, chapter 6 concludes the results of this work and provides recommendations and suggestions for future work.

Chapter 2: PMSM and Field Oriented Control

2.1. Mathematical Model of PMSM

The PMSM is the motor drive of choice in this work. Its stator consists of three-phase, sinusoidally distributed windings. These windings form together the stator field vectors ($\vec{I}_s$, $\vec{V}_s$) and a rotating magnetic field ($\vec{B}_s$). On the other hand, the rotor does not consist of any windings. Instead, permanent magnets are fixed on the rotor, generating the rotor magnetic field ($\vec{B}_r$) [18]. These magnets can be fixed on the surface of the rotor, known as surface mounted PMSM (SMPMSM), or internally (IPMSM). The current study uses the SMPMSM. The mathematical model of the PMSM in three-phase reference (3ϕ) frame is given by Eq. (1)-(3) [31].

$$\vec{I}_s = \frac{2}{3}\left(i_u(t) + i_v(t)e^{j\frac{2\pi}{3}} + i_w(t)e^{j\frac{4\pi}{3}}\right) \tag{1}$$

$$\begin{bmatrix} v_u \\ v_v \\ v_w \end{bmatrix} = R_s \begin{bmatrix} i_u \\ i_v \\ i_w \end{bmatrix} + \frac{d}{dt}\begin{bmatrix} \psi_u \\ \psi_v \\ \psi_w \end{bmatrix} \tag{2}$$

$$\begin{bmatrix} \psi_u \\ \psi_v \\ \psi_w \end{bmatrix} = \begin{bmatrix} L_u & M_{uv} & M_{uw} \\ M_{vu} & L_v & M_{vw} \\ M_{wu} & M_{wv} & L_w \end{bmatrix} \begin{bmatrix} i_u \\ i_v \\ i_w \end{bmatrix} + \psi_{PM} \begin{bmatrix} cos(\theta) \\ cos(\theta - \frac{2\pi}{3}) \\ cos(\theta - \frac{4\pi}{3}) \end{bmatrix} \tag{3}$$

Eq. (1) defines the stator current vector at any given time. Eq. (2) shows the phase windings voltages, where R_s is the stator resistance. Eq. (3) defines the total flux linkage, where L_x denotes the self-inductance in each phase, M_{xx} denotes the mutual inductance between two phases and ψ_{PM} is the flux produced by the permanent magnets on the rotor. Deriving the electromagnetic torque in this form is complex. Therefore, the model must be simplified first as explained in the next section.

2.2. Mathematical Analysis of Field Oriented Control

In order to simplify the analysis of the PMSM, the mathematical model is transformed into a two-phase reference frame. The transformation is achieved by the Clarke-Park transformation [18] [32]. This transforms the system variables, such as voltages or currents, from a three-phase reference frame (UVW) to a fixed two-phase reference frame ($\alpha\beta$). This transformation simplifies the analysis of three-phase machines and is used in generating simplified reference signals for the control system. Figure 1 shows the SMPMSM reference frames. The stator consists of three-phase windings; $\alpha - \beta$ reference frame is fixed, and $d - q$ frame is rotating with an angle θ. The permanent magnets are surface mounted on the rotor and thus create a rotating magnetic field. Eq. (4) shows the forward Clarke transformation from (UVW-) reference frame to ($\alpha\beta$-) reference frame.

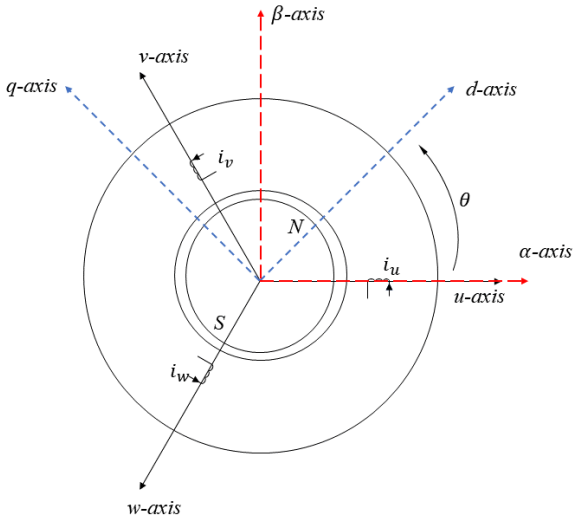

Figure 1: SM-PMSM reference frames

$$\begin{bmatrix} i_\alpha \\ i_\beta \\ i_\gamma \end{bmatrix} = \frac{2}{3} \begin{bmatrix} 1 & -\frac{1}{2} & -\frac{1}{2} \\ 0 & \frac{\sqrt{3}}{2} & -\frac{\sqrt{3}}{2} \\ \frac{1}{2} & \frac{1}{2} & \frac{1}{2} \end{bmatrix} \begin{bmatrix} i_a \\ i_b \\ i_c \end{bmatrix} \tag{4}$$

The inverse transformation from ($\alpha\beta$-) reference frame to (UVW-) reference frame is given by Eq. (5) [33].

$$\begin{bmatrix} i_a \\ i_b \\ i_c \end{bmatrix} = \begin{bmatrix} 1 & 0 & 1 \\ -\frac{1}{2} & \frac{\sqrt{3}}{2} & 1 \\ -\frac{1}{2} & -\frac{\sqrt{3}}{2} & 1 \end{bmatrix} \begin{bmatrix} i_\alpha \\ i_\beta \\ i_\gamma \end{bmatrix} \tag{5}$$

Similarly, Park transformation changes the system from three-phase reference frame (UVW-) to a dynamic rotating two-phase reference frame (dq). This transformation can be also used to transform the system components from a fixed ($\alpha\beta$) frame to a rotating (dq) frame as given by Eq. (6). The inverse transformation from (dq) to ($\alpha\beta$) is given by Eq. (7), where θ is the angle between the d-axis and the fixed α axis.

$$\begin{bmatrix} i_d \\ i_q \\ i_0 \end{bmatrix} = \begin{bmatrix} \cos(\theta) & \sin(\theta) & 0 \\ -\sin(\theta) & \cos(\theta) & 0 \\ 0 & 0 & 1 \end{bmatrix} \begin{bmatrix} i_\alpha \\ i_\beta \\ i_\gamma \end{bmatrix} \tag{6}$$

$$\begin{bmatrix} i_\alpha \\ i_\beta \\ i_\gamma \end{bmatrix} = \begin{bmatrix} \cos(\theta) & -\sin(\theta) & 0 \\ \sin(\theta) & -\cos(\theta) & 0 \\ 0 & 0 & 1 \end{bmatrix} \begin{bmatrix} i_d \\ i_q \\ i_0 \end{bmatrix} \tag{7}$$

A forward and inverse transformation between stationary 3-phase (UVW-) reference frame and rotating (dq-) reference frame also exist. The forward and inverse transformations are given by Eq. (8) and (9), respectively.

$$\begin{bmatrix} i_d \\ i_q \\ i_0 \end{bmatrix} = \frac{2}{3} \begin{bmatrix} \cos(\theta) & \cos(\theta - \frac{2\pi}{3}) & \cos(\theta + \frac{2\pi}{3}) \\ \sin(\theta) & \sin(\theta - \frac{2\pi}{3}) & \sin(\theta + \frac{2\pi}{3}) \\ \frac{1}{2} & \frac{1}{2} & \frac{1}{2} \end{bmatrix} \begin{bmatrix} i_a \\ i_b \\ i_c \end{bmatrix} \tag{8}$$

$$\begin{bmatrix} i_a \\ i_b \\ i_c \end{bmatrix} = \begin{bmatrix} \cos(\theta) & \sin(\theta) & 1 \\ \cos(\theta - \frac{2\pi}{3}) & \sin(\theta - \frac{2\pi}{3}) & 1 \\ \cos(\theta + \frac{2\pi}{3}) & \sin(\theta + \frac{2\pi}{3}) & 1 \end{bmatrix} \begin{bmatrix} i_d \\ i_q \\ i_0 \end{bmatrix} \tag{9}$$

This is to represent the machine variables in a frame that rotates synchronously with the stator vectors. In this process, the machine variables are represented as DC signals, similar to the case in DC motors, instead of three-phase sinusoidal signals. This transformation simplifies the analysis of the system and, upon applying field orientation, the torque and flux are decoupled and can be controlled separately. Field orientation is applied by aligning the rotor flux vector $\vec{\Psi}_r$ with the d-axis. This is done to ensure that the d-component of the stator current (i_d) is used to control the magnetic flux. Consequently, the q-component of the stator current (i_q) is used to control the machine's torque and hence, decoupling is achieved. In PMSM, the rotor field is generated by permanent magnets fixed on the rotor. The d-component of the stator current (i_d) is controlled to be kept at 0. This will prevent any flux weakening or demagnetization of the permanent magnet. The angular speed of the permanent magnet's flux vector $\vec{\Psi}_{PM}$ is equal to the electrical angular speed of the rotor (ω_m). Therefore, in order to maintain field orientation, the dq-frame's angular speed (ω_d) is rotated at the same electrical angular speed of the rotor as given by Eq. (10) [18].

$$\omega_d = \omega_m \tag{10}$$

Upon applying field orientation, the simplified mathematical model of the PMSM in the rotor reference frame is given by Eq. (11-13) [18, 34] as follows:

$$v_d = Ri_d + L_d \frac{di_d}{dt} - L_q i_q \omega_e \tag{11}$$

$$v_q = Ri_q + L_q\frac{di_q}{dt} + L_d i_d \omega_e + \omega_e \lambda_{PM} \tag{12}$$

$$J\frac{d\omega}{dt} = \tau_e + B\omega + \tau_L \tag{13}$$

The generated electromagnetic torque (T_e) in the rotating dq frame is given by Eq.(14). However, in case of surface mounted or non-salient PMSM, the inductances in both d and q axes are equal. Therefore, the expression of the electromagnetic torque of a non-salient PMSM can be further simplified into Eq. (15) [34].

$$T_e = \frac{3}{2}\frac{P}{2}[\lambda_{PM} i_q + (L_d - L_q) i_d i_q] \tag{14}$$

$$T_e = \frac{3}{2}\frac{P}{2}\lambda_{PM} i_q \tag{15}$$

Where P is the number of poles of the motor. Figure 2 shows the block diagram of the field oriented control scheme. The error between the reference speed and the actual mechanical speed of the machine is fed to a PI speed controller. The speed controller generates a command or reference q-axis current component (i_q^*).

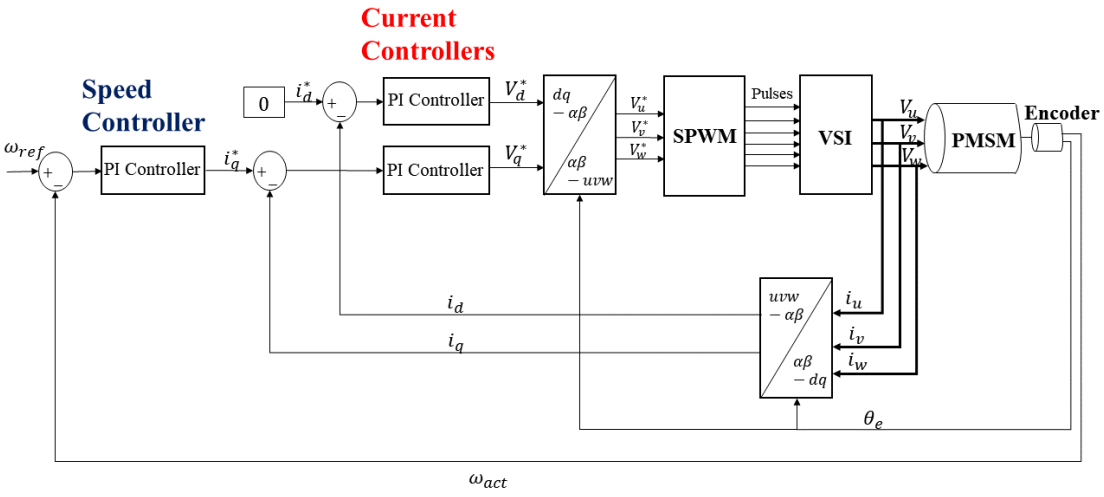

Figure 2: Field oriented control block diagram

In normal mode operation of PMSM using FOC, the reference current of the stator current d-component (i_d) is kept 0 to avoid any flux weakening or demagnetization of the permanent magnets. The current errors are fed to PI current regulators that regulate the currents in d and q, axes generating command voltages V_d^* and V_q^* for both d and q axes respectively. This is known as voltage controlled FOC. The dq-command voltages are then transformed into reference three-phase voltages using inverse Clarke and Park transformations. SPWM is used to generate switching pulses to the voltage source inverter (VSI) by comparing the reference three phase voltages to a carrier signal. The PWM signals control the output voltage of the inverter which supplies the PMSM. The rotor position is acquired using an encoder and the electrical angle of the machine is computed using the formula given in Eq.(16) to be used in Clarke and Park transformations. The machine's three-phase currents are also measured and transformed into dq currents using forward Clarke and Park transformations.

$$\theta_e = \frac{P}{2}\theta_{mech} \tag{16}$$

2.3. Simulation Analysis

In this section, the FOC scheme is designed and tested in MATLAB/Simulink environment. The PMSM is simulated and the performance of the controller algorithm is tested under different scenarios. The SPWM modulator is first tested separately and then included with the FOC to simulate the operation of a complete motor drive system.

2.3.1. SPWM Modulator. To simulate a SPWM modulator, a three-phase RL-load was created. The values for R and L used are the same values of the PMSM stator resistances and inductances. Figure 3 shows the Simulink model. Three-phase reference signals are input to the modulator that is connected to the three-phase load. The modulation index can be set by manipulating the amplitudes of the input reference sine signals. The carrier signal has a maximum amplitude $\hat{V}_{tri} = \frac{1}{2}U_{DC}$ and a frequency of $f_{sw} = 10kHz$. Figure 4 shows the carrier signal and the input control signals of the PWM modulator. The selected modulation index is $m_a = 0.5$, and the carrier frequency,

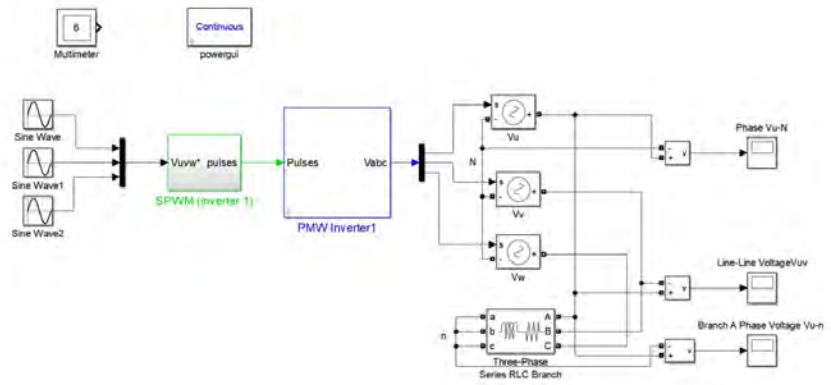

(a)

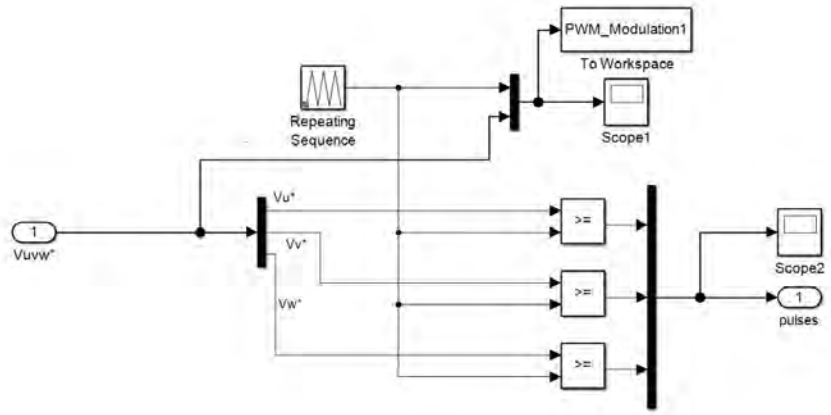

(b)

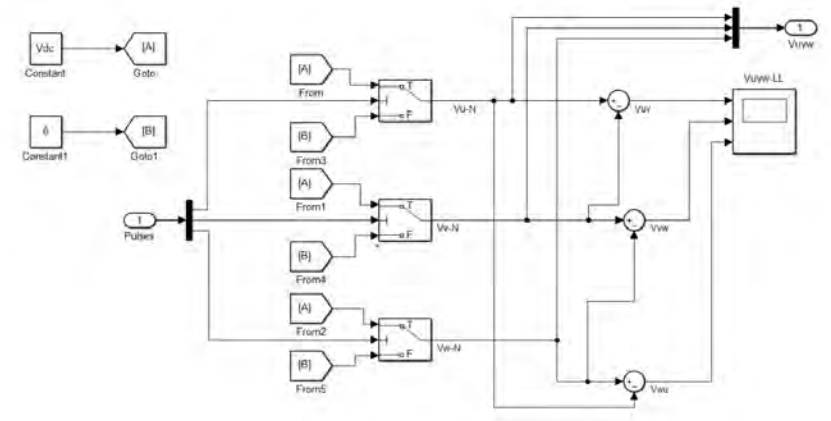

(c)

Figure 3: Simulation of SPWM modulator (a) Full Simulink Model (b) SPWM block (c) Inverter block

which is also the switching frequency of the inverter, is $f_c = 1kHz$ Figure 5 shows the

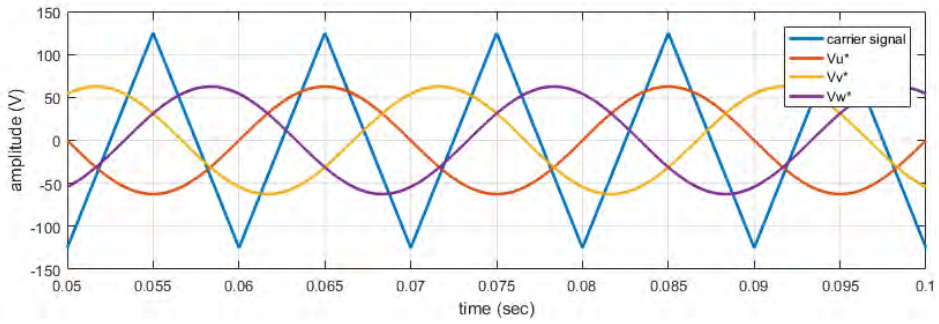

Figure 4: SPWM modulation

waveforms of the phase voltage V_a, line-line voltage V_{ab} and the three phase currents in the RL branch. The simulation results confirm the performance of the SPWM modulator.

2.3.2. FOC. The FOC scheme was designed based on the block diagram in Figure 2. The PMSM was simulated and tested under different scenarios. In the first simulation test, the motor starts from rest at $t = 0$ with a step input reference speed of 1000 RPM while being subjected to a load torque of 3 Nm. Next, the motor is subjected to another speed step to reach 1200 RPM. After the motor speed settles, the load torque is reduced to 1 Nm. The motor speed, dq axes currents, torque and three-phase currents are measured. The Simulink model of the FOC scheme is shown in Appendix A.

Figures 6 and 7 show the results of the simulation. The speed controller is able to track the speed reference. For the step reference input, the controller is able to track its new references with zero steady-state error. When the load torque is reduced, the speed of the motor increases, but the controller is able to bring the motor speed back down to its reference. The average value of the d-axis current i_d in steady state is 0 as required to avoid any demagnetization or flux weakening of the machine. The speed controller generates a torque command in transient periods, which in turn dictates the reference for the quadrature current i_q. The current regulators are able to track their respective references efficiently and the torque of the motor is equal to the load torque in steady state as desired. Finally, the three phase currents are sinusoidal and shifted by

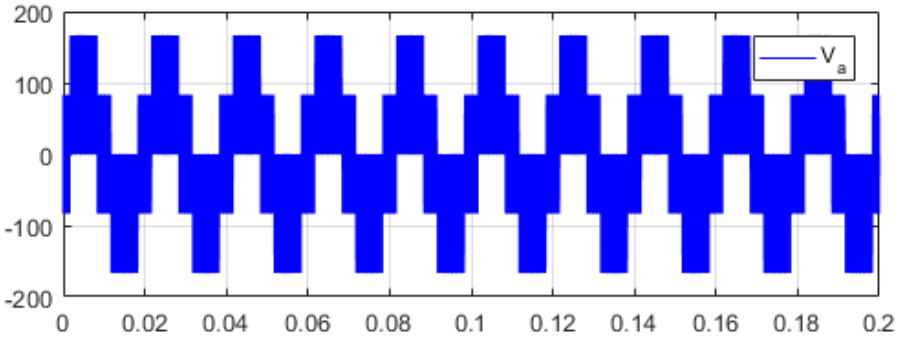

(a)

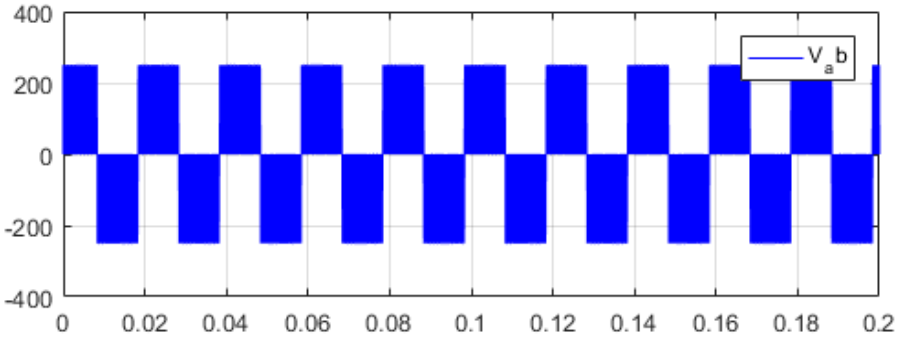

(b)

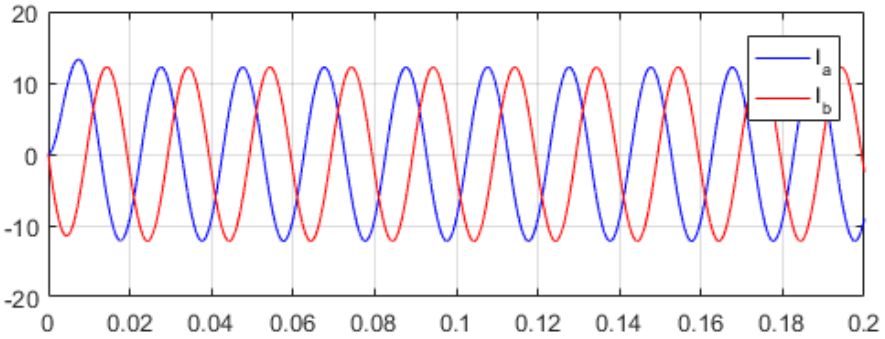

(c)

Figure 5: (a) Phase voltage (b) Line-line voltage (c) Phase current

120° apart. The current is reduced once the load torque is removed. The decoupling of dq currents can be seen in the figures 6c and 6d. It proves that field orientation is achieved, and the sinusoidal currents show that the transformation into a two-reference frame is performed accurately.

2.4. Hysteresis Current Control

The experimental setup used in the current study consists of a PMSM coupled to a DC motor. The DC motor acts as a load and is controlled to produce a torque

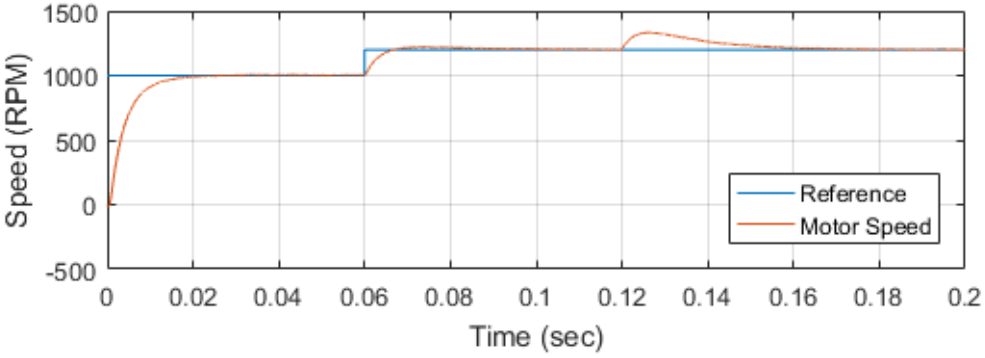

(a)

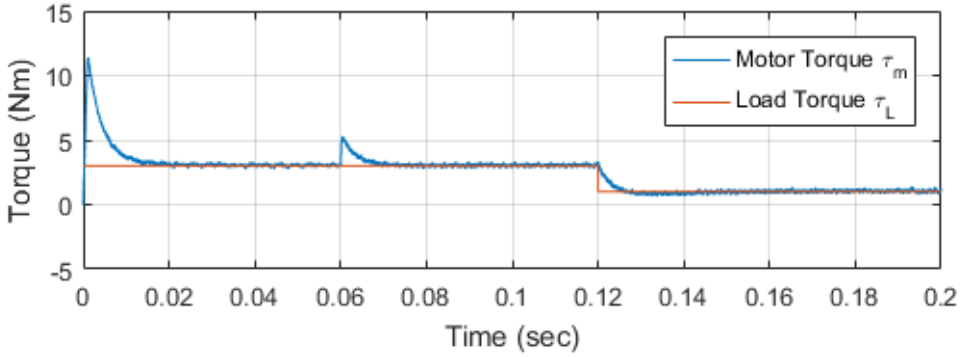

(b)

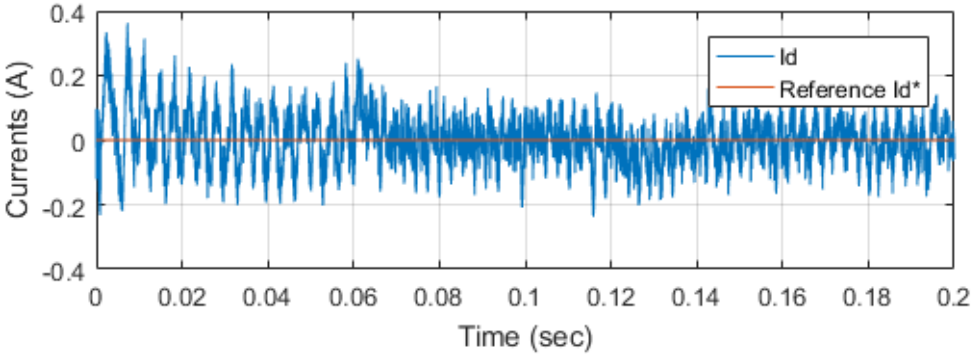

(c)

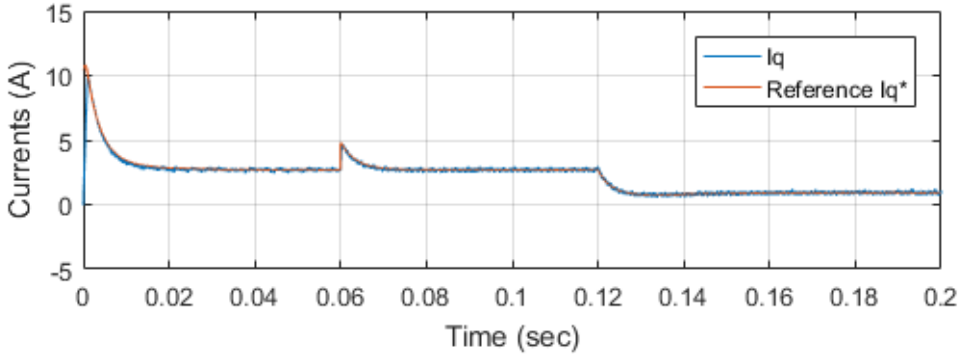

(d)

Figure 6: (Response of a) Motor speed (b) Motor torque (c) d-axis current (d) q-axis current under FOC

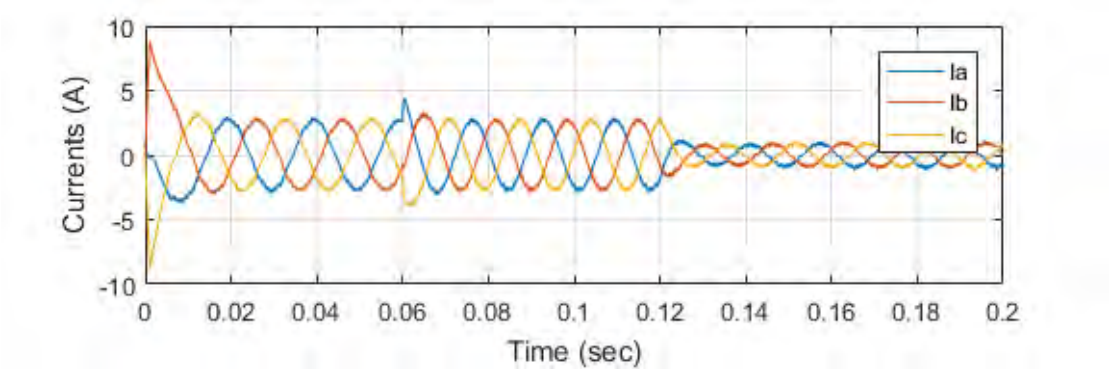

Figure 7: Three phase currents under FOC

that opposes the PMSM's torque. To control the output torque of the DC motor, a hysteresis current controller is implemented to control the DC motor's armature current. Hysteresis current control is used because it results in low current ripple and is easy to tune. Moreover, it is robust, provides good tracking capabilities and has a fast response. However, some of its drawbacks are the variable switching frequency and high switching losses. The desired torque can be translated into current simply by dividing it by the torque constant following the relation shown in Eq. (17), where K_t is the torque constant.

$$\tau_m = K_t i_a \tag{17}$$

Figure 8 shows the block diagram of the hysteresis current controller. The DC motor current is controlled using a DC-DC converter, simply known as H-Bridge. The H-Bridge switching is controlled using a dSPACE 1104 board.

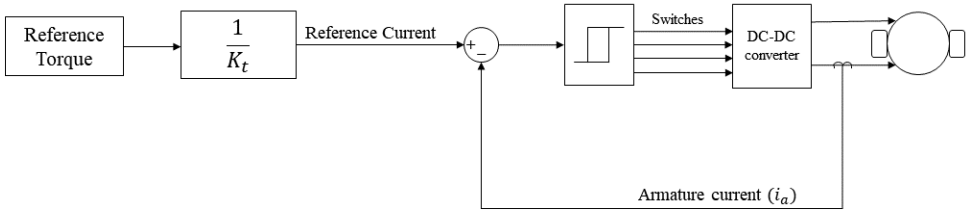

Figure 8: Hysteresis current controller block diagram

The current controller computes the error between the desired current and the actual current flowing in the motor's armature circuit. A relay block with predefined thresholds is used to switch the H-Bridge between ON-mode and OFF-mode. During ON-mode intervals, the motor is connected to +Vdc, and the armature current increases. Once the error in the current exceeds its upper threshold, the controller switches to OFF-mode. During OFF-mode intervals, the motor is connected to -Vdc, and the armature current starts decreasing. Once the error in the current exceeds its lower threshold, the controller switches back to ON-mode. This results in a triangular waveform of armature current that increases and decreases in a defined band around the desired current. Three inductances have been added in series with the DC motor coil in order to increase the electrical time constant of the motor and have a sufficient time window for the controller to react to the current's behavior [35]. Figure 9 shows the expected waveforms of the current and how the switching occurs.

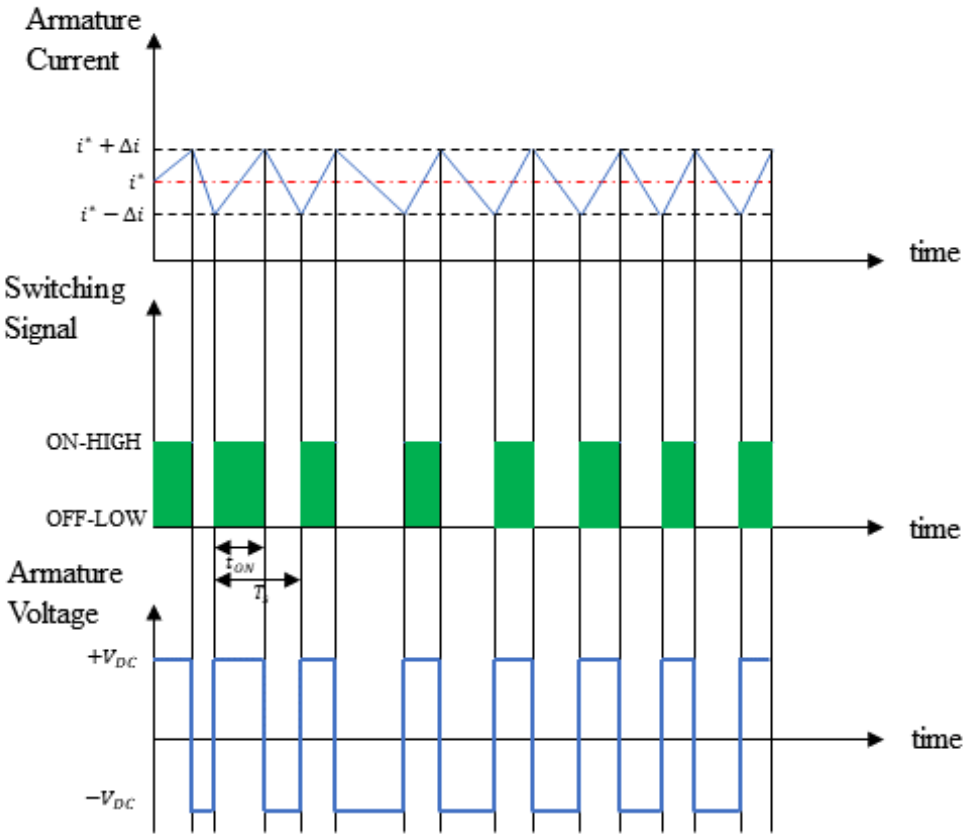

Figure 9: Hysteresis current controller waveforms

The mathematical model of a DC motor is given by Eq. (18)-(19).

$$V_a = R_a i_a + L\frac{di}{dt} + K_b\omega \tag{18}$$

$$J\frac{d\omega}{dt} = \tau_m - B\omega - \tau_c \tag{19}$$

Where R_a is the armature resistance, L is the coil inductance, K_b is the back-EMF constant, J is the motor's inertia, τ_m is the motor's torque, B is viscous friction coefficient and τ_c is the coulomb friction. The parameters of the used DC motor are given in Appendix A. Studying the mechanical equation of a DC motor given by Eq. (19), the motor's angular acceleration is directly proportional to the motor torque; in other words, to the armature current. Thus, if the armature current is kept constant for long periods of time, the motor's speed will continue to increase and will exceed its rated mechanical speed which will damage the motor. Therefore, to test the hysteresis controller, a square wave current reference is used. Figure 10 shows the motor speed, motor torque and the armature current. The controller was tuned such that its off-time threshold is $-0.1A$ and its on-time threshold is $0.15A$, these values are selected to reduce the current ripples as much as possible. However, experimental results show that the current ripple was $\pm 0.2A$ as shown in Fig 10d.

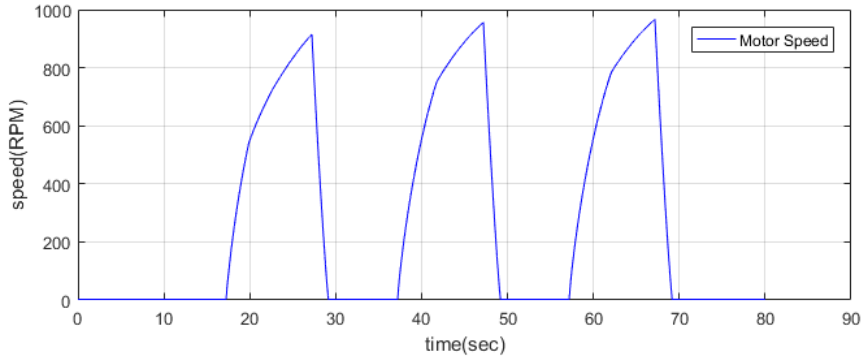

(a)

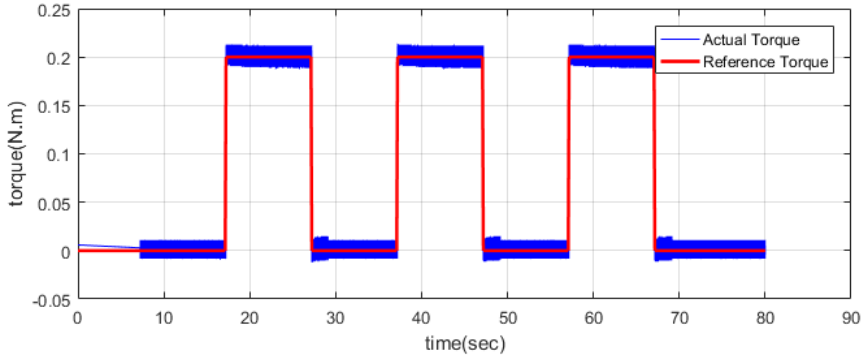

(b)

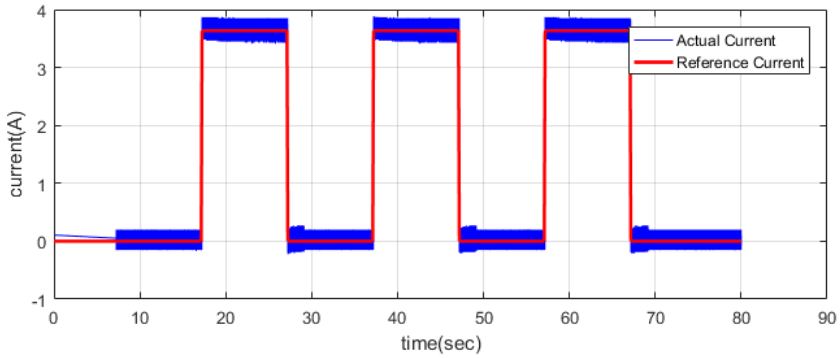

(c)

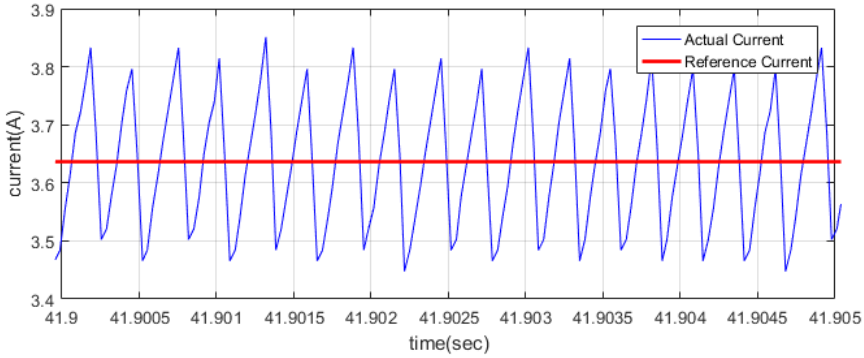

(d)

Figure 10: (a) DC motor speed (b) DC motor torque (c) Armature current (d)Zoomed views of the current

Chapter 3: Synergetic Control

3.1. Synergetic Controller Design

3.1.1. Theoretical Analysis. The synergetic control design procedure is based on the Analytical Design of Aggregated Regulators (ADAR) method [23,24,36]. Given a non-linear system, described by its state space equation in the form given by Eq. (20).

$$\dot{x} = f(x,d,t) \tag{20}$$

Where x is the state vector defining all the state variables of the system, d is the control input vector, and t denotes time. First, the so-called macro-variable is defined as a function of the system state variables as shown in Eq. (21).

$$\psi = \psi(x) \tag{21}$$

The objective of the control effort is to force the system dynamics to operate on the manifold $\psi = 0$. Defining a manifold adds a new constraint on the system and hence reduces the order of the system as mentioned earlier. This will also force the system towards stability, preventing it from diverging. Depending on the control specifications and limitations (e.g to avoid saturation), the macro-variable characteristics are selected. The simplest case is defining the macro-variable as a linear combination of the state variables. A macro-variable is defined for each desired control input. In other words, the number of macro-variables of a given system is equal to the number of the system input channels. The dynamics of the macro-variable are subjected to the constraint given by Eq. (22):

$$T\dot{\psi} + \psi = 0, \quad T > 0 \tag{22}$$

Where T is a time constant that defines the convergence speed to the manifold specified by the macro-variable. It can be tuned and selected by the designer. Defining the appropriate macro-variable will force the system towards global stability, parameter in-

sensitivity and noise suppression. As discussed earlier, the controller synthesis depends greatly on the system model. Therefore, any uncertainties in the model parameters may affect the controller's performance. To avoid using costly complex observers to estimate system parameters, studies show that this drawback can be overcome by the appropriate selection of the macro-variables [36].

By using the chain rule of differentiation, the expression of $\dot{\psi}$ can be computed as shown in Eq. (23). The control input d can be computed using Eq. (24).

$$\frac{d\psi}{dt} = \frac{d\psi}{dx}\frac{dx}{dt} \tag{23}$$

$$T\frac{d\psi}{dt}f(x,d,t) + \psi = 0 \tag{24}$$

3.1.2. SC Controller Design for the PMSM. As discussed in the previous subsection, a good knowledge of the system model is needed before designing the controller. By referring to the mathematical model of the PMSM in rotor reference frame, given by Eq.(11-13) in section 2.2, and rearranging these equations, the expressions for $\frac{di_d}{dt}$ and $\frac{di_q}{dt}$ can be found as follows:

$$\frac{di_d}{dt} = \frac{1}{L_d}[v_d - Ri_d + L_q i_q \omega_e] \tag{25}$$

$$\frac{di_q}{dt} = \frac{1}{L_q}[v_q - Ri_q - L_d i_d \omega_e - \omega_e \lambda_{PM}] \tag{26}$$

It can be seen from Eq. (11) and (12) that the PMSM in this representation has two control input channels; v_d and v_q. Thus, two macro-variables are needed. A macro-variable is defined for each axis, which also means that torque and flux will be decoupled similar to FOC. Consider the following set of macro-variables given by Eq. (27) and (28) [26].

$$\psi_1 = i_d \tag{27}$$

$$\psi_2 = K_1(\omega - \omega_{ref}) + K_2 i_q + K_3 \int (\omega - \omega_{ref})dt \tag{28}$$

where K_1, K_2 and K_3 are the SC controller gains. These macro-variables are not chosen randomly, but the control effort forces the macro-variable to operate on the manifold $\psi = 0$ following the dynamics given by Eq.(22). Therefore, the first macro-variable ψ_1 is selected to be equal to i_d since i_d is preferably kept at 0 in PMSM systems to avoid any flux weakening or demagnetization of the permanent magnets. As for the second macro-variable ψ_2, the first and last terms act as a speed controller, and together, they generate a command reference for the current in the q-axis (i_q^*). ω_{ref} is the reference speed desired by the designer. By selecting $K_2 = 1$, the resultant will be the error in the q-axis current $i_q - i_q^*$, which will converge to 0 automatically following the dynamics of the macro-variable.

3.1.2.1. Direct Axis Macro-variable (ψ_1). After selecting the macro-variables, the constraint given by Eq.(22) is applied for each macro-variable.

$$\psi_1 = i_d \tag{29}$$

$$T_d \frac{d\psi_1}{dt} + \psi_1 = 0 \tag{30}$$

Solving for $\frac{d\psi_1}{dt}$, the expression for $\frac{di_d}{dt}$ is plugged in from Eq. (25)

$$\frac{d\psi_1}{dt} = \frac{di_d}{dt} = \frac{1}{L_d}[v_d - Ri_d + L_q i_q \omega_e] \tag{31}$$

Next, Eq. (27) and (31) are substituted in Eq. (30).

$$T_d[\frac{-R}{L_d} i_d + \frac{L_q}{L_d}\omega_e i_q + \frac{1}{L_d} v_d] + i_d = 0 \tag{32}$$

The last step is to solve for the control input v_d

$$v_d = (R - \frac{L_d}{T_d}) i_d - L_q \omega_e i_q \tag{33}$$

By this, the first control input is solved for. As seen from Eq. 33, the expression for v_d is a function of system parameters and the variable T_d which is selected by the designer.

The same procedure is repeated with the second macro-variable ψ_2 to find the second control input v_q.

3.1.2.2. Quadrature Axis Macro-variable (ψ_2). Applying the same procedure to solve for v_q, the second macro-variable ψ_2 is given by:

$$\psi_2 = K_1(\omega - \omega_{ref}) + K_2 i_q + K_3 \int (\omega - \omega_{ref}) dt \tag{34}$$

This macro-variable is subjected to the following constraint:

$$T_q \frac{d\psi_2}{dt} + \psi_2 = 0 \tag{35}$$

Solving for $\frac{d\psi_2}{dt}$, the first time derivative can be shown as follows:

$$\frac{d\psi_2}{dt} = K_1 \frac{d\omega}{dt} + K_2 \frac{di_q}{dt} + K_3(\omega - \omega_{ref}) \tag{36}$$

Expanding the term $\frac{di_q}{dt}$ in Eq.(36) with the expression from Eq.(26), the expanded expression of $\frac{d\psi_2}{dt}$ becomes the following:

$$\frac{d\psi_2}{dt} = K_1 \frac{d\omega}{dt} + K_2 [\frac{-R}{L_q} i_q - \frac{1}{L_q} \omega_e \lambda_{PM} - \frac{L_d}{L_q} \omega_e i_d + \frac{1}{L_q} v_q] + K_3(\omega - \omega_{ref}) \tag{37}$$

Substituting with Eq. (37) and (28) in Eq. (35), the solution for the second control input v_q can be found from Eq. (38-41) as follows.

$$T_q [K_1 \frac{d\omega}{dt} + K_2 (\frac{-R}{L_q} i_q - \frac{1}{L_q} \omega_e \lambda_{PM} - \frac{L_d}{L_q} \omega_e i_d + \frac{1}{L_q} v_q) + K_3(\omega - \omega_{ref})] + ... \\ K_1(\omega - \omega_{ref}) + K_2 i_q + K_3 \int (\omega - \omega_{ref}) dt = 0 \tag{38}$$

$$K_1 \frac{d\omega}{dt} + K_2 (\frac{-R}{L_q} i_q - \frac{1}{L_q} \omega_e \lambda_{PM} - \frac{L_d}{L_q} \omega_e i_d + \frac{1}{L_q} v_q) + K_3(\omega - \omega_{ref}) = ... \\ - \frac{K_1}{T_q}(\omega - \omega_{ref}) - \frac{K_2}{T_q} i_q - \frac{K_3}{T_q} \int (\omega_{rated} - \omega_{ref}) dt \tag{39}$$

$$\frac{-R}{L_q}i_q - \frac{1}{L_q}\omega_e\lambda_{PM} - \frac{L_d}{L_q}\omega_e i_d + \frac{1}{L_q}v_q = \frac{-K_1}{K_2}\frac{1}{T_q}(\omega-\omega_{ref}) - \frac{1}{T_q}i_q - \frac{K_3}{K_2}\frac{1}{T_q}\int(\omega-\omega_{ref})dt\ldots$$
$$-\frac{K_1}{K_2}\frac{d\omega}{dt} - \frac{K_3}{K_2}(\omega-\omega_{ref}) \quad (40)$$

Finally, the expression for the control input v_q can be computed as follows:

$$v_q = \frac{-K_1}{K_2}\frac{L_q}{T_q}(\omega-\omega_{ref}) - \frac{L_q}{T_q}i_q - \frac{K_3}{K_2}\frac{L_q}{T_q}\int(\omega-\omega_{ref})dt - \frac{K_1}{K_2}L_q\frac{d\omega}{dt} - \frac{K_3}{K_2}L_q(\omega-\omega_{ref})\ldots$$
$$+Ri_q + L_d\omega_e i_d + \omega_e\lambda_{PM} \quad (41)$$

As show in Eq. (41), the expression for the control input v_q depends on the system parameters and the controller gains K_1, K_2, K_3 and T_q that are tuned and selected by the designer.

In conclusion, the synergetic controller requires 4 inputs; desired motor speed (ω_{ref}), dq currents (i_d and i_q) and actual motor speed. The expressions for each of the two control inputs are computed and the commands closed loop voltages v_d^* and v_q^* are computed. These voltages are then converted into three phase voltages using inverse Clarke-Parke transformation and the corresponding SPWM signals are generated to control the switching of the VSI as desired. Figure 11 shows the block diagram of the synergetic controller.

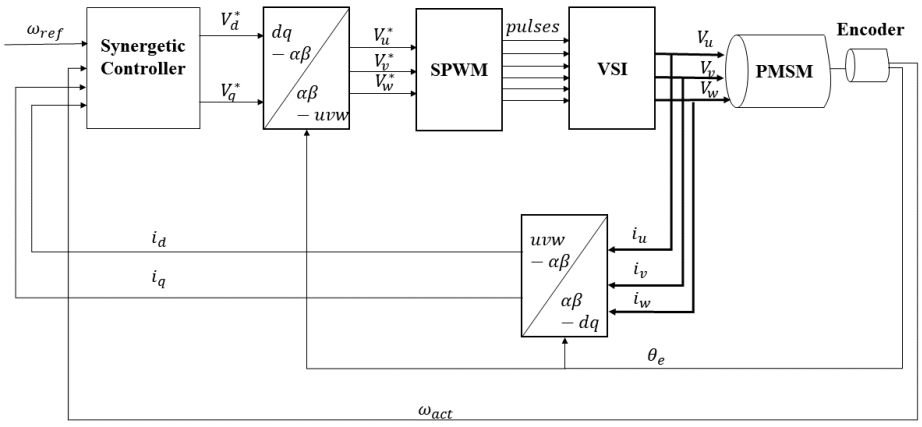

Figure 11: Synergetic controller block diagram

3.2. Simulation Analysis

In this section, the synergetic controller is designed and simulated in MATLAB/Simulink environment. The controller performance is tested under the same conditions as those applied on the FOC scheme. In addition, the same SPWM modulator is used. The previously synthesized controller in section 3.1.2 is used in these simulations. The gains of the controller are tuned manually based on a trial and error basis to reach the desired performance. The motor speed, torque, dq and three-phase currents are analyzed to check the performance of the SC. The responses of the two designed macro-variables are observed as well.

Figure 12 shows the simulation results. It can be observed that the controller is able to track the speed efficiently. It reaches its steady state value after every transition. Once the load torque is reduced, the controller is able to maintain the motor speed. The motor torque is also equal to the load torque in steady state. The d-axis current is maintained at 0 as desired to avoid machine demagnetization or flux weakening. The Simulink model is attached in Appendix B.

Figure 13 shows the response of the three phase currents as well as the response of the designed macrovariables ψ_1 and ψ_2. The objective of the control effort is to force these macrovariables to operate on the manifold $\psi = 0$. Simulation results indicate that the designed macrovariables converge to 0 as expected. The synergetic controller was able to control the PMSM speed and force the macro-variables to operate on the manifold $\psi = 0$.

The designed controller in section 3.1.2 assumes ideal operation and knowledge of the system parameters. Since the synergetic controller depends on the system parameters, any errors or miscalculations of these parameters lead to the wrong command law, and thus the macro-variable will not converge to 0 [23], [24]. This might not be apparent in simulation since the same parameters are used for both controller design and simulation of the PMSM. Practically, there will always remain some discrepancies between actual system parameters and the ones estimated in the controller design process. One way to avoid this problem is the implementation of high speed observers that estimate any unknown parameters. However, this solution is undesirable as it will increase

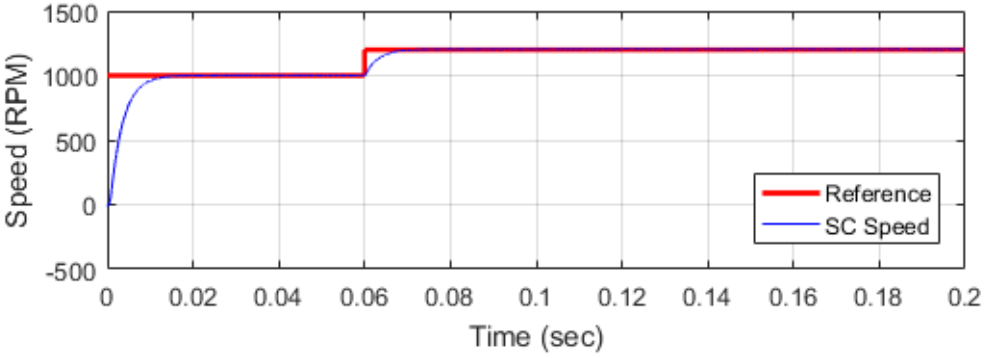

(a)

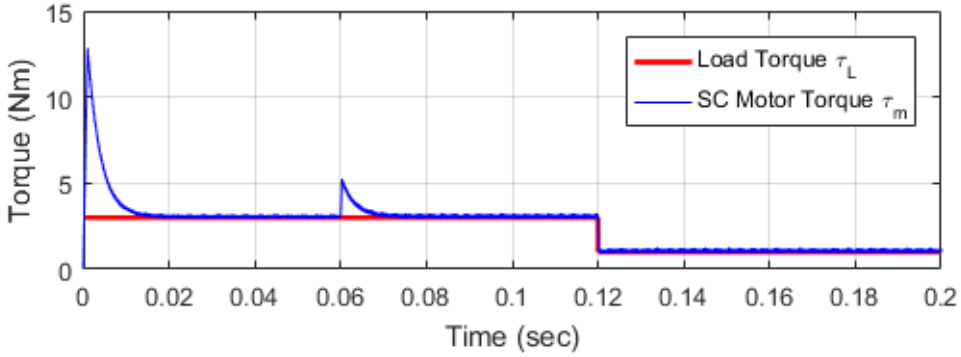

(b)

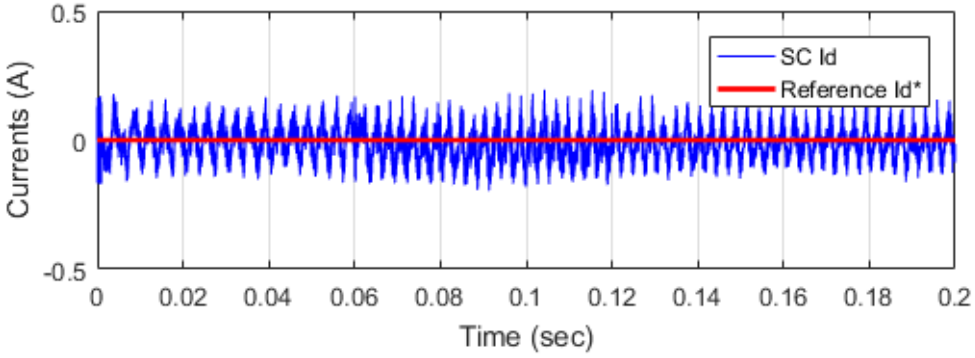

(c)

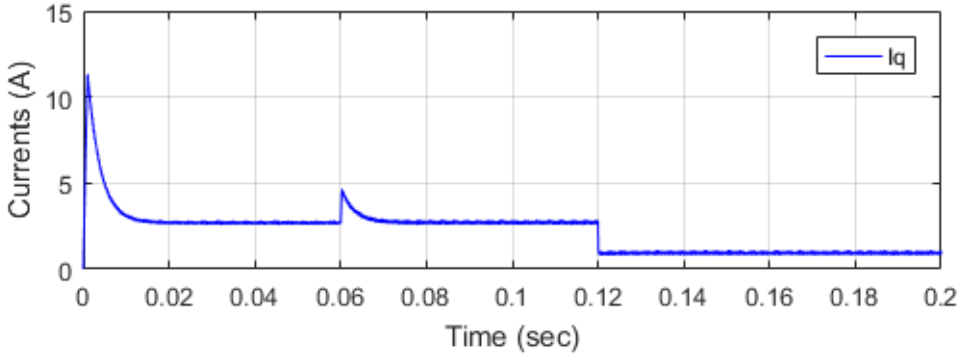

(d)

Figure 12: (a) Speed response (b) PMSM torque (c) d-axis current (d) q-axis current under SC

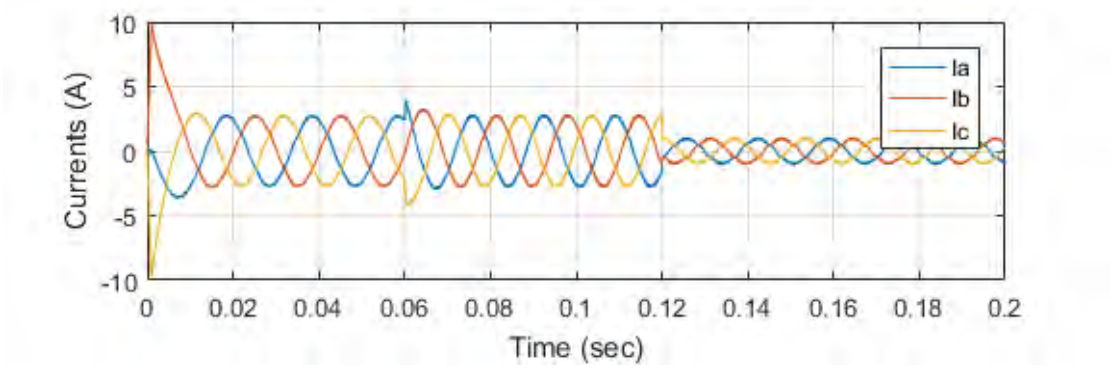

(a)

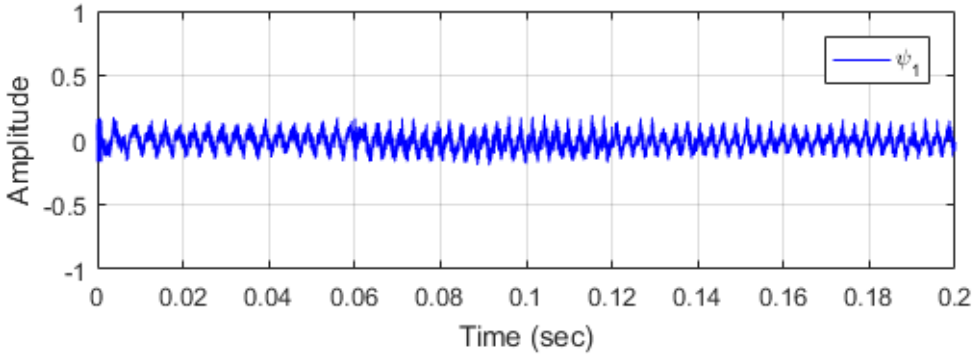

(b)

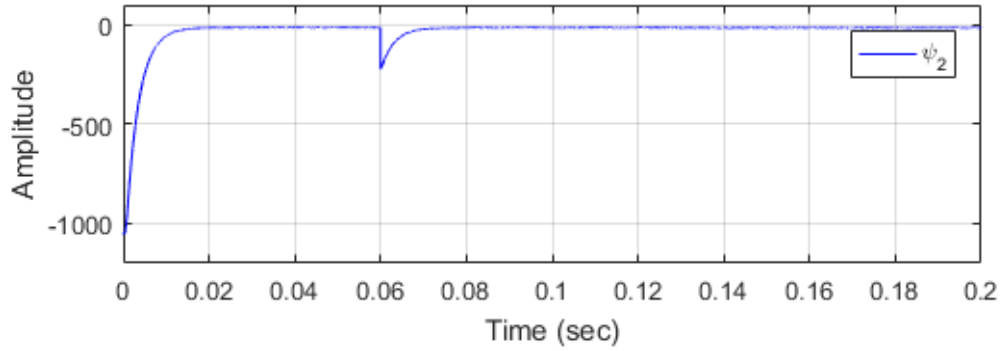

(c)

Figure 13: (a) Three phase current (b) Macrovariable ψ_1 (c) Macrovariable ψ_2

computation costs. Therefore, in order to improve the performance of the synergetic controller, the following improved SC is proposed in this study.

3.3. Proposed Synergetic Controller

To eliminate any steady state errors in the d-axis variables, the following macro-variable is proposed to maintain a constant value for the d-axis current i_d at 0.

$$\psi_1 = K_1 i_d + K_2 \int i_d dt \tag{42}$$

The addition of the gain K_1 will control the peak magnitude of i_d during the transient periods. The addition of an integral term removes any steady state error and the gain K_2 controls the speed of convergence during the transient periods. Similarly, the same steps from section 3.1.2 are followed to compute a control law based on the proposed macro-variable in Eq. (42). The dynamics of the ψ_1 are described by Eq. (30). The term $\dot{\psi}_1$ is computed.

$$\frac{d\psi_1}{dt} = K_1 \frac{di_d}{dt} + K_2 i_d \tag{43}$$

Substituting the expression of $\frac{di_d}{dt}$ from Eq. (25) into Eq. (43), the expression for $\frac{d\psi_1}{dt}$ can be further expanded.

$$\dot{\psi}_1 = \frac{K_1}{L_d}[V_d - Ri_d + L_q i_q \omega_e] + K_2 i_d \tag{44}$$

Substituting with the results of Eq. (42) and (44) into (30) and solving for V_d, the control law V_d^* can be computed as follows:

$$T_d\left[\frac{K_1}{L_d}(V_d - Ri_d + L_q i_q \omega_e) + K_2 i_d\right] + K_1 i_d + K_2 \int i_d dt = 0 \tag{45}$$

$$V_d - Ri_d + L_q i_q \omega_e = -\frac{L_d}{T_d} i_d - \frac{K_2}{K_1}\frac{L_d}{T_d}\int i_d dt - \frac{K_2}{K_1} L_d i_d \tag{46}$$

$$V_d = -\frac{L_d}{T_d} i_d - \frac{K_2}{K_1}\frac{L_d}{T_d}\int i_d dt - \frac{K_2}{K_1} L_d i_d + Ri_d - L_q i_q \omega_e \tag{47}$$

Hence, the expression for the command law V_d^* is given by Eq. (47). This command maintains i_d to remain 0 despite any discrepancies between actual and assumed system parameters. The macro-variable ψ_2 controlling the q-axis command voltage V_q^* remains

unchanged. Only the gain subscripts are updated to be as follows.

$$\psi_2 = K_3(\omega - \omega_{ref}) + K_4 i_q + K_5 \int (\omega - \omega_{ref}) dt \tag{48}$$

Chapter 4: Regenerative Braking

Electric vehicle braking can be done in different ways; mechanically or electrically. In mechanical braking, friction forces are used to dissipate the kinetic energy in the wheels and all of this energy is lost in the form of heat due to friction forces. However, in electrical braking, the kinetic energy of the motor can be harvested with the proper switching sequence of the three-phase inverter in order to redirect the current flowing in the motor windings back to the source or integrated hybrid energy storage system. It should be noted that not all energy can be recovered during the braking process as there exists some boundaries along the torque-speed plane where regenerative braking occurs [37]. In most applications, this regenerated current charges a supercapacitor module or the vehicle's battery connected to the DC side of the inverter through a DC-DC converter. In the literature, some studies avoid the use of the DC-DC converter to avoid any additional costs. Therefore, the inverter's switches and the motor windings are used to perform as a buck converter [38]. This proper switching sequence is explained on a DC motor circuitry for simplicity. AC drives adopt the same concept in three-phase windings.

4.1. Regenerative Braking of DC Motor

When supplied with a full-bridge DC-DC converter (H-bridge), a DC motor has four quadrant operations which include driving and braking in each direction. The braking mode is divided into two periods which will be illustrated later in this section. To simplify the system analysis, it can be assumed that a DC motor is connected to a supercapacitor through a DC-DC converter. This supercapacitor is used to drive the motor and store the regenerated energy. The EV's operation is divided into two modes; driving mode and braking mode.

1. Driving mode: In this mode, the source feeds the DC motor through the DC-DC converter which is controlled by a PWM signal to control the speed of rotation. In this mode of operation, electrical energy from the supply is converted to kinetic energy in the motor inertia. Figure 14 shows the direction of current flow in the

circuit during this mode of operation. The converter switches Q_1 and Q_3 are conducting and the motor is driven in its forward direction. The dynamics of the DC motor are described by Eq.(18) and (19). It can be seen from the mathematical model of a DC motor that the input voltage is translated into kinetic energy in the form of the generated torque.

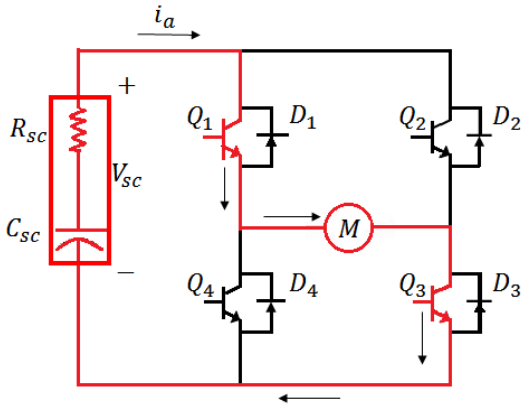

Figure 14: Direction of current flow in driving mode.

2. Regenerative braking mode: In this mode of operation, all of the converter switches are opened, and only Q_4 is controlled with a PWM signal. The motor current decreases gradually until it reaches zero. Since all of the switches are opened, the supply voltage is cut off the motor. Rewriting the equation, it can be seen that the back EMF generated acts as a voltage source, and the current will change its direction to generate an opposing torque and stop the motor.

$$0 = R_a i_a + L\frac{di}{dt} + K_b \omega \tag{49}$$

$$K_b \omega = -R_a i_a - L\frac{di}{dt} \tag{50}$$

The operation of Q_4 is divided into two intervals; ON-time period where Q_4 is conducting current and OFF-time period where Q_4 is open.

(a) ON-time period: During this period, Q_4 is closed and the current circulates in the closed loop flowing through Q_4 and D_3 and back through the motor's

armature. Figure 15 shows the direction of current flow in this state. During this period, the armature's inductance is charged, and it stores energy acting similarly to the operation of a boost converter.

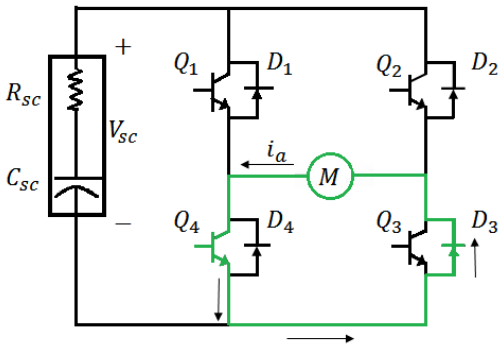

Figure 15: Direction of current flow while Q4 is ON.

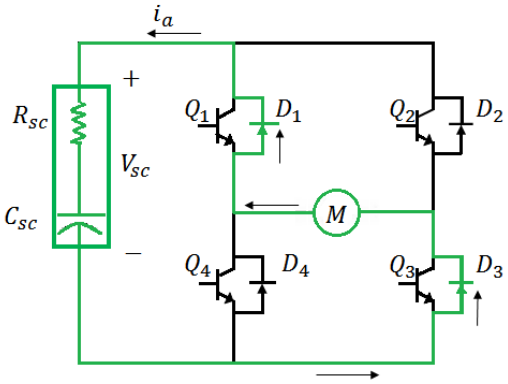

Figure 16: Direction of current flow while Q4 is OFF.

(b) OFF-time period: During this period, Q_4 is open and the current finds its path back to charge the supercapacitor through D_1 and D_3. The motor inductance also discharges its energy back to the capacitor. This operation is similar to that of a boost converter. Figure 16 shows the direction of current flow during this interval. Regenerative braking is achieved in this mode of operation.

4.2. Regenerative Braking of PMSM

For an AC motor drive, the power switches of the three-phase inverter can be utilized to harvest mechanical energy and feed it back to the DC source [39]. The researchers use the three-phase inverter as a bidirectional DC-AC converter that controls energy flow in both directions between the power source and the motor in case of driving and regenerative braking modes of operation. They propose three control techniques to operate in regenerative braking mode depending on the number of switches controlled. The first control scheme, named "single-switch control", uses only one of the three lower switches to control the path of the current in the motor windings. The other

switches remain open. This is similar to the operation of a DC-DC converter (H-Bridge) controlling a DC motor in regenerative braking as explained in the previous section. The second control type, named "two-switches control", uses a lower switch and a higher switch of the three-leg inverter and the remaining switches remain open. Finally, the "three-switches control" scheme uses all three lower switches to control the path of the current. The upper switches remain open at all times. Their results show that the single-switch and three-switches control schemes are most suitable for braking at high speeds, or during deceleration, while the two-switches control scheme is most suitable for low-speed, high-torque braking, such as in emergency brakes. This study shows that multiple switching schemes of a three-phase inverter can be used to operate in the regenerative braking mode.

In [37], a regenerative braking analysis is performed to determine the minimum and maximum applied torques that identify the regenerative braking region on the speed-torque plane. As shown in Figure 17, the speed-torque plane is divided into four sectors; In forward motoring, the motor speed and torque are both positive. In reverse braking, the applied torque is positive while the speed is negative. In reverse driving, both of the applied torque and speed are negative. Finally, in forward braking, the speed is positive, and the applied torque is negative. Regenerative braking lies in the fourth quadrant where a negative torque is applied to stop the motor.

By balancing the input electrical power with the output power of the PMSM motor, as well as using some optimization laws, the researchers were able to find the command torques that specify the lower and maximum boundaries of regenerative braking [37]. The input power and the output electromagnetic power of the PMSM are given by Eq. (51,52). The expression for T_{em} can be expanded with the formula given by Eq. (15).

$$P_{in} = V_d i_d + V_q i_q \tag{51}$$

$$P_{em} = T_{em}\omega \tag{52}$$

The electric machine power losses are given by Eq. (53) below:

$$P_{loss} = i_d^2 R + i_q^2 R \tag{53}$$

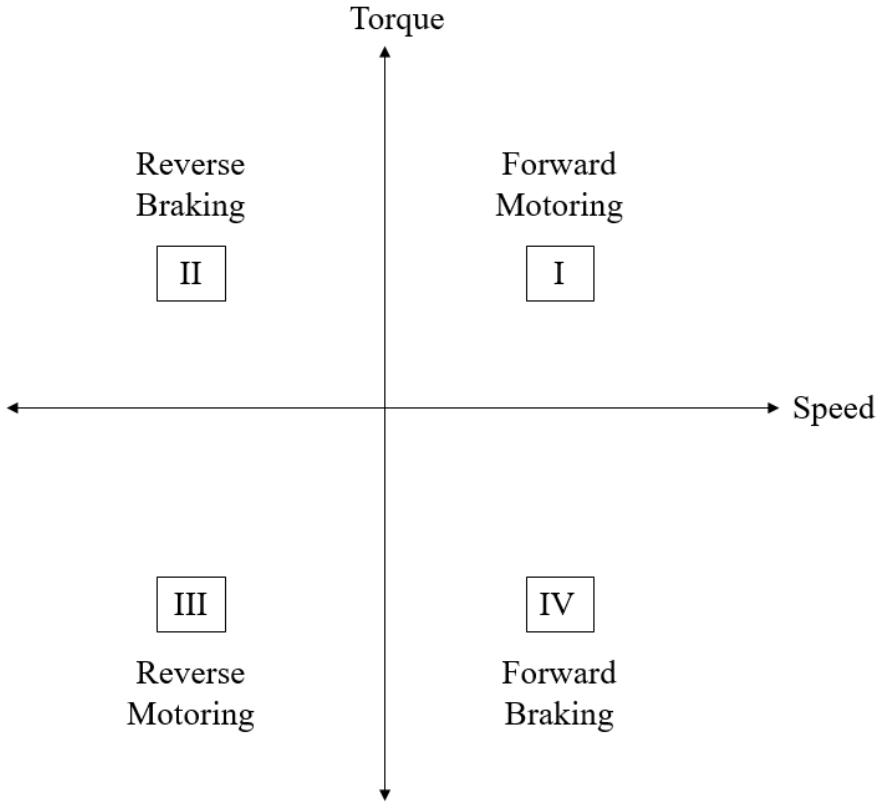

Figure 17: Speed-torque plane.

Balancing the input and output power, the following expression for the input power can be formulated.

$$P_{in} = P_{em} + P_{loss} \tag{54}$$

$$P_{in} = \frac{3}{2}\frac{P}{2}\lambda_{PM} i_q \omega + R(i_d^2 + i_q^2) \tag{55}$$

To find the regenerative braking boundaries, P_{in} is set to 0 in Eq. (55), indicating that no power is drawn from or to the DC source. The solution of i_q in terms of i_d can be found.

$$i_q = \frac{-\frac{3}{2}\frac{P}{2}\lambda_{PM}\omega \pm \sqrt{(\frac{3}{2}\frac{P}{2}\lambda_{PM}\omega)^2 - 4R^2 i_d^2}}{2R} \tag{56}$$

The equivalent electromagnetic torque can be found using Eq. (15)

$$T_{em} = \frac{3}{2}\frac{P}{2}\lambda_{PM}\frac{-\frac{3}{2}\frac{P}{2}\lambda_{PM}\omega \pm \sqrt{(\frac{3}{2}\frac{P}{2}\lambda_{PM}\omega)^2 - 4R^2 i_d^2}}{2R} \tag{57}$$

This expression describes the electromagnetic torque inside the regenerative braking region. To find the boundaries of this region, the torque is minimized as follows.

$$\frac{dT_{em}}{di_d} = 0 \tag{58}$$

$$i_d = 0 \tag{59}$$

By substituting this result in Eq. (56), the value of the equivalent i_q can be evaluated.

$$i_q = 0 \quad \text{or} \quad iq = -\frac{3P\lambda_{PM}}{4R}\omega \tag{60}$$

The equivalent minimum torque and maximum torques defining the regenerative braking boundaries are defined by Eq. (61).

$$T_{em} = 0 \quad \text{or} \quad T_{em} = -\frac{(\frac{3}{4}P\lambda_{PM})^2}{R}\omega \tag{61}$$

By finding the local minimum points to minimize the input power to the motor, the maximum current absorbed by the DC source during regenerative braking can be found.

$$\nabla P_{in} = \begin{bmatrix} \frac{\partial P_{in}}{\partial i_d} \\ \frac{\partial P_{in}}{\partial i_q} \end{bmatrix} = \begin{bmatrix} 2Ri_d \\ \frac{3}{2}\frac{P}{2}\lambda_{PM}\omega + 2Ri_q \end{bmatrix} \tag{62}$$

The minimum power is obtained by setting the gradient to zero and solving for each of i_d and i_q as illustrated in Eq. (63) and (64) respectively. The equivalent electromagnetic torque is given by Eq. (65).

$$i_d = 0 \tag{63}$$

$$i_q = -\frac{3P\lambda_{PM}}{8R}\omega \tag{64}$$

$$T = -\frac{9P^2\lambda_{PM}^2}{32R}\omega \tag{65}$$

This electromagnetic torque guarantees maximum absorbed power and maximum absorbed current by the DC source during the regenerative braking process.

4.2.1. Regenerative Braking Using FOC. Under FOC, regenerative braking is achieved by operating the PMSM in torque control mode. The current controllers are given a command i_d^* and i_q^* equal to the results found in Eq. (63) and (64) respectively. This will brake the motor in the regenerative braking region and guarantee maximum current harvested from the motor's rotation. For that reason, the speed control loop is removed from the FOC controller and instead the command currents i_d^* and i_q^* are fed to the current regulators right away. Figure 18 shows the block diagram of the FOC in regenerative braking mode.

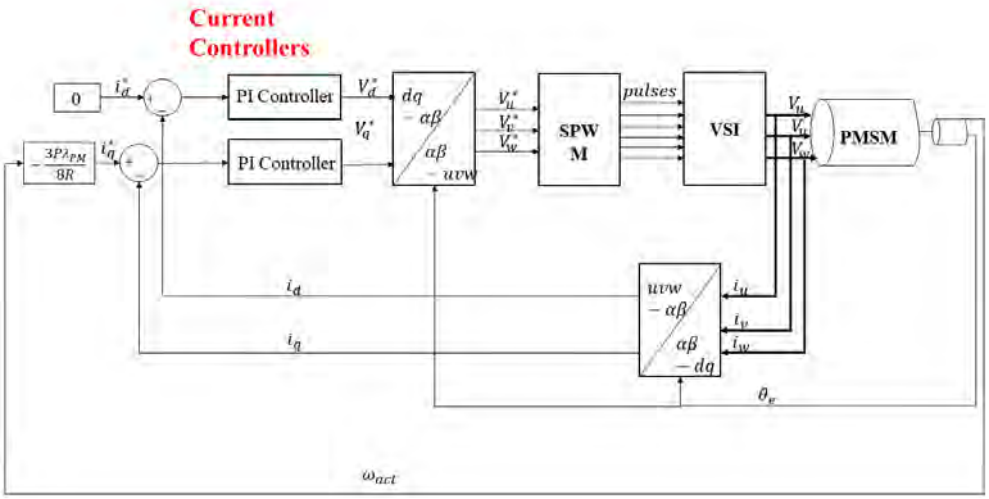

Figure 18: FOC block diagram in regenerative braking mode

4.2.2. Regenerative Braking Using SC. Two macro-variables are defined for the synergetic controller to operate the PMSM in regenerative braking mode. The design of these macro-variables adopts the same approach to control i_d and i_q to follow the references described earlier in Eq. (63) and (64), respectively. Figure 19 shows the block diagram of the synergetic controller in regenerative braking mode.

4.2.2.1. Direct Axis Macro-variable. The proposed macro-variable is described by Eq. (66). The reference i_d^* is equal to 0. Therefore, the gain K_1 forces i_d to 0 and reduces the error between i_d and its reference; since the control law tends to force the

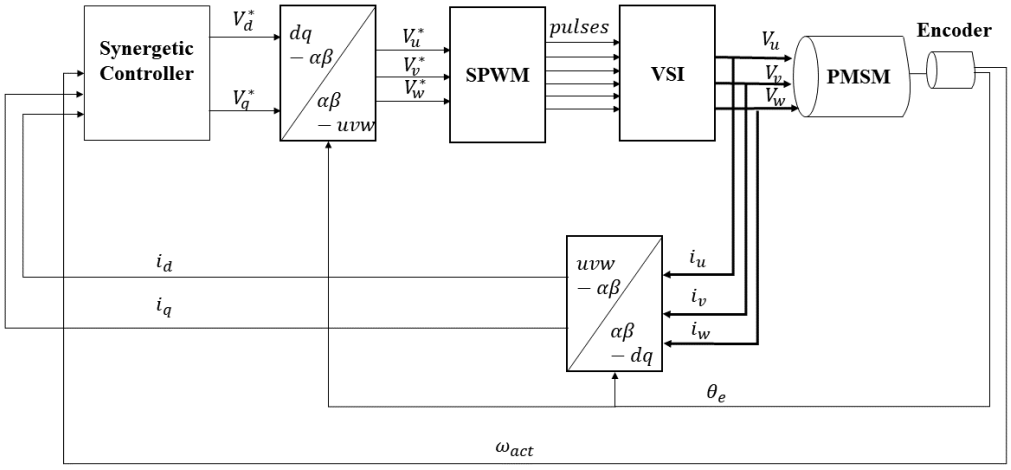

Figure 19: Synergetic controller block diagram in regenerative braking mode

macro-variable to converge to 0 as explained in section 3.1.2. The integral term is added to eliminate any steady state error.

$$\psi_1 = K_1 i_d + K_2 \int i_d dt \tag{66}$$

The dynamic response of this macro-variable is governed by Eq. (67).

$$T_d \frac{d\psi_1}{dt} + \psi_1 = 0 \tag{67}$$

Where T_d is the convergence time of ψ_1. Following the design procedure explained in section 3.1.2, the control law V_d^* is derived as illustrated in Eq. (68). Applying this voltage V_d will ensure that i_d remains 0.

$$V_d = -\frac{L_d}{T_d} i_d - \frac{K_2}{K_1}\frac{L_d}{T_d} \int i_d - \frac{K_2}{K_1} L_d i_d + R i_d - L_q i_q \omega_e \tag{68}$$

4.2.2.2. Quadrature Axis Macro-variable. The proposed macro-variable to control i_q is given by Eq. (69), where the reference i_q^* is the i_q current that allows maximum current absorption by the DC supply as shown in Eq. (64). The dynamics of

the macro-variable are defined by Eq. (70), where T_q is the convergence time of ψ_2.

$$\psi_2 = K_3(i_q - i_q^*) + K_4 \int (i_q - i_q^*)dt \tag{69}$$

$$T_q \frac{d\psi_2}{dt} + \psi_2 = 0 \tag{70}$$

To evaluate the command V_q^*, the design procedure explained in section 3.1.2 is followed. First, the term $\frac{d\psi_2}{dt}$ is evaluated by differentiating Eq. (69) as shown in Eq. (71). It should be noted that the term $\frac{di_q}{dt}$ is not constant, since it is a function of the motor's angular speed. The derivative of this term is shown in Eq. (72)

$$\frac{d\psi_2}{dt} = K_3(\frac{di_q}{dt} - \frac{di_q^*}{dt}) + K_4(i_q - i_q^*) \tag{71}$$

$$\frac{di_q^*}{dt} = -\frac{3P\lambda_{PM}}{8R}\frac{d\omega}{dt} \tag{72}$$

By substituting the expressions of $\frac{di_q}{dt}$ and $\frac{di_q^*}{dt}$ with Eq. (26) and (72) respectively, and by rearranging the terms, the expression for the command law V_q^* is evaluated and given by Eq. (73). Applying this voltage will generate a reverse torque given by Eq. (65) that forces the motor to operate under regenerative braking mode.

$$V_q^* = L_q\frac{di_q^*}{dt} - \frac{K_4}{K_3}L_q(i_q - i_q^*) - \frac{L_q}{T_q}(i_q - i_q^*) - \frac{K_4}{K_3}\frac{L_q}{T_q}\int (i_q - i_q^*)dt + Ri_q + L_d i_d \omega_e + \omega_e \lambda_{PM} \tag{73}$$

Chapter 5: Experimental Analysis and Results

5.1. Experimental Setup

Figure 20 shows the topology of the mechanical setup in the lab. The system consists of a PMSM, which is controlled using a MYWAY MWINV-9R144 inverter. The inverter switches are controlled using the dSPACE 1103 board. The PMSM is coupled with a Bühler DC Motor through flexible couplings and additional disc inertia mounted on the same shaft. The DC motor acts as a mechanical load and is controlled using a DC-DC converter, which in turn is controlled using a dSPACE 1104 board. Two encoders are used; one incremental encoder is directly connected to the DC motor side, and the other encoder is a sine/cosine connected to the PMSM side.

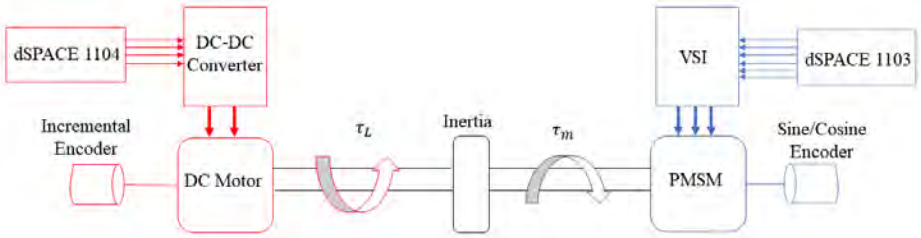

Figure 20: Topology of the experimental setup

Figure 21 shows the experimental system inside the lab.

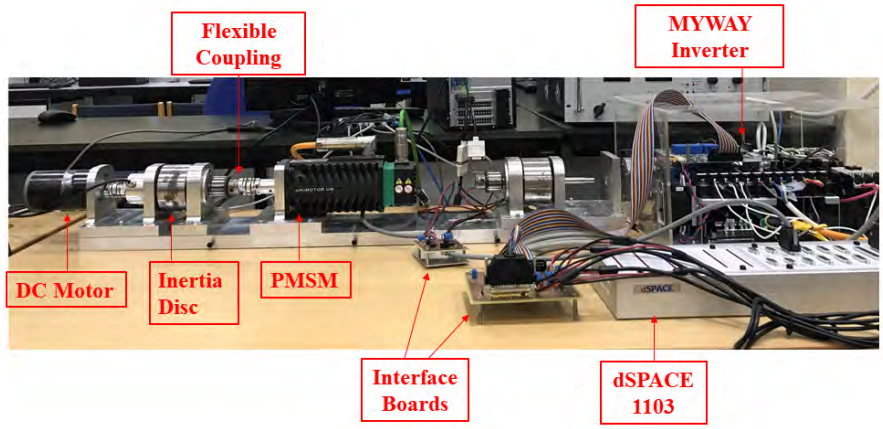

Figure 21: Experimental system setup

5.2. Permanent Magnet Synchronous Motor

In this work, the main motor of choice for the drive system is the permanent magnet synchronous motor (PMSM). This motor provides several advantages, such as compact sizes, high power ratings and less losses since the rotor field is generated by a set of permanent magnets fixed on the rotor surface. Therefore, there are no current losses in the rotor, which means less heat dissipation. Therefore, costly cooling systems are not needed to maintain the temperature of the motor during operation. The motor of choice is a Unimotor UM series from EMERSON Industrial Automation. Table 1 summarizes the specifications of the motor [40].

Table 1: PMSM parameters

Variable	Value	Unit
Torque Constant (K_t)	1.6	Nm/A
EMF Coefficient (K_e)	98	V/krpm
Rated Torque(τ_{rated})	3.9	Nm
Stall Current (I)	2.7	A
Rated Speed (ω_{rated})	3000	RPM
Rated Power (P_{rated})	1.23	kW
Stator Resistance (R_{pk-pk})	6.8	Ohms
Stator Inductance (L_{pk-pk})	24.3	mH
Inertia (J)	2.5	kgcm^2
Poles (P)	6	-

5.2.1. Motor Feedback. The PMSM is attached to a SinCos encoder acting as the feedback device to measure the motor speed and position. The analog encoder provides high resolution and accurate measurements which are necessary for field orientation in FOC. An interface board is designed to interface the analog encoder with dSPACE 1103 since it dedicates a channel to analog encoders. dSPACE receives the Sine and Cosine waveforms output from the encoder and translates these signals into pulses. The motor speed and position can then be computed in software. However, dSPACE requires the input signals to have amplitude of 1 V_{pp} and a mean value of 0 [41]. The raw output data from the encoder has amplitude 1 V_{pp} but a mean value of $2.5V$. Therefore, an interface board is designed to interface the SinCos encoder with the

dSPACE board. The interface board shifts the encoder output signals to remove the DC offset and acquire waveforms with $0V$ mean value. Figure 22 shows the circuit diagram of the interface board. It subtracts the DC offset value (2.5V) from both signals using differential amplifiers. The output is fed to a voltage follower to avoid any voltage fluctuations due to impedance drop. The output of the voltage followers is directly input to dSPACE.

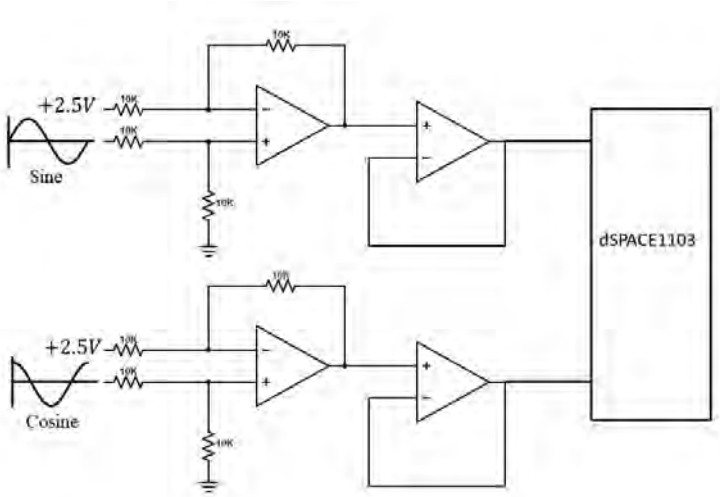

Figure 22: Circuit diagram of the encoder interface board

The frequency of the generated sine and cosine waves depends on the motor speed. The encoder generates 1024 SinCos periods/revolution. This can be used to calculate the output frequency using the formula given by Eq. (74) [42].

$$f(Hz) = \frac{\text{periods}}{\text{rev}} \times \text{speed(rpm)} \times \frac{1}{60} \tag{74}$$

Once the signals are received, dSPACE divides these Sine and Cosine waves into 256 segments and converts them into pulses. Finally, the motor position and speed are found by dividing by the number of SinCos periods as shown in Eq. (75) and (76).

$$\theta(rad) = \text{pulses} \times \frac{2\pi}{1024} \tag{75}$$

$$\omega(rad/s) = \Delta\theta \times \frac{1}{Ts} \tag{76}$$

5.2.2. Motor Alignment. Induction motors rotate with a slip angle between the stator field and the rotor field. This is contrary to the case of PMSM where the rotor field is generated by a permanent magnet, and this magnetic field aligns itself with the stator field without any slip between both fields. Consequently, this stresses the importance of finding the absolute position of the rotor field to obtain field orientation. The SinCos encoder is an analog incremental encoder; therefore, it is not capable of finding the absolute position of the rotor. A resolver or an absolute encoder is needed instead. Nonetheless, these sensors are costly. Another solution is proposed in [43] to operate the PMSM with a SinCos encoder. Initially, the rotor flux vector is placed arbitrarily depending on the mechanical position of the rotor. The main idea is to align the stator current vector $\vec{I}_s$ with the rotor flux vector $\vec{\Psi}$ along the α axis. Hence, the angle between both vectors will be 0. The rotor position read from an incremental encoder can now be used as the actual absolute position of the motor. This can be done by connecting phase U of the PMSM with the positive terminal of the DC link and connecting phases V and W to the negative terminal of the DC link as shown in Figure 23. The application of a constant DC voltage will create a constant current flowing in

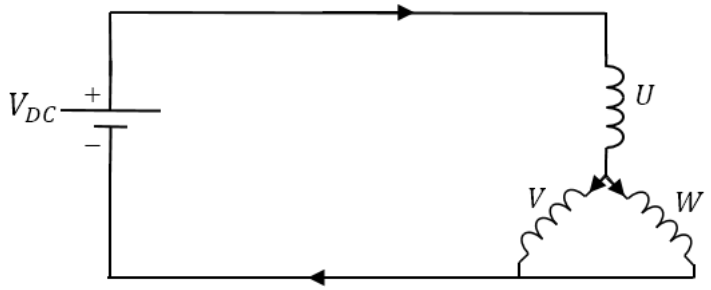

Figure 23: Configuration of PMSM for alignment

all phases, and will place the stator current vector along the α axis. Since the current flowing in each of the motor phases is constant, this vector is stationary and will remain fixed along the α axis. This will in turn force the rotor flux vector to align itself with the stator current vector. Therefore, the rotor moves in the direction of the stator magnetic

field until both vectors are aligned which sets the angle between both vectors to 0 as shown in Figure 24. This, in other words, means that the d-axis is aligned with the α axis, and the initial electrical angle of the rotor is 0. By this, the readings of an incremental encoder become sufficient to apply field orientation.

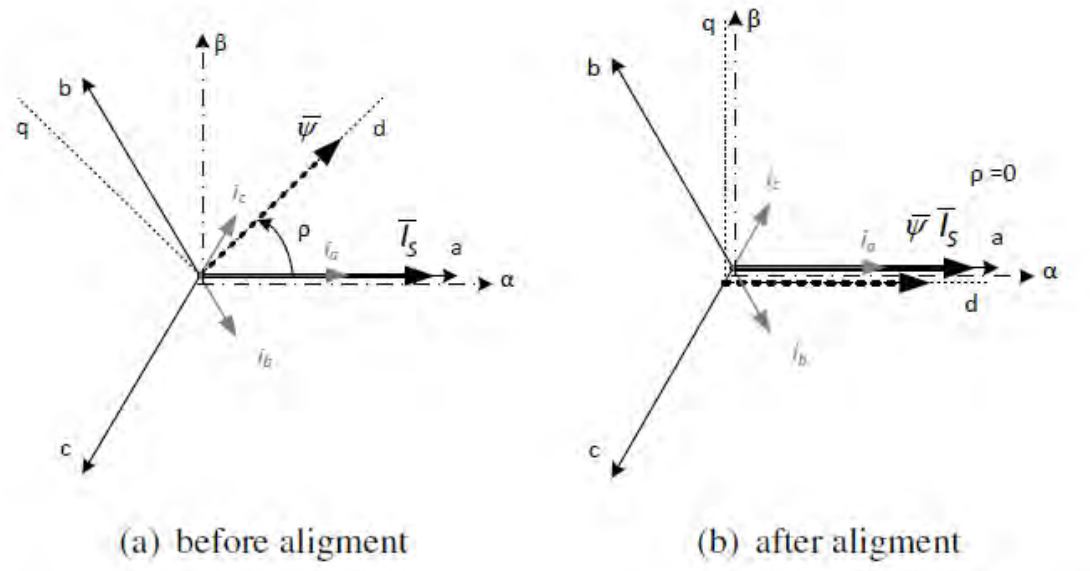

Figure 24: Alignment of rotor flux [43]

5.3. Inverter

5.3.1. Three-Phase Inverter. The MYWAY three-phase inverter is supplied with a three-phase voltage source through a 3ϕ rectifier bridge. A capacitor is connected across the DC-bus to maintain a constant DC-bus Bus voltage. The inverter provides current and voltage sensors to measure the corresponding voltages and currents of each of the DC Bus, phases U and W. The two-level inverter consists of 6 IGBT switches that are controlled using gating signals transmitted from dSPACE 1103 board through a custom designed interface board. Figure 25 shows the circuit diagram of the inverter [44].

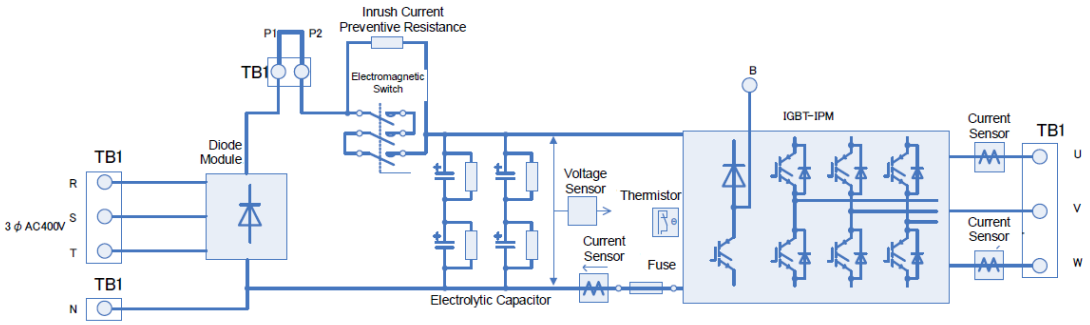

Figure 25: MYWAY Inverter block diagram [44]

5.3.2. dSPACE Interface Board. An interface board is designed to interface the MYWAY inverter with dSPACE 1103. The interface board serves three purposes; reading and sending I/O signals received or sent from/to the inverter and inverting the output PWM signals, since the IGBT switches are active low. Finally, the board adds delays to the PWM signals as the switches require a minimum of 4 μs as deadtime delay between each two inverted switches in each inverter leg.

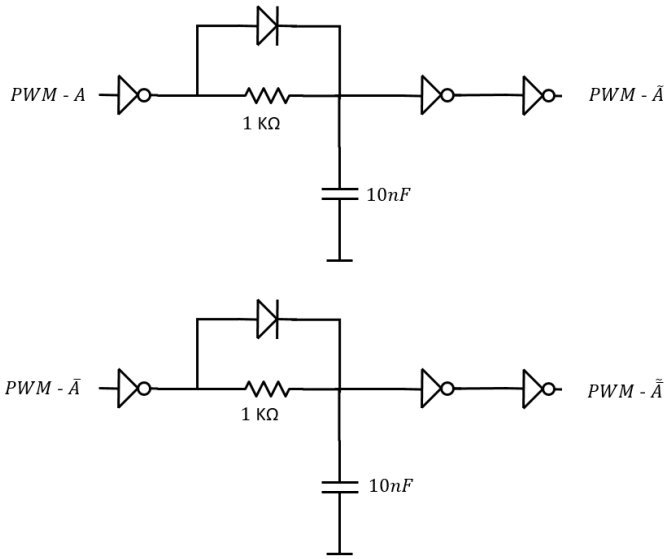

Figure 26: Interface board circuit diagram

Figure 26 shows the circuit diagram of the deadtime delay circuit. The input signals A and $\bar{A}$ are the two complementary PWM signals sent to one inverter leg, and the output signals $\tilde{A}$ and $\tilde{\bar{A}}$ are the delayed signals with deadtime delay of $5-7$ μs. The

input PWM signals generated from software are active high signals. The addition of an extra inverting gate was to ensure that all signals are active low. Figures 27 and 28 show the delayed signals for each of the rising and falling edges respectively. The delay was designed by selecting the proper values of the resistors and capacitances used. Therefore, there were some difficulties in obtaining a perfectly symmetric delay between rising and falling edges. The final rising edge delay was 6.8 μs and the falling edge was 5 μs. This asymmetry is caused by the capacitor; since it might take a relatively longer time to charge than to discharge.

Figure 27: Rising edge dead-band delay

5.3.3. Inverter Control. Various techniques to control the switching of the inverter exist in the literature, such as Six Step operation, Space Vector Pulse Width Modulation (SVPWM) and Sine Triangle Pulse Width Modulation (SPWM). In this study, SPWM is used to generate 6 PWM pulses that control the switching of the inverter. The main idea of SPWM is to compare 3-phase sinusoidal reference signals, usually generated by the controller, to a triangular carrier signal. Both, the input sinusoidal references and the obtained PWM signals are shifted 120° apart. The obtained PWM signals are fed to the upper switches of each inverter leg. Their complements are

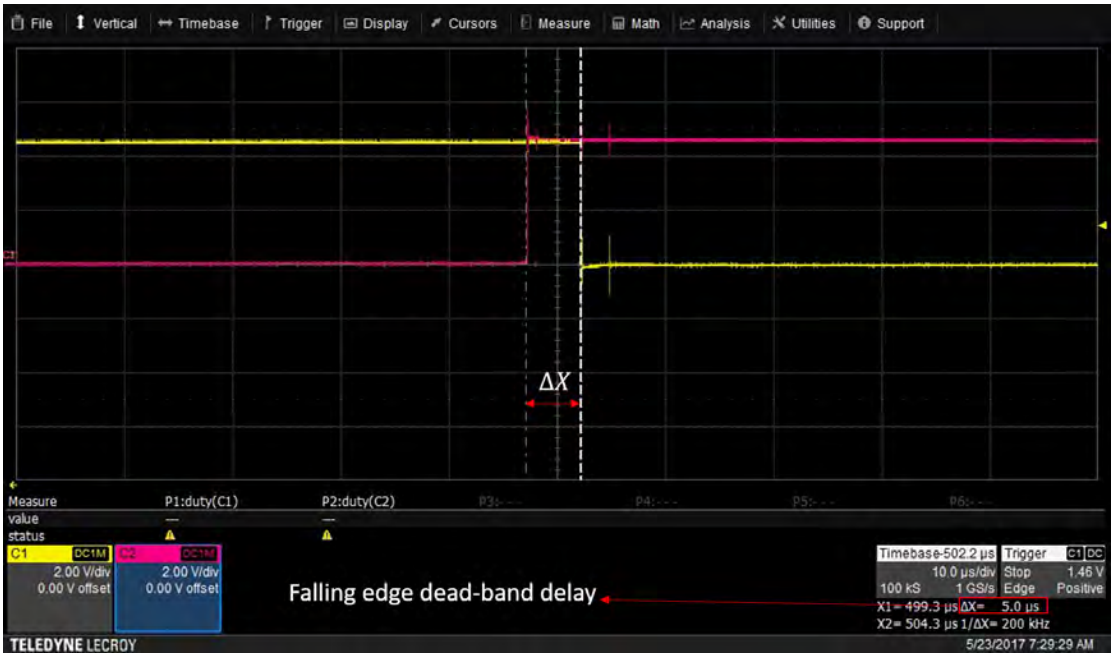

Figure 28: Falling edge dead-band delay

in turn fed to the lower switches of each inverter leg. Due to switching losses, some harmonics are added to the output waveforms. However, the fundamental component of these waveforms will have a sinusoidal shape. The fundamental component of the output voltage will follow the approximation given by Eq. (77), when modulation index is kept below 1 [45].

$$V_{RMS} = 0.612 m_a V_{dc} \tag{77}$$

Where m_a is the modulation index. The modulation index is the ratio between the peak of the sinusoidal reference signals and the peak of the triangular carrier signal. The output speed of the motor will change upon changing the frequency and magnitude of the input reference signals. This is taken care of by the controllers in closed loop speed control. The output switching frequency depends on the frequency of the triangular carrier signal. Increasing the switching frequency will reduce current ripples and result in cleaner waveforms and less switching losses.

5.4. Field Oriented Control

This section presents the experimental results of the motor drive system with FOC. Being the most commonly used and robust controller in motor drive applications, FOC is used as a benchmark to assess the performance of the synergetic controller. In this section, the results of the FOC are analyzed for different operating conditions, including the response to step speed references and the response to sudden load variation. The experimental procedure goes as follows. Initially, as the motor is at rest, a speed step input of 500 RPM is introduced and then is followed by another step input of 500 RPM. Once the motor speed settles at 1000 RPM, a load torque of 0.6 N.m is applied using the DC motor attached on the PMSM shaft as explained in Figure 20. The load torque is then removed, and after the motor speed settles back, the speed reference is set to 0 to bring the motor to rest. This event is referred to as braking in the upcoming analysis. Figure 29 shows the speed response of the motor as well as the speed reference and a description of the events in this experiment.

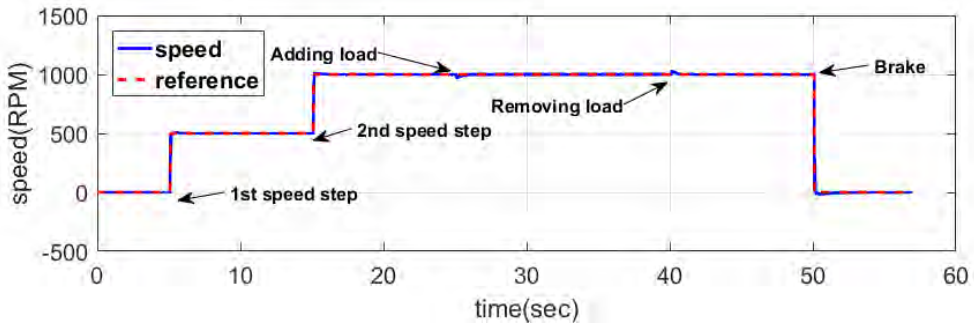

Figure 29: Speed reference and experimental procedure description

The motor speed successfully tracks its reference at all times. When the load is applied, the speed drops for a short period of time because of the added torque. On the other hand, the controller regulates the generated electromagnetic torque to overcome the added load. Hence, the speed returns back to its reference as desired. Upon removing the load, the scenario is reversed. The electromagnetic torque generated is higher than the required amount of torque to overcome friction since the load torque has become 0. Thus, the speed of the motor increases for a short period of time once the load

is removed. The controller regulates the output electromagnetic torque, and the speed returns back to its reference. Figure 30 shows the motor speed during the transient periods. The figure shows that the speed settles to its reference in less than 0.1 seconds. The

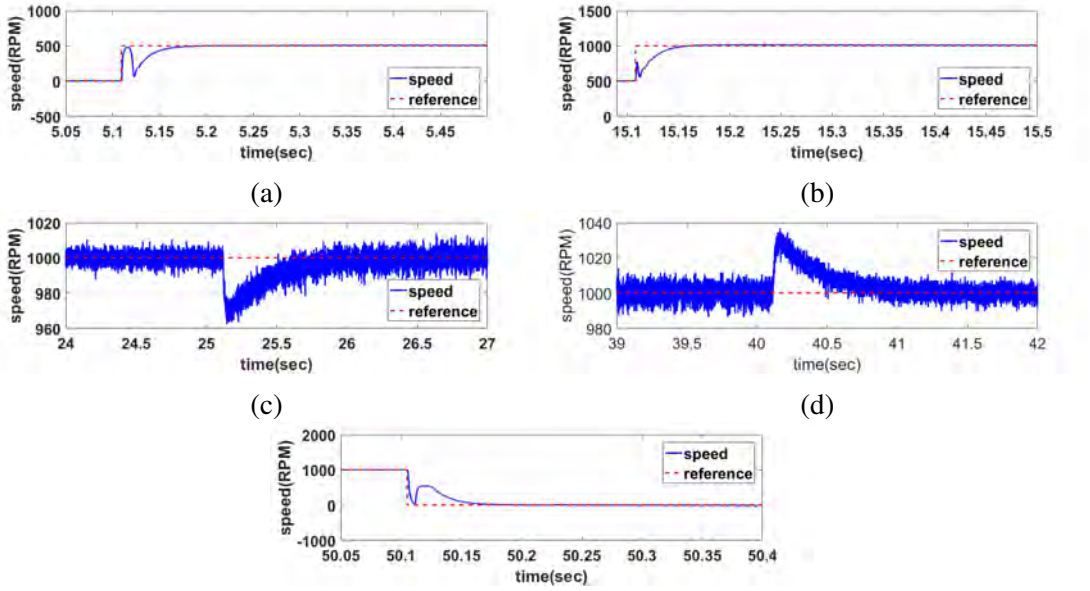

Figure 30: Zoomed views of each transient period of the motor speed response under FOC (a) 1st speed step (b) 2nd speed step (c) Applying load (d) Removing load (e) Braking

oscillation in the transient response is caused by the flexible coupling between the motor shaft and the encoder. Figure 31 shows the response of the quadrature axis current (i_q). Since the main objective of FOC is to decouple the system, i_q is responsible for

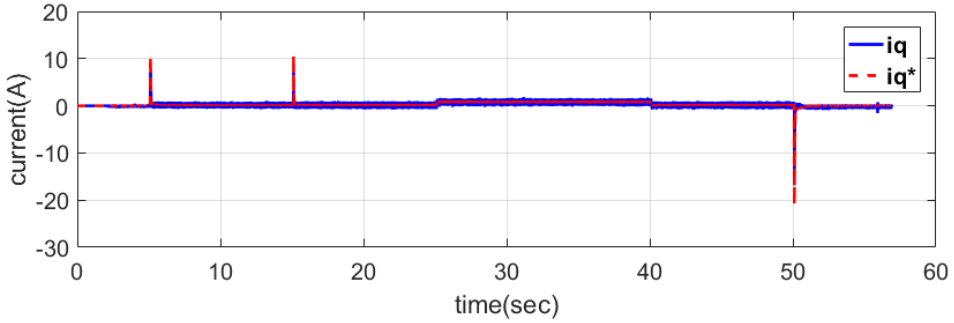

Figure 31: i_q response

controlling the motor torque. Figure 31 shows that the generated command i_q^* increases

during the transient parts to accelerate the motor. Once the speed of the motor settles to its reference, the i_q^* returns to a steady state value which is the amount of current needed to generate enough electromagnetic torque to overcome frictional losses. If a load is added, i_q^* increases to account for the extra torque. When the load is removed, the generated i_q^* decreases again. When the braking occurs, a negative i_q^* is generated to induce a negative torque to stop the motor. Figure 32 illustrates the transient periods of i_q. It shows that the actual i_q is always able to track the command i_q^*. The command

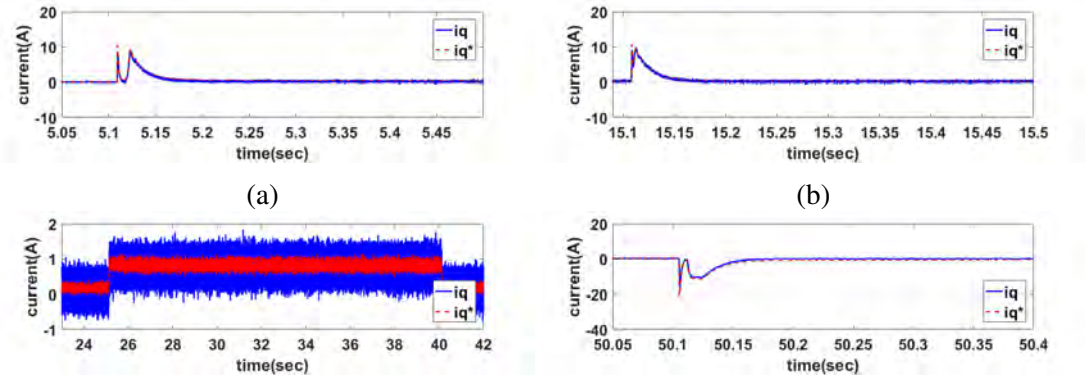

Figure 32: Zoomed views of each transient period of i_q response under FOC (a) 1st speed step (b) 2nd speed step (c) Applying and removing load (d) Braking

current is generated by the speed controller as demonstrated in the FOC block diagram in Figure 2. This explains the reason behind the fluctuations in the generated command current in transient periods.

In field orientation, the direct axis current (i_d) controls the machine's flux generated by the stator current. In case of PMSM, i_d is preferably controlled to always equal 0. This is to ensure that no flux weakening or demagnetization of the permanent magnets occurs. Permanent magnets are fixed on the machine's rotor; therefore, the rotor flux is not induced by the stator currents as opposed to the induction motor. But instead, the rotor flux is constant and is generated by the magnets fixed on the rotor. Flux weakening could be used to generate more power by the motor. In this work, flux weakening is not used and i_d is always controlled to be equal 0. Figure 33 shows the response of i_d. It indicates that i_d is maintained at 0 in steady state. During the speed transient, i_d experiences a jump before the controller forces it back to 0. It is worth

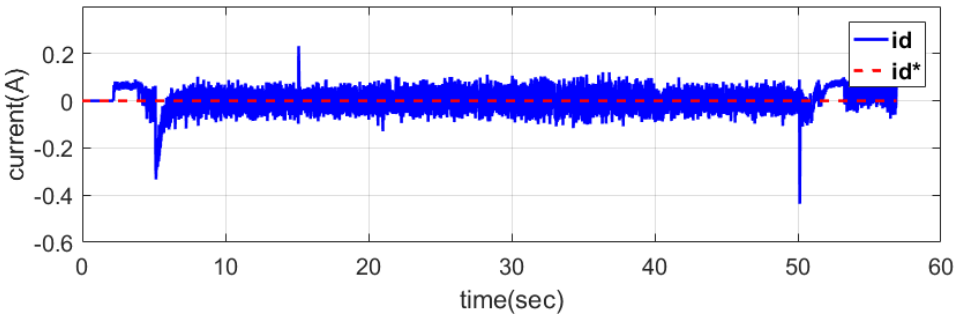

Figure 33: i_d response

noting that i_d shown in this figure is filtered by means of a low pass filter with a cutoff frequency of 20 Hz to reduce the current ripples and acquisition noise. Figure 34 shows the response of i_d in transient periods.

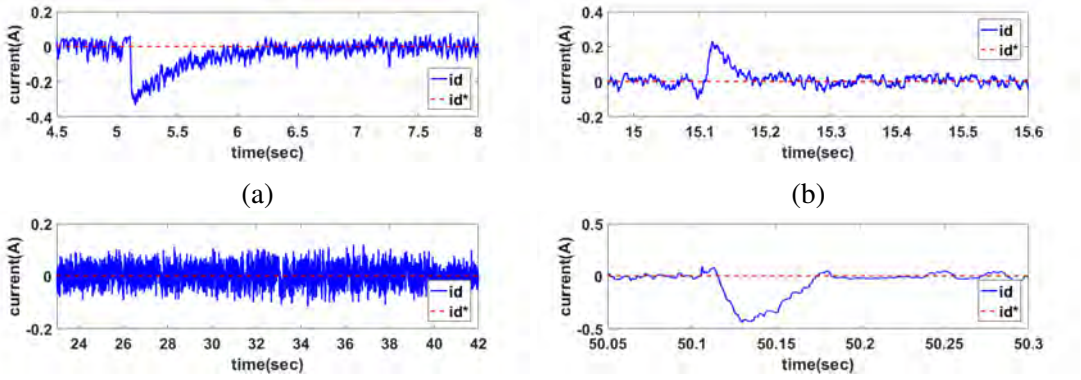

Figure 34: Zoomed views of each transient period of i_d response under FOC (a) 1st speed step (b) 2nd speed step (c) Applying and removing load (d) Braking

The three phase stator currents are shown in Figure 35. To show that the three phase currents are sinusoidal, the above figure is zoomed on a sample of the resulting waveforms. Data was also filtered by means of a moving average filter that computes the average of every 16 samples, to reduce the ripples.

Figure 36 shows the zoomed view of the three-phase stator currents. The figures show that the current has a sinusoidal waveform as expected, which proves that the transformation from three-phase reference plane to two-phase rotating frame is accurate.

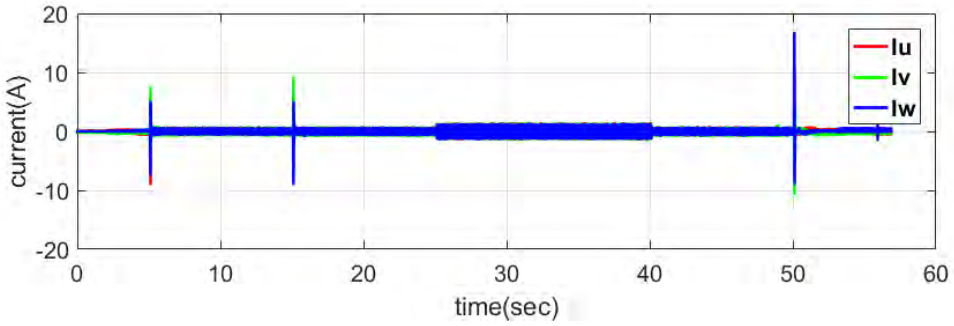

Figure 35: Three phase stator current response

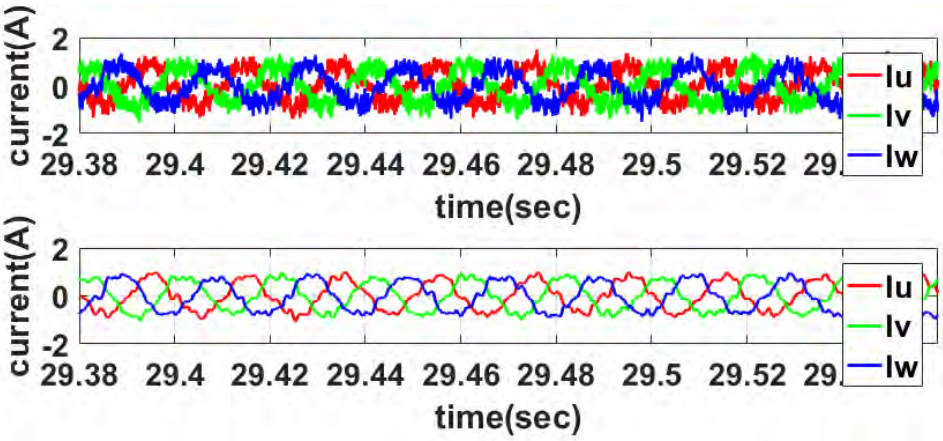

Figure 36: Zoomed views of the three phase stator currents (a) unfiltered (b) filtered

5.5. Synergetic Controller

5.5.1. Performance of The Proposed SC. In this section, the performance of the macro-variable (ψ_1) proposed in section 3.3 is compared to that of the original macro-variable derived in section 3.1.2.1. The old macro-variable is given the subscript A and the proposed macro-variable is given the subscript B. The performance of both macro-variables is tested by analyzing the behavior of $i_d(t)$ and $\psi_1(t)$. Since the q-axis macro-variable (ψ_2) is not altered, the speed response and $i_q(t)$ remain unchanged. In this experiment, the PMSM is subjected to a speed reference step of 500 RPM followed by another step to 1000 RPM. The DC motor load is switched on to apply a load torque of 0.6 $N.m$. The load torque is then removed, and the speed reference is brought back to 0. Figure 37 shows the speed reference and speed response of both controllers. Figure 38 shows the response of the macro-variable $\psi_1(t)$ resulting from both controllers

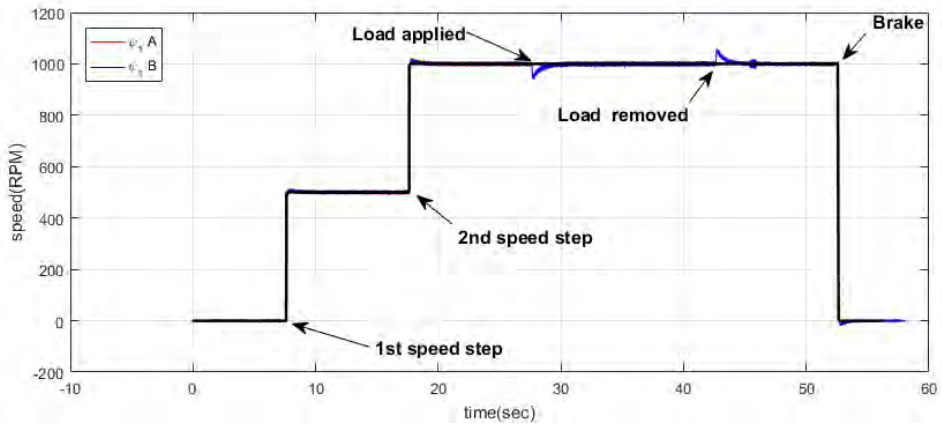

Figure 37: Speed reference description

throughout the entire experiment. The response of controller A is represented in red while the response of controller B is represented in blue. Figure 39 shows a zoomed view of each transient period. From these figures, it can be seen that the proposed controller improves the response of $\psi_1(t)$ significantly. The proposed controller (in blue) provides two advantages. First, the macro-variable ψ_1 always converges back to 0 after any transient period (with the exception of applying load which will be discussed later). As shown in the figures, ψ_1 for controller B (shown in red) always maintains a steady state error and does not converge to 0 as designed. Second, the magnitude of the peak values reached during the transients. Clearly, the peaks reached by the proposed controller B are much smaller than that with controller A. Table 2 summarizes the recorded peaks in the mentioned figures. It is shown that controller B improves the peak response of ψ_1 by approximately 90%. This shows that the proposed macrovarible improves the performance of the controller and the response of $\psi_1(t)$.

Table 2: Summary of recorded peak values of ψ_1

Period	ψ_{1A} Max. Amplitude	ψ_{1B} Max. Amplitude	Improvement (%)
1st speed step	-0.3077	-0.02526	91.79 %
2nd speed step	-0.8425	-0.08622	89.77 %
Applying/Removing load	-0.2829	-0.02407	91.40%
Brake	1.526	0.142	90.69%

As for the response of both controllers when the load is applied, there remains a steady state error in both cases. None of the macro-variables was able to converge

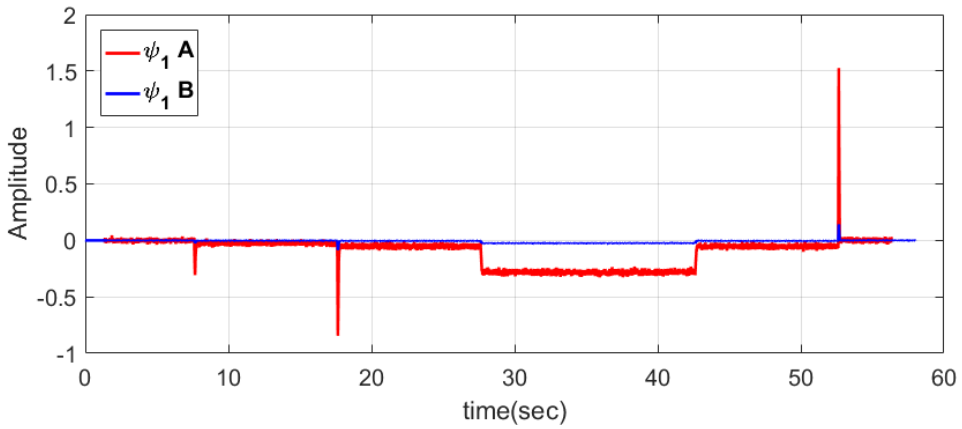

Figure 38: macro-variable ψ_1 response

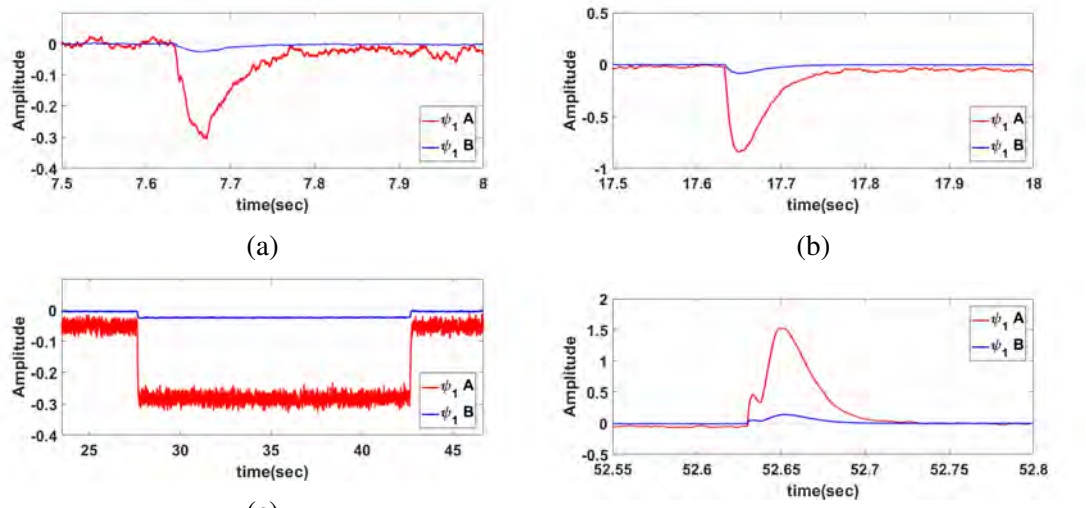

Figure 39: Zoomed views of each transient period of ψ_1 response (a) 1st speed step (b) 2nd speed step (c) Applying and removing load (d) Braking

back to 0. The reason is that the load torque was not accounted for in the controller synthesis. Hence, in this case, the extra load torque acts as a disturbance to the system. However, controller B was less affected by this disturbance compared to controller A and shows a steady state error much smaller than that of controller A. Looking at the behavior of $i_d(t)$, the same analysis is done. Figure 40 shows the response of $i_d(t)$ for the two controllers. The response of controller A is shown in red, and the response of controller B is shown in blue.

Figure 41 shows a zoomed view of each transient period of the $i_d(t)$ response. Studying the results shown in the above figures, it can be seen that i_d exhibits lower peak

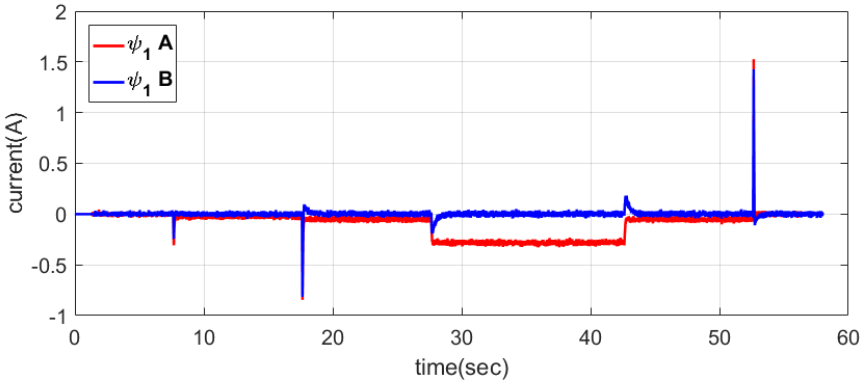

Figure 40: Direct axis current i_d response

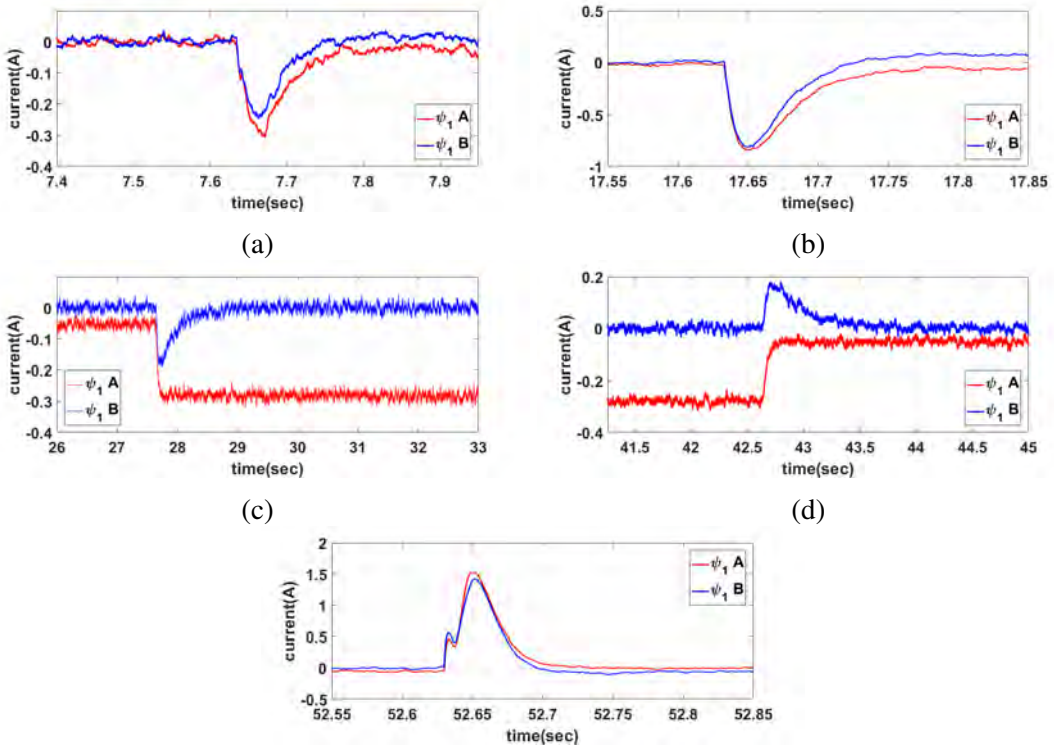

Figure 41: Zoomed views of each transient period of i_d response (a) 1st speed step (b) 2nd speed step (c) Applying load (d) Removing load (e) Braking

magnitudes in the case of controller B in all scenarios. This is similar to the case of the macro-variable ψ_1 response. It is worth noting that the response of controller B can be further adjusted by tuning the gains in Eq. (42). This will be investigated thoroughly in section 5.5.2. It is clear that the proposed controller improves the response of i_d significantly especially in the case of adding and removing load torque. Even though the external load torque is not accounted for in the controller design, controller B is

still able to control i_d to follow its reference after adding or removing the load torque. This is not the case in controller A since i_d is not able to converge to 0 because of the added disturbance. i_d maintains a constant steady state error upon adding or removing any load torque. It should also be noted that controller A never converges to 0. There remains a steady state error after each transient. The macro-variables and d-axis current signals have been filtered using a low pass filter with a cutoff frequency at 20 Hz to reduce noise and signal ripples.

5.5.2. Effect of Gains on The SC. In this section, the effect of all gains used in the SC synthesis is studied. The same experiment procedure explained in section 5.5.1 is used to test the performance of the SC. Each gain is tuned with multiple values while keeping the remaining gains constant to see the effect of this inspected gain. This procedure is done for each of the 5 gains ($K_1 - K_5$) used in the controller design in Eq. (42) and (48) as well as the time constants T_d and T_q.

5.5.2.1. Direct Axis Macro-variable ψ_1. The designed macro-variable ψ_1 uses two gains; K_1 and K_2 as shown in Eq. (42). Moreover, with reference to the dynamics of the macro-variable in Eq. (67), it can be realized that the constant T_d also affects the response of the macro-variable. The effect of each gain on the behavior of the macro-variable ψ_1 and the response of the d-axis current i_d will be analyzed. Starting with K_1, Table 3 summarizes the selected gains to test the effect of K_1.

Table 3: Summary of the selected values for K_1 inspection

Experiment	K_1	K_2	T_d
1	0.01	0.3	0.001
2	0.05	0.3	0.001
3	0.1	0.3	0.001
4	0.15	0.3	0.001
5	0.2	0.3	0.001
6	0.25	0.3	0.001

Figure 42 shows the response of the macro-variable ψ_1 upon changing the value of K_1. The same experimental sequence used in section 5.5.1 is used.

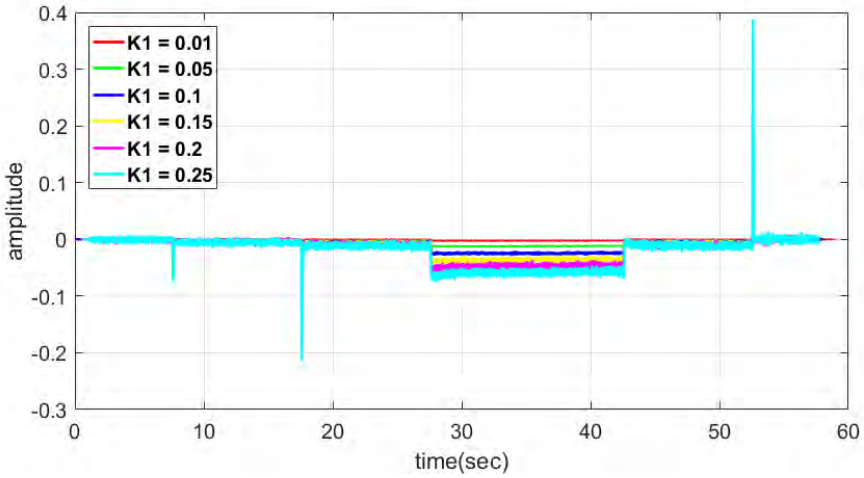

Figure 42: Macro-variable ψ_1 response to different values of K_1

Looking at the transient periods displayed in Figure 43, it is noticed that increasing the value of K_1 increases the magnitude of the peak value that ψ_1 reaches before it starts settling back to its reference. It is also noticed from Figure 43c that the steady state error in case of adding a load torque decreases for lower values of K_1. In the same vein, it is noticed that increasing the value of K_1 increases the ripple of the macro-variable ψ_1.

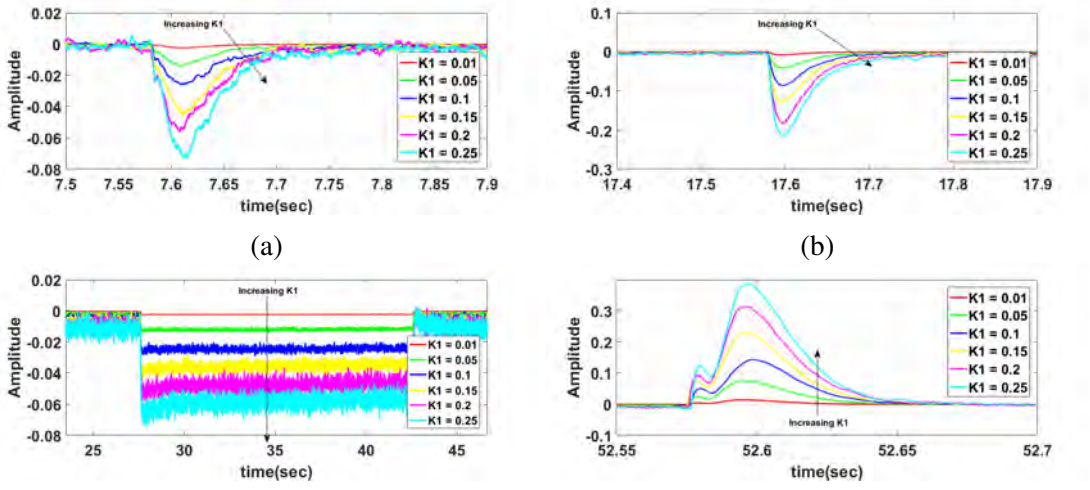

Figure 43: Zoomed views of each transient period of ψ_1 response (a) 1st speed step (b) 2nd speed step (c) Applying and removing load (d) Braking

Figure 44 shows the response of i_d for different values of K_1. It can be realized that i_d always converges to its reference ($i_d^* = 0$) in steady state. During the transient periods, the magnitude of i_d changes for each respective value of the gain K_1. Figure

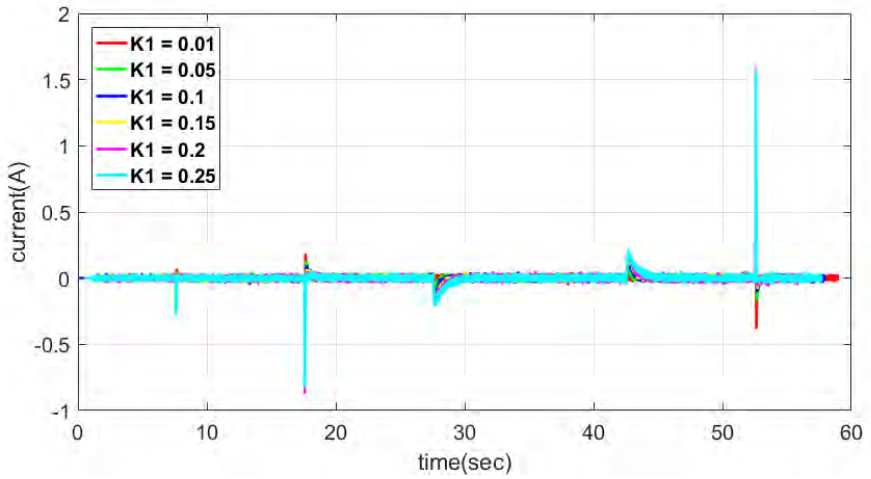

Figure 44: i_d response to different values of K_1

45 shows a closer look at the behavior of i_d during transient periods. It is noticed that, for low values of K_1, the peak of i_d is lower than those recorded for higher values of K_1. However, if K_1 is decreased to a great extent, i_d may exhibit an overshoot in its response, which can be seen in case of $K_1 = 0.01$ represented in red. Therefore, a suitable value of K_1 should be selected to maintain a balance between the response of i_d and ψ_1 altogether.

The above procedure is repeated to study the effect of K_2 on each of ψ_1 and i_d. Table 4 summarizes the selected values of K_2 in this experiment. Figure 46 shows the

Table 4: Summary of the selected values for K_2 inspection

Experiment	K_1	K_2	T_d
1	0.1	0.05	0.001
2	0.1	0.1	0.001
3	0.1	0.15	0.001
4	0.1	0.2	0.001
5	0.1	0.25	0.001
6	0.1	0.3	0.001

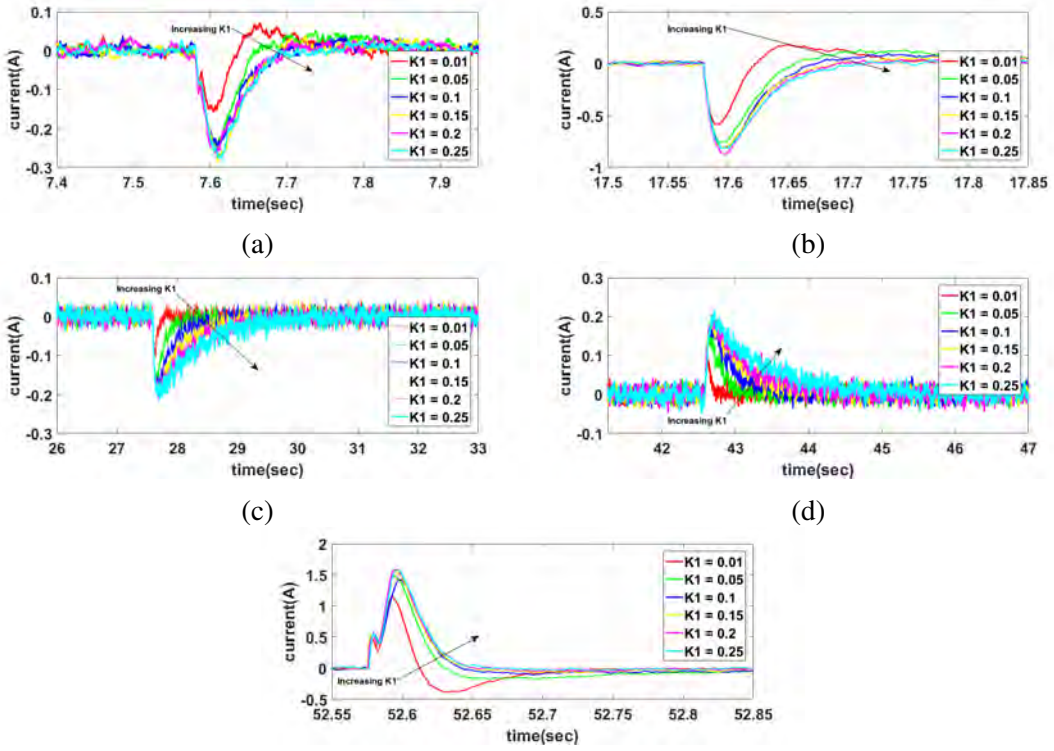

Figure 45: Zoomed views of each transient period of i_d response (a) 1st speed step (b) 2nd speed step (c) Applying load (d) Removing load (e) Braking

response of ψ_1 corresponding to each value of K_2. The results show that ψ_1 converges to 0 in general, with the exception of when adding a load torque. The same experimental sequence used in section 5.5.1 is applied. Figure 47 shows a closer look at each transient period. It can be seen that the gain K_2 does not affect the behavior of ψ_1 significantly. However, this is not the case for i_d. Changing the value of K_2 clearly affects the

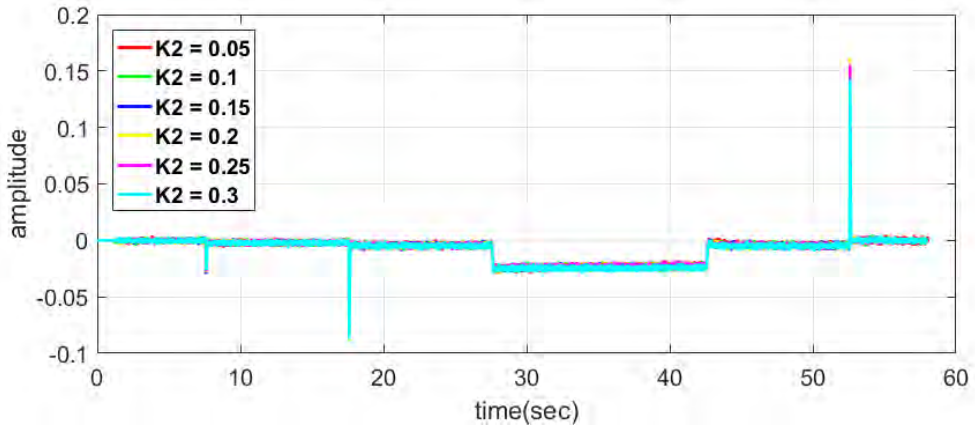

Figure 46: Macro-variable ψ_1 response to different values of K_2

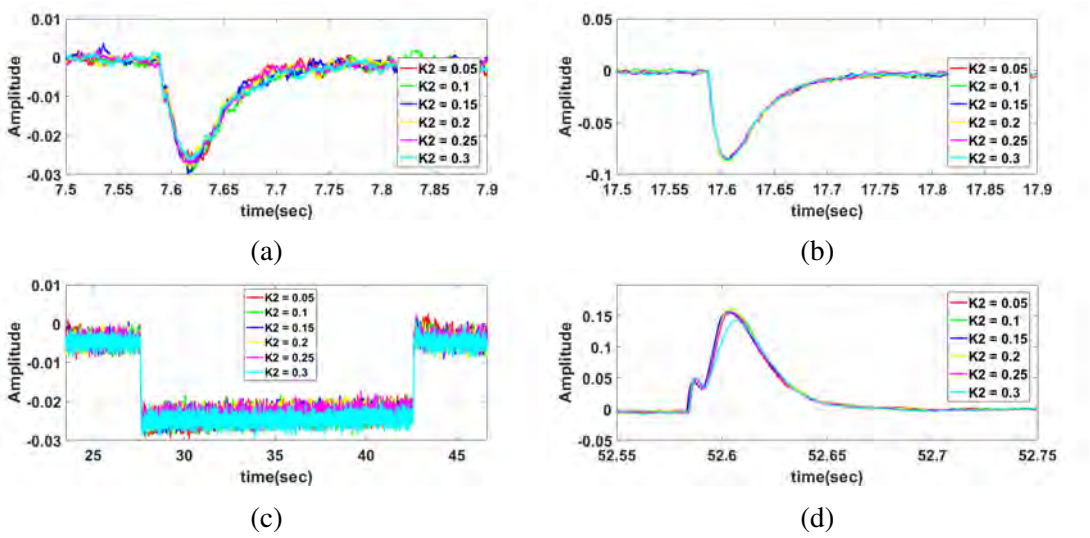

Figure 47: Zoomed views of each transient period of ψ_1 response (a) 1st speed step (b) 2nd speed step (c) Applying and removing load (d) Braking

behavior of i_d as shown in Figure 48. The time of convergence of i_d to its reference ($i_d^* = 0$) is affected by the choice of K_2. Inspecting the transient periods separately, it is noticed that, generally, increasing K_2 returns i_d back to its reference faster. However, this effect is more significant in the case of the presence of any disturbances. This shows that, with proper tuning of K_2, i_d can be maintained at its reference despite any external disturbances to the system. Increasing K_2 to a great extent might add some overshoot to the response of i_d, which is not preferred since i_d is preferably kept at 0 to avoid any demagnetization of the permanent magnets inside the machine. It should be noted that

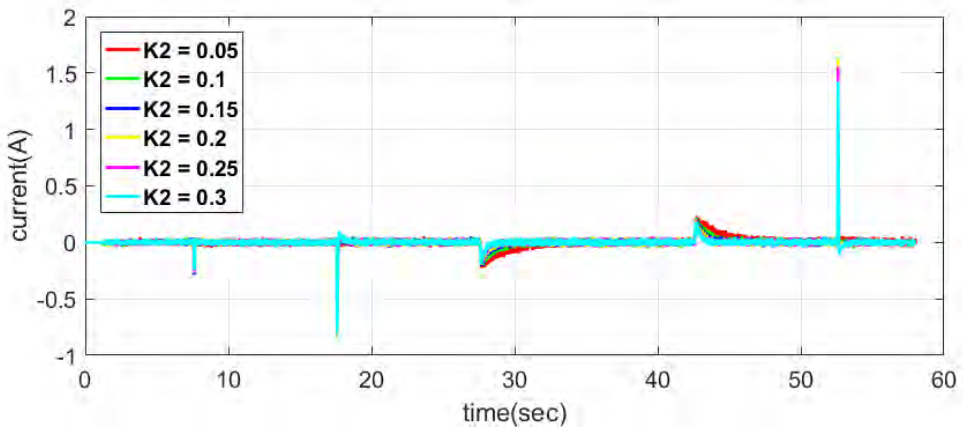

Figure 48: i_d response to different values of K_2

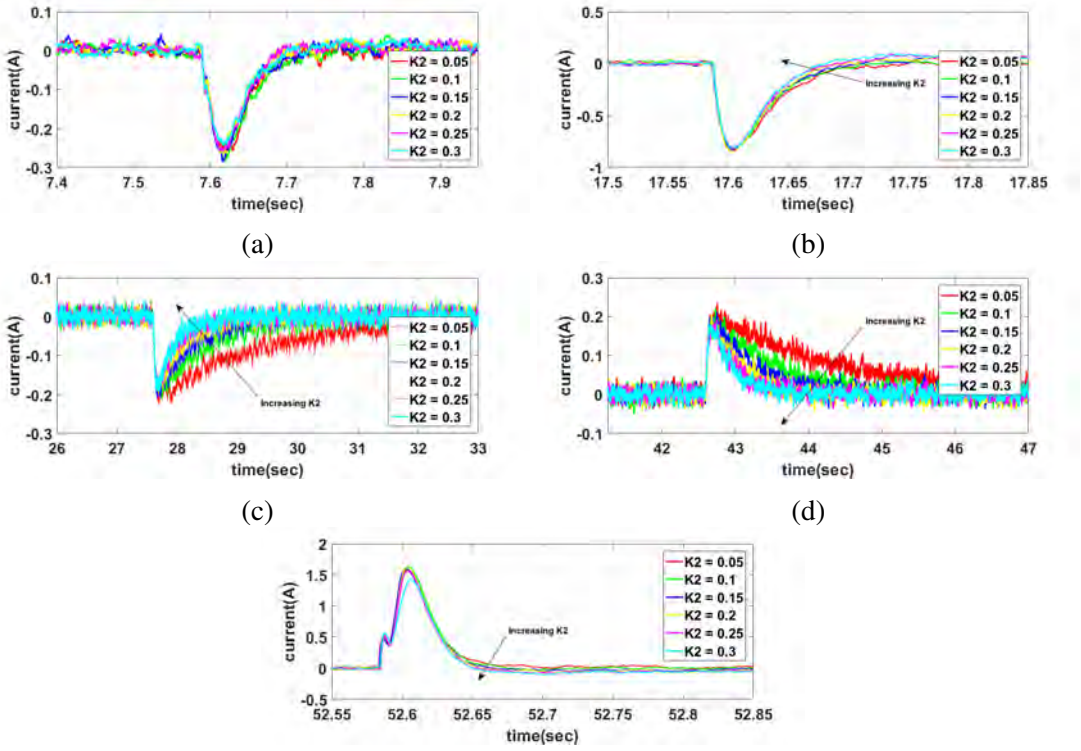

Figure 49: Zoomed views of each transient period of i_d response (a) 1st speed step (b) 2nd speed step (c) Applying load (d) Removing load (e) Braking

all signals for ψ_1 and i_d are filtered by a low pass filter with a cutoff frequency of 20 Hz.

It is also worth mentioning that these gains affect only the behavior of ψ_1 and i_d. The speed of the motor is not affected by changing these gains, since the speed and torque of the motor are controlled only by the second macro-variable ψ_2. Figure 50 shows the response of the motor speed upon changing each of K_1 and K_2. The figure shows that, in both cases, when either K_1 or K_2 is changed, the motor speed is unaffected and all responses align on top of each other. This is expected since ψ_2 was not altered in this experiment.

Lastly, the effect of changing T_d on the behavior of ψ_1 and i_d is studied. Table 5 shows the selected gains in this experiment. T_d is responsible for the time taken by ψ_1 to reach the manifold $\psi = 0$.

Figure 51 shows the response of ψ_1 upon changing the constant T_d. It can be seen that changing T_d affects the magnitude of the peak of ψ_1 reached during the tran-

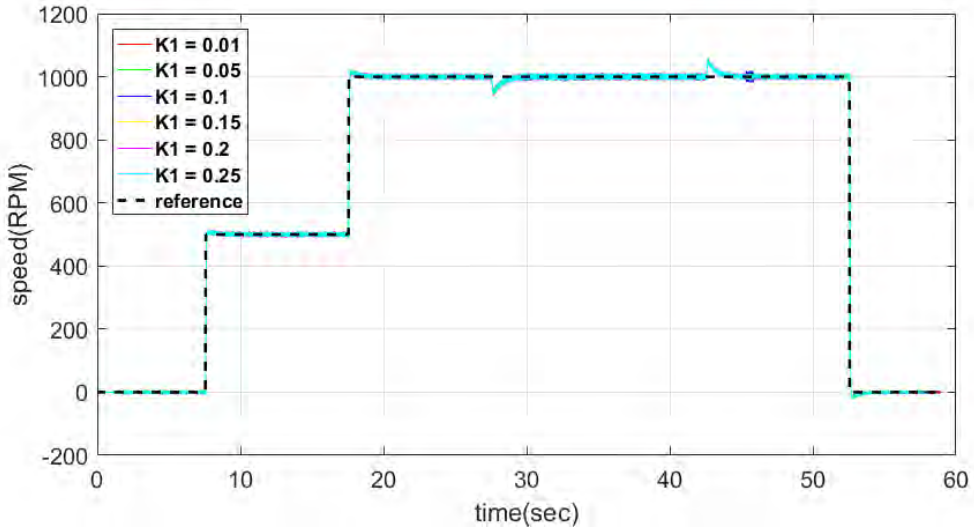

(a)

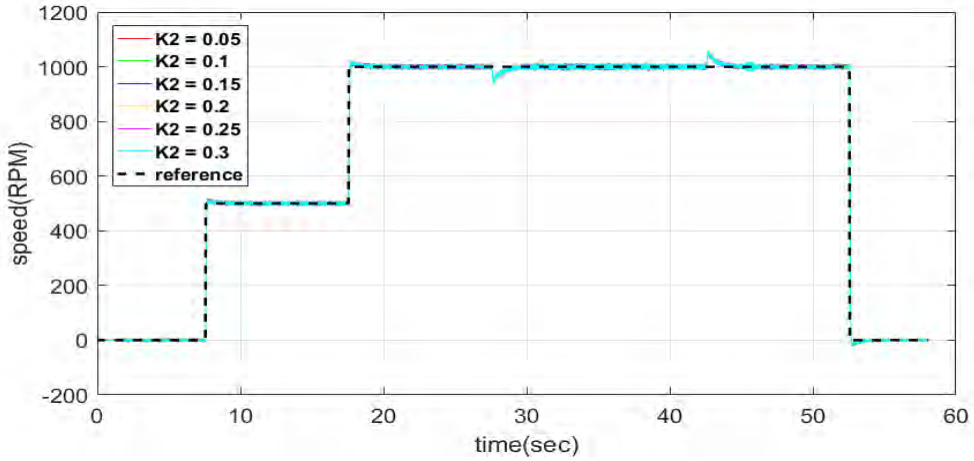

(b)

Figure 50: (a) Motor speed response to different values of (a) K_1 (b) K_2

Table 5: Summary of the selected values for T_d inspection

Experiment	K_1	K_2	T_d
1	0.1	0.3	0.003
2	0.1	0.3	0.001
3	0.1	0.3	0.0007

sient periods, as well as the steady state error. Decreasing T_d indicates that the macro-variable will converge faster to the manifold $\psi = 0$. Upon reaching this manifold, the dynamics of the system depend on the definition of the macro-variable instead of the system dynamics. In other words, reaching the manifold faster will yield a faster response of the system variables. However, this comes at the cost of energy since the

faster response will consume more energy. The transient periods are shown in Figure 52. It is clearly shown that decreasing T_d yields less steady state error and faster transient responses in all scenarios. Similarly, the effect of T_d on the behavior of i_d

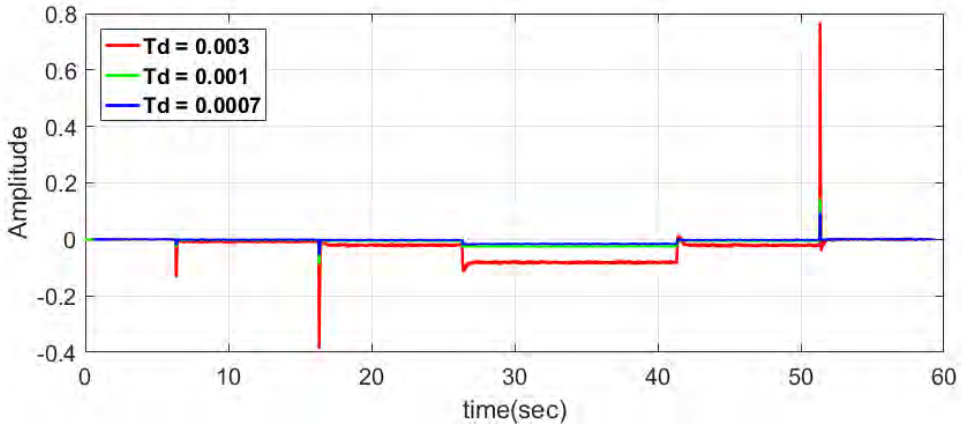

Figure 51: ψ_1 response to changing the constant T_d

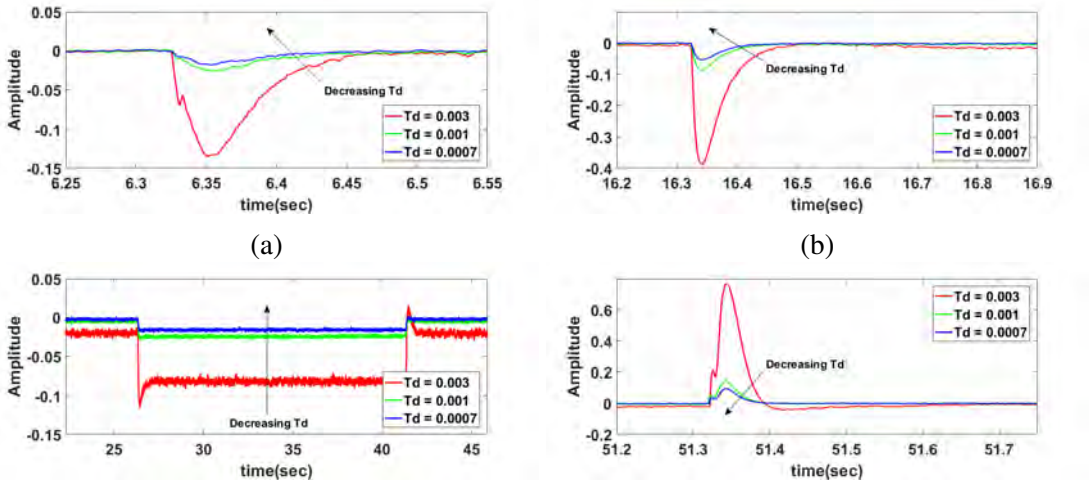

Figure 52: Zoomed views of each transient period of ψ_1 response (a) 1st speed step (b) 2nd speed step (c) Applying and removing load (d) Braking

shows that decreasing T_d will give a faster response of i_d; where i_d is forced to converge back to its reference faster at lower values of T_d. The magnitude of the peaks it reaches during the transient periods also decreases.

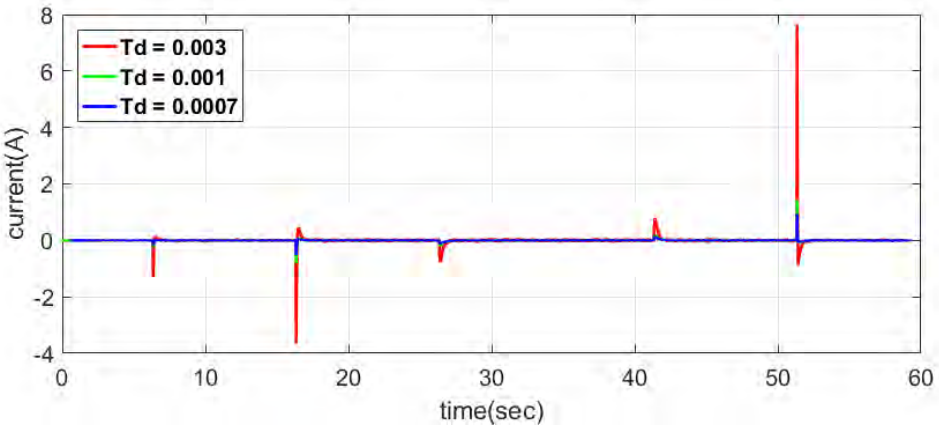

Figure 53: i_d response to different values of T_d

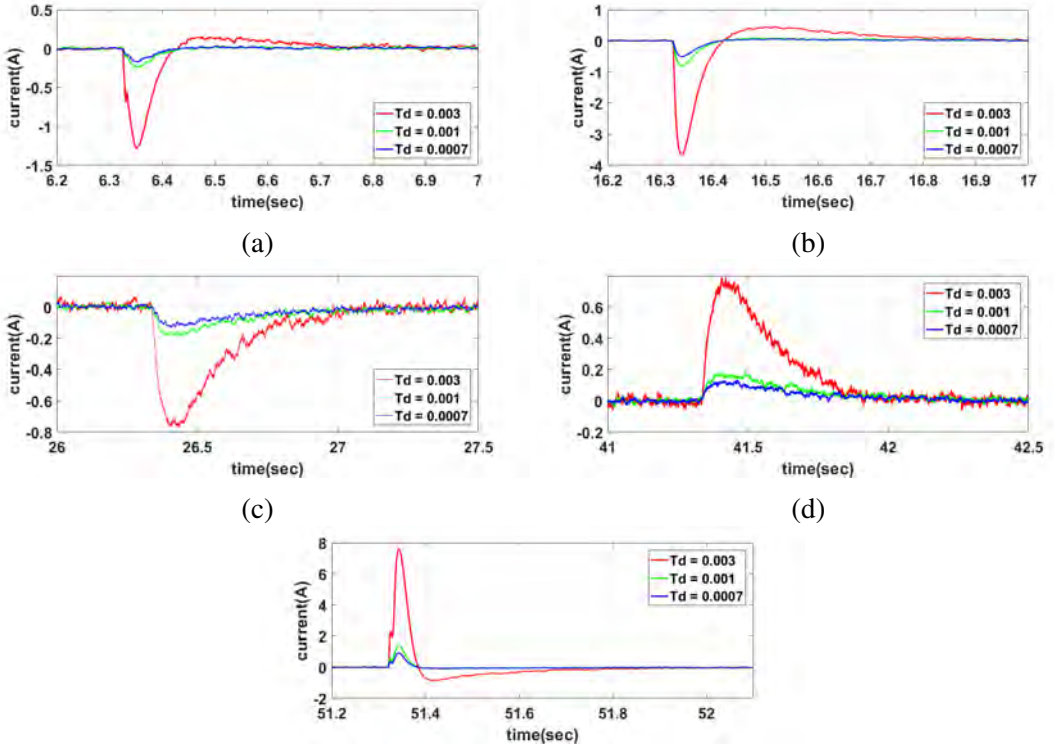

Figure 54: Zoomed views of each transient period of i_d response (a) 1st speed step (b) 2nd speed step (c) Applying load (d) Removing load (e) Braking

Figures 53 and 54 show the response of i_d upon changing the value of T_d. It is noted that for relatively large values of T_d (shown in red), i_d exhibits an overshoot whenever a speed step is invoked. Therefore, proper selection of the constant T_d is crucial for the operation of the system, taking into consideration a good compromise

between the response speed of the system and the consumed energy, which may be limited by hardware limitations and ratings.

This concludes the effect of the gains K_1 and K_2 and the constant T_d on the performance of the macro-variable ψ_1 and i_d. To summarize, K_1 affects the deviation during transient periods as well as the steady state error upon adding a load. K_2 affects the speed of convergence to the reference value while T_d affects the overall speed and error of the system at the cost of energy used, as it allows the macro-variable to converge faster to its manifold.

5.5.2.2. Quadrature Axis Macro-variable ψ_2. Recalling the structure of the q-axis macro-variable ψ_2 given in Eq. (48), ψ_2 is affected by 3 gains, K_3, K_4 and K_5. In addition, the constant T_q affects the time of convergence of ψ_2 as per the macro-variable's dynamics given by Eq. (35). To investigate the effect of the mentioned gains, each gain value is changed while maintaining the remaining gains unaltered. The same experimental sequence used in section 5.5.1 is followed. The effect of these gains on the motor speed, generated command i_q^* and the macro-variable ψ_2 is demonstrated. It is worth noting that ψ_2 results have been filtered using a low pass filter with cutoff frequency of 20 Hz to reduce acquisition ripples and noise. The first and last elements of Eq. 48 control the speed of the motor, and they are directly affected by the gains K_3 and K_5. Together, these two terms generate the reference i_q^* which adjusts the machine torque as desired through controlling i_q. Table 6 summarizes the selected values of K_3 in this experiment. Figure 55 shows the response of ψ_2 corresponding to each value of K_3.

Table 6: Summary of the selected values for K_3 inspection

Experiment	K_3	K_4	K_5	T_q
1	0.01	1	0.15	0.001
2	0.05	1	0.15	0.001
3	0.1	1	0.15	0.001
4	0.15	1	0.15	0.001
5	0.2	1	0.15	0.001

The figure shows that ψ_2 exhibits different peak values in transient periods. The peak increases with higher values of K_3. In steady state, the macro-variable always settles

back to 0 as desired except for cases of adding a load, where there remains a steady state error because this load acts as a disturbance and was not accounted for in the design of the macro-variable. Figure 56 shows a zoomed in capture of all transient periods. It is

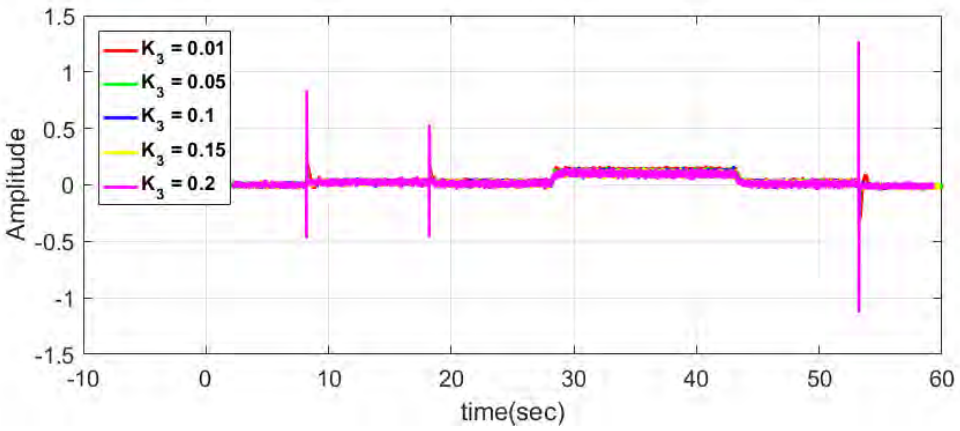

Figure 55: Response of ψ_2 upon changing K_3

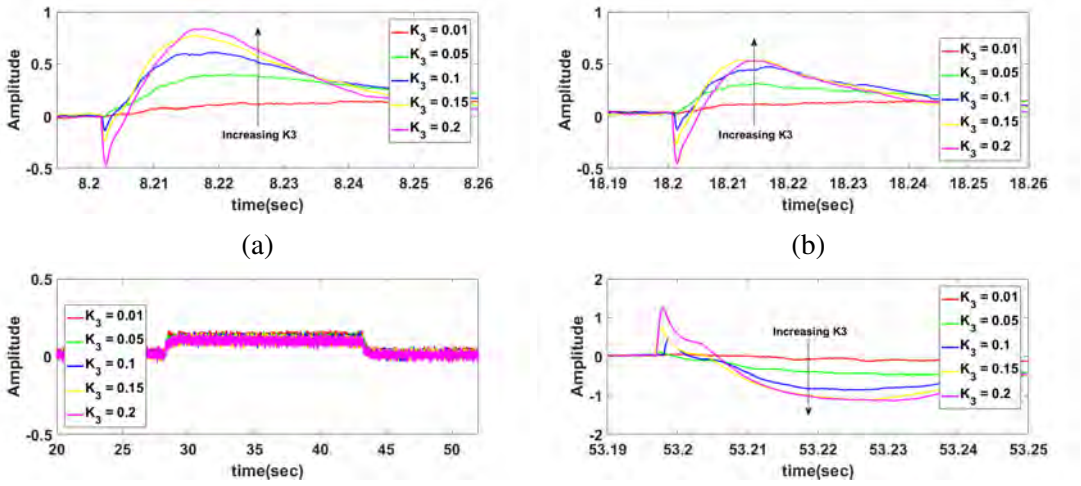

Figure 56: Zoomed views of each transient period of ψ_2 response (a) 1st speed step (b) 2nd speed step (c) Applying and removing load (d) Braking

observed that the amplitude of ψ_2 increases when K_3 is increased. In case of adding a load, the macro-variable exhibits a steady state error for the reasons explained earlier. This error is the same regardless of the value of K_3, as shown in Figure 56c.

Figure 57 presents the motor speed response corresponding to each value of K_3 used. It shows that the motor speed overshoot and peak magnitudes differ depending on the value of K_3. Figure 58 shows the zoomed in captures of the transient periods for closer inspection. The figure indicates that extremely low values of K_3 (in red for

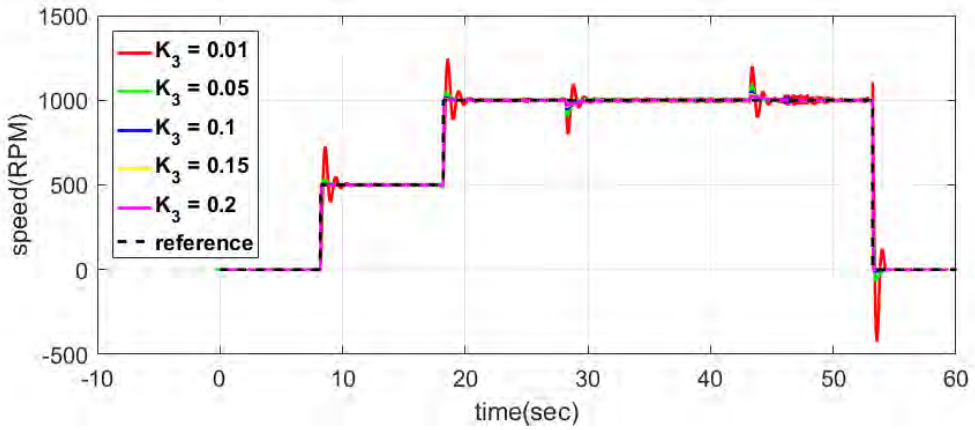

Figure 57: Motor speed response upon changing K_3

example) exhibit an underdamped response with very high overshoot and slow settling times. Increasing K_3 decreases the oscillations and maintains and overdamps response. In cases of adding or removing load torque, increasing K_3 reduces the error of the motor speed before it starts settling back to its reference once again. The impact of removing or adding the load is lessened by increasing K_3. The command i_q^* generated by the controller in each case of K_3 is displayed in Figure 59. The controller generates a higher command current as K_3 is increased. Figure 60 shows the generated i_q^* in each transient period. It is noticed that increasing K_3 increases the ripples of the generated command current. Increasing K_3 could result in high command currents as shown in the case of $K_3 = 0.2$ (shown in magenta) where the reference current reaches $10A$ and $-20A$. Tuning this gain should be done with caution to not generate high current ratings that might damage the machine.

As mentioned, K_3 and K_5 affect the speed directly. Therefore, the effect of K_5 is studied and displayed first. Table 7 shows the selected values for K_5's inspection. K_5 tunes the effect of the integral of the error in motor speed from its reference. Figure 61 shows the response of ψ_2 for different values of K_5. The figure shows that the

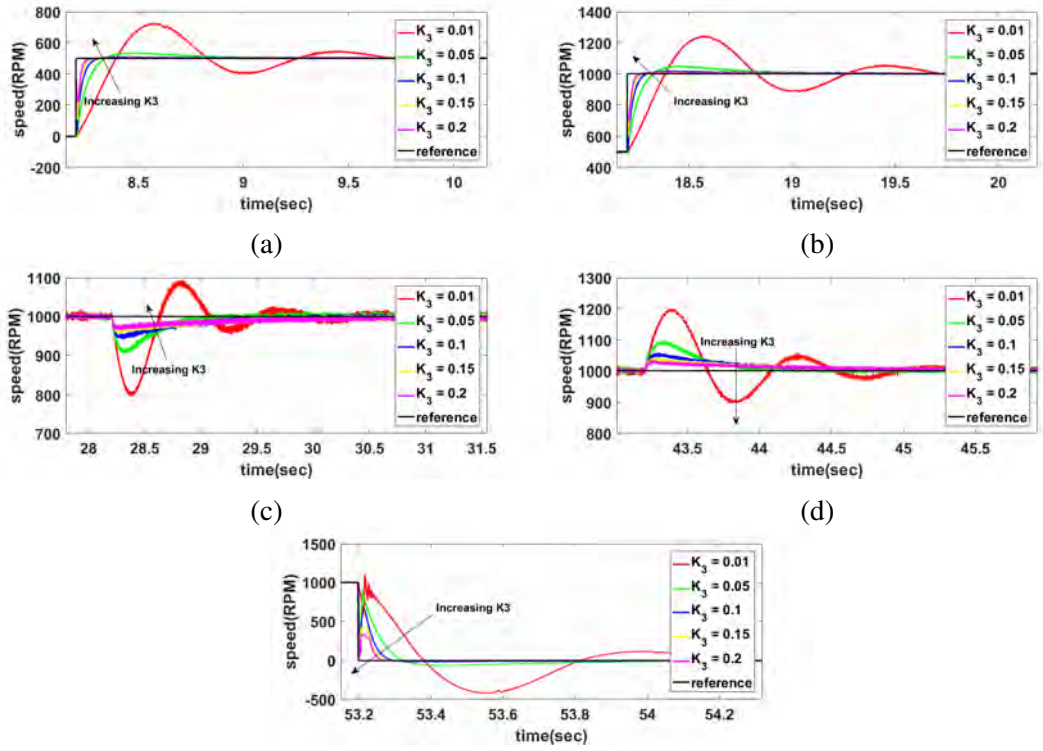

Figure 58: Zoomed views of each transient period of motor speed response (a) 1st speed step (b) 2nd speed step (c) Applying load (d) Removing load (e) Braking

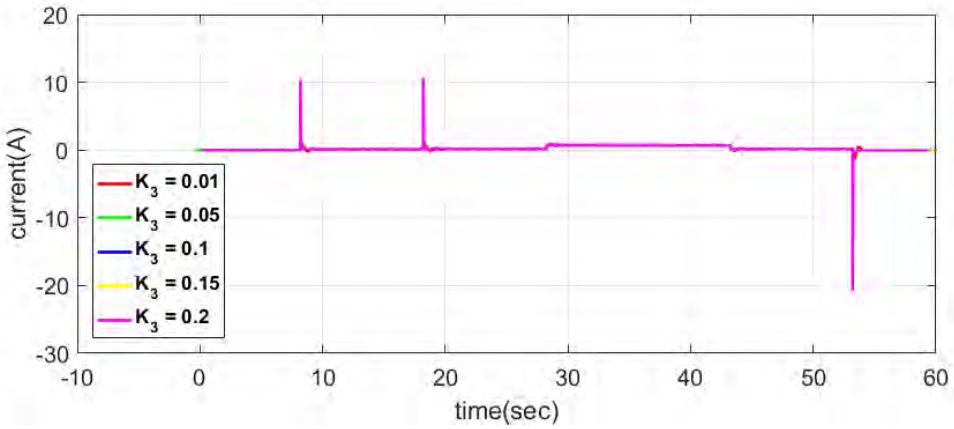

Figure 59: Generated i_q^* upon changing K_3

macro-variable converges to 0 in steady state except when load is added to the system. Transient responses, presented in Figure 62, show that K_5 does not affect the response of ψ_2 significantly. Increasing K_5 will increase the amplitude of ψ_2 by negligible amounts. This, in fact, is the case for ψ_1 as well when the effect of K_2 was studied in section 5.5.2.1. This concludes that integral terms have less effects on the behavior of the

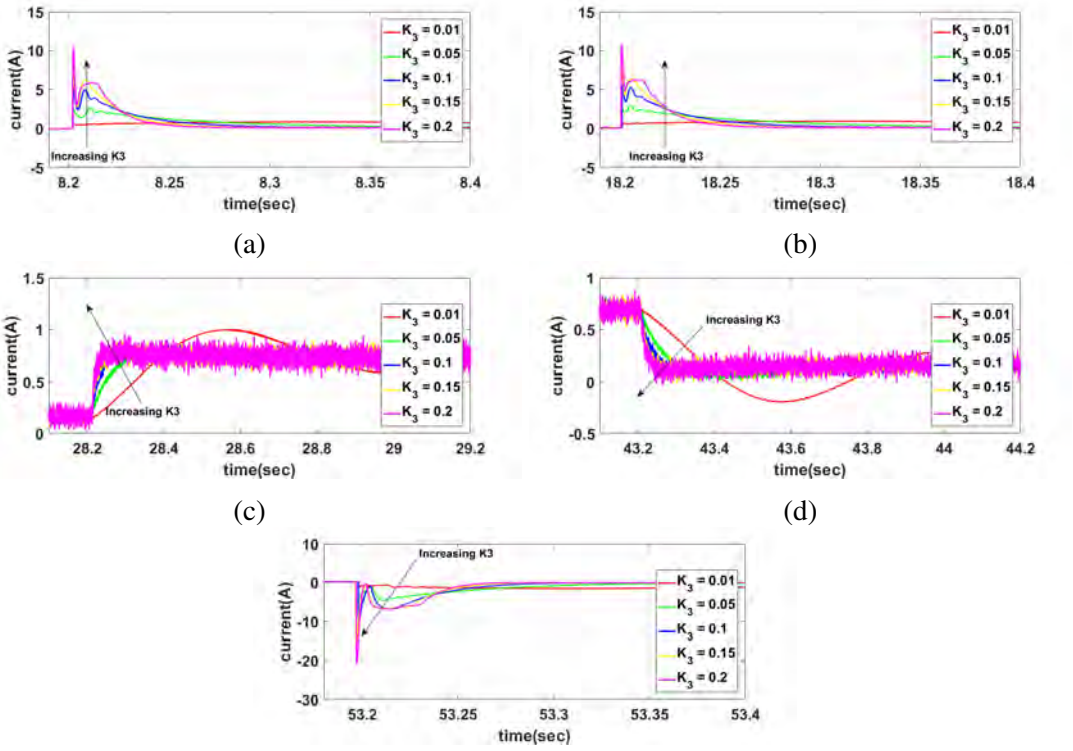

Figure 60: Zoomed views of each transient period of i_q^* response (a) 1st speed step (b) 2nd speed step (c) Applying load (d) Removing load (e) Braking

Table 7: Summary of the selected values for K_5 inspection

Experiment	K_3	K_4	K_5	T_q
1	0.1	1	0.01	0.001
2	0.1	1	0.05	0.001
3	0.1	1	0.1	0.001
4	0.1	1	0.15	0.001
5	0.1	1	0.2	0.001

macro-variable itself. Nonetheless, they are added to adjust key variables that construct the macro-variable such as speed and i_d in cases of ψ_2 and ψ_1, respectively.

With regards to the effect of K_5 on the motor speed, the response of the motor speed corresponding to different values of K_5 is shown in Figure 63. The figure indicates that the motor speed converges faster to its reference at higher values of K_5. This effect is noticed the most when the load torque is added or removed from the system. Since the load acts as a disturbance, the effect of K_5 stands out as it shows how fast the system is able to correct itself whenever disturbance is applied. Inspecting the transient periods

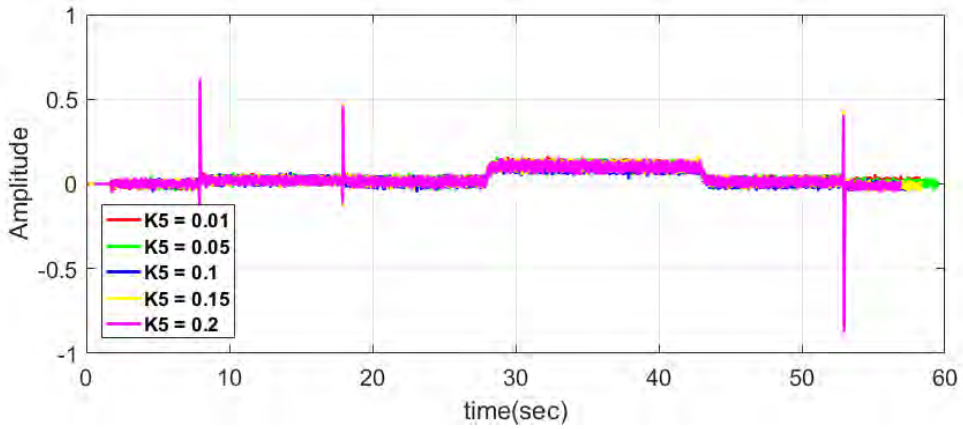

Figure 61: ψ_2 response upon changing K_5

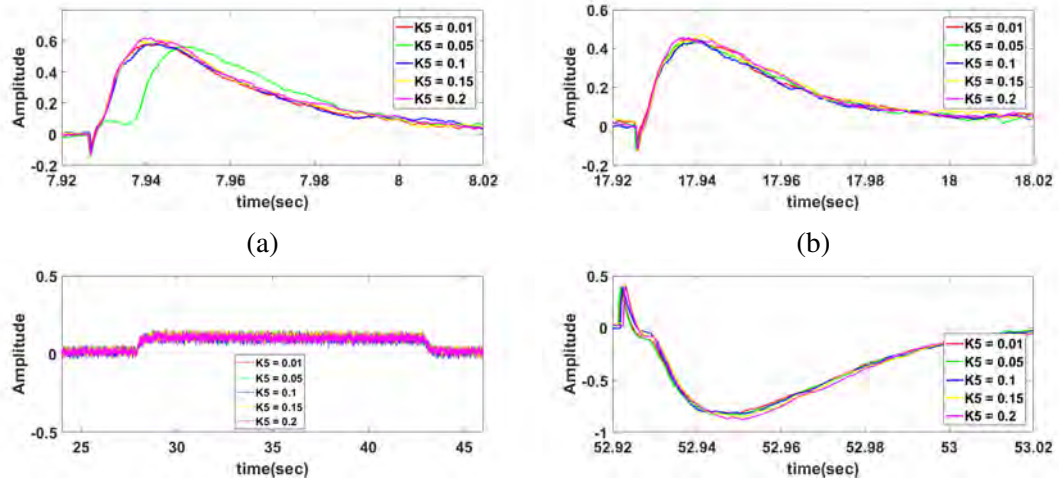

Figure 62: Zoomed views of each transient period of ψ_2 response (a) 1st speed step (b) 2nd speed step (c) Applying and removing load (d) Braking

shown in Figure 64, it is noticed that increasing K_5 increases the speed of convergence and eliminates steady state error faster. Comparing the response of the highest and lowest gain values, represented in magenta and red respectively in Figures 64c and 64d, it is noticed that the effect of K_5 is significant. As for changing the speed reference, increasing K_5 will slightly decrease the settling time. The fluctuations in speed in the transient response are not caused by the controller. After some inspection and testing, it is noticed that these fluctuations occur at high step inputs and fast responses. It is suspected that this may be caused by the coupling between the motor's shaft and the encoder. This behavior occurs regardless of the controller used.

The effect of K_5 on the generated i_q^* is also studied. Figure 65 shows the generated i_q^* for different values of K_5.

Next, the effect of K_4 on the behavior of ψ_2, the motor speed and i_q^* is studied. In general, decreasing K_4 less than 1 increases the generated i_q^* significantly. Therefore, the speed step reference was halved in this experiment to avoid drawing high values of current. Table 8 shows the selected values of K_4 in this experiment.

Table 8: Summary of the selected values for K_5 inspection

Experiment	K_3	K_4	K_5	T_q
1	0.1	0.25	0.15	0.001
2	0.1	0.5	0.15	0.001
3	0.1	1	0.15	0.001
4	0.1	1.5	0.15	0.001
5	0.1	2	0.15	0.001

The design of the macro-variable ψ_2 requires keeping K_2 equal to 1. Simply because the first and third terms in Eq. (48) will generate the command $-i_q^*$ that adjusts the motor torque as required, depending on the error in the motor speed. Keeping K_4 equal to 1 results in the difference $i_q - i_q^*$ forcing it to converge to 0 as ψ_2 converges to 0. Figure 67 illustrates the response of ψ_2 upon changing the value of K_4. It shows that, in steady state, the macro-variable ψ_2 converges to 0. However, when a load torque is added to the system, the steady state error increases as K_4 increases. Analysis of the

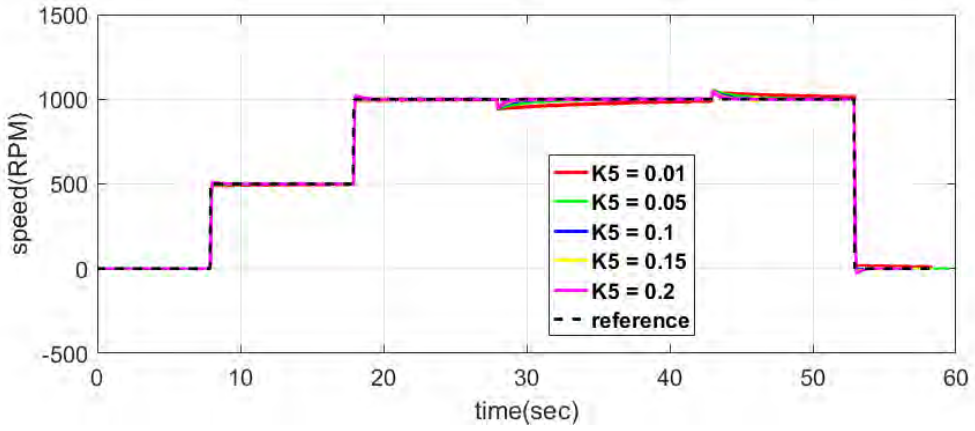

Figure 63: Motor speed response upon changing K_5

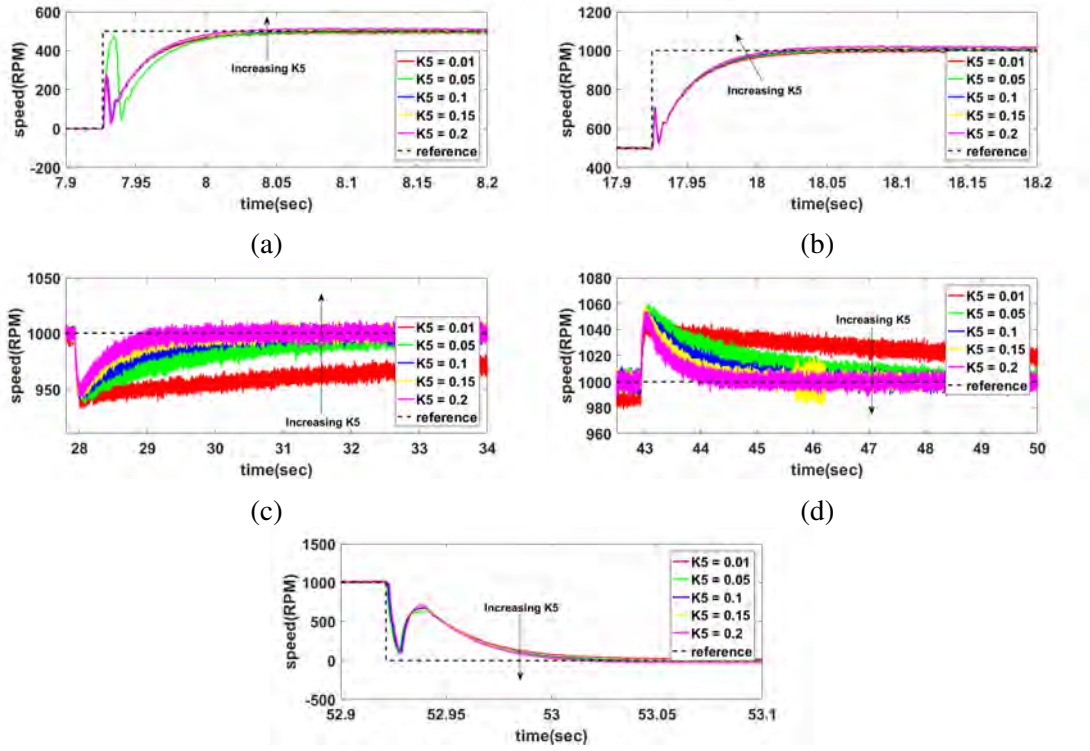

Figure 64: Zoomed views of each transient period of motor speed response (a) 1st speed step (b) 2nd speed step (c) Applying load (d) Removing load (e) Braking

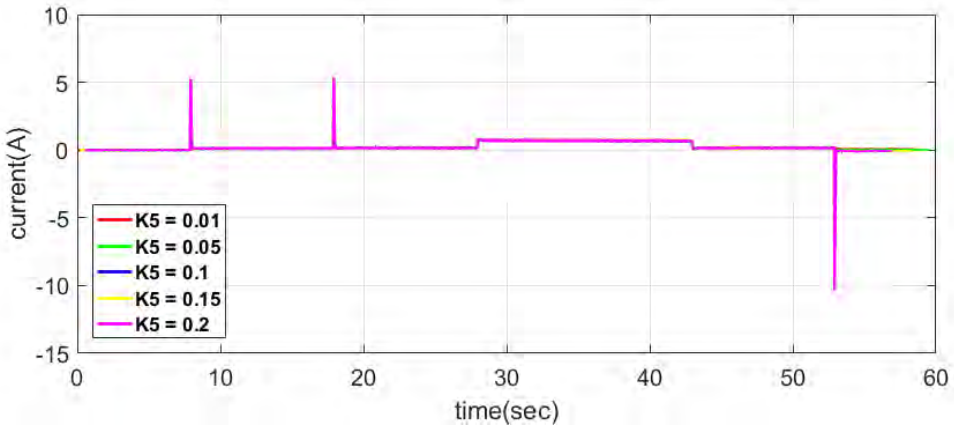

Figure 65: Generated i_q^* upon changing K_5

transient periods shown in Figure 68 shows that the peak of ψ_2 in every period increases with the increase of K_4. The settling time also increases.

Studying the effect of K_4 on the motor speed, Figure 69 shows the response of the motor speed to different values of K_4. The figure shows higher settling times and higher speed peaks in transients as K_4 increases. On the other hand, the motor

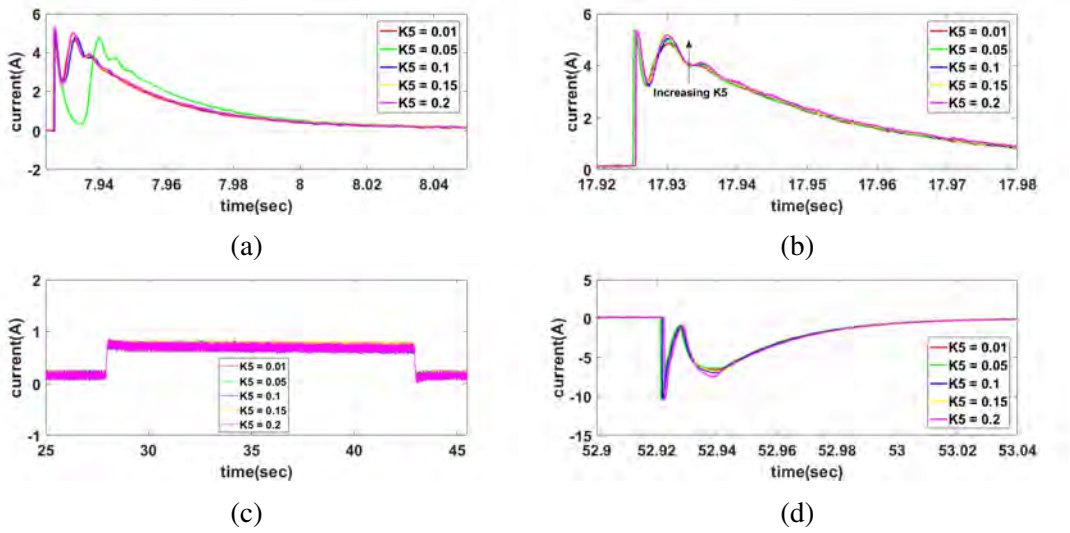

Figure 66: Zoomed views of each transient period of i_q^* response (a) 1st speed step (b) 2nd speed step (c) Applying and removing load (d) Braking

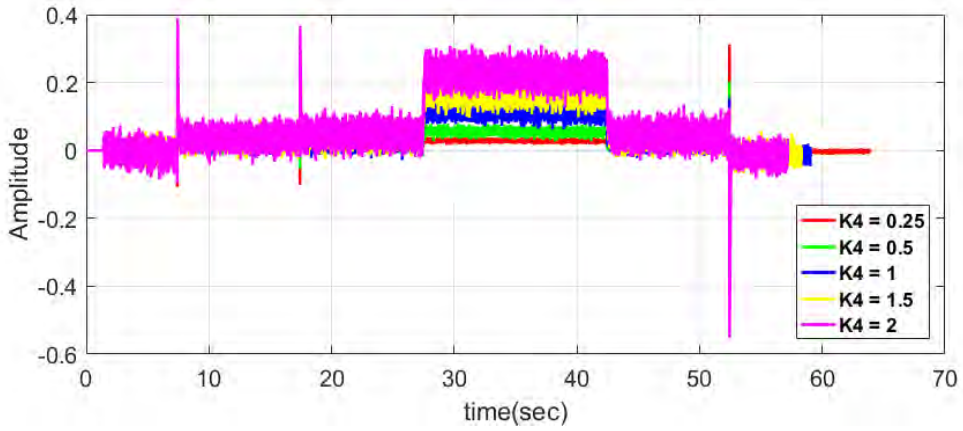

Figure 67: ψ_2 response upon changing K_4

speed settles back to its reference in steady state as desired. Transient periods shown in Figure 70 show that the speed is less effected by the disturbance load as K_4 decreases. Significant enhancement to settling times of the motor speed is also noticedl. Figure 71 shows the generated i_q^* for different values of K_4. Figure 72 shows the transient periods. It shows that as K_4 decreases, the generated i_q^* decreases. This leads to less settling time and less steady state error in transient periods and on the addition of any load torque. The reason for this, is that decreasing K_4 in Eq. 48 to be less than 1, the generated i_q^* is compared to a portion of the actual i_q of the system. Hence, this error converges faster. Upon increasing the value of K_4 beyond 1, the generated i_q^* is compared to multiples

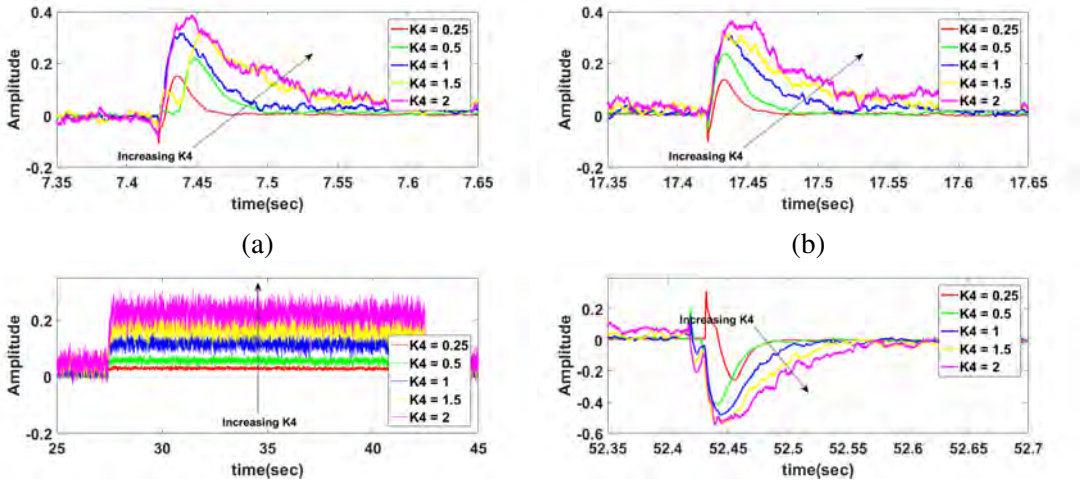

Figure 68: Zoomed views of each transient period of ψ_2 response (a) 1st speed step (b) 2nd speed step (c) Applying and removing load (d) Braking

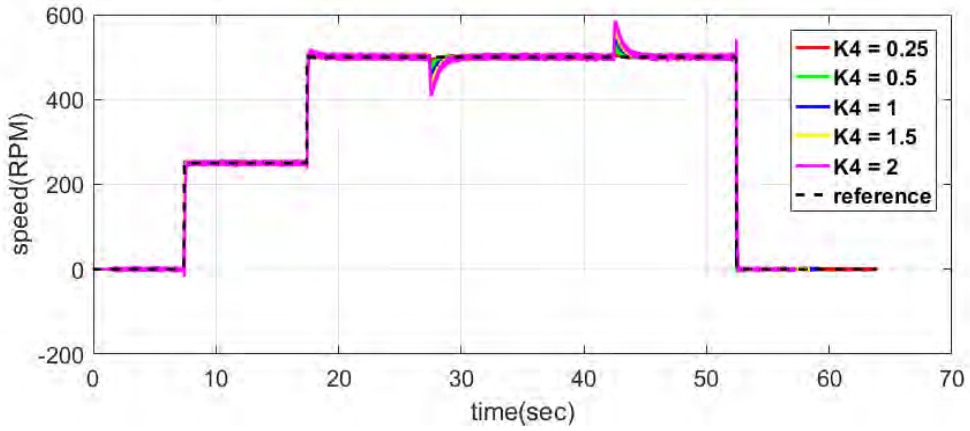

Figure 69: Motor speed response upon changing K_4

of the actual value of i_q which adds some delay and more error in the response of the macro-variable. In other words, when K_4 is decreased, the controller accounts for portion of the actual i_q only. Therefore, low values of i_q^* are generated, thinking that this is the actual value of i_q. This however means that the actual error between i_q and i_q^* converges slowly and hence, high values of i_q are drawn by the motor. This results in higher electromagnetic torque. For that reason, the motor speed converges the fastest at the lowest value of K_4. On the other hand, when K_4 is greater than 1, the controller senses multiples of the actual i_q. Thinking that the error is greater than it actually is. Hence, it generates higher values of the command current i_q^* to overcome this extra

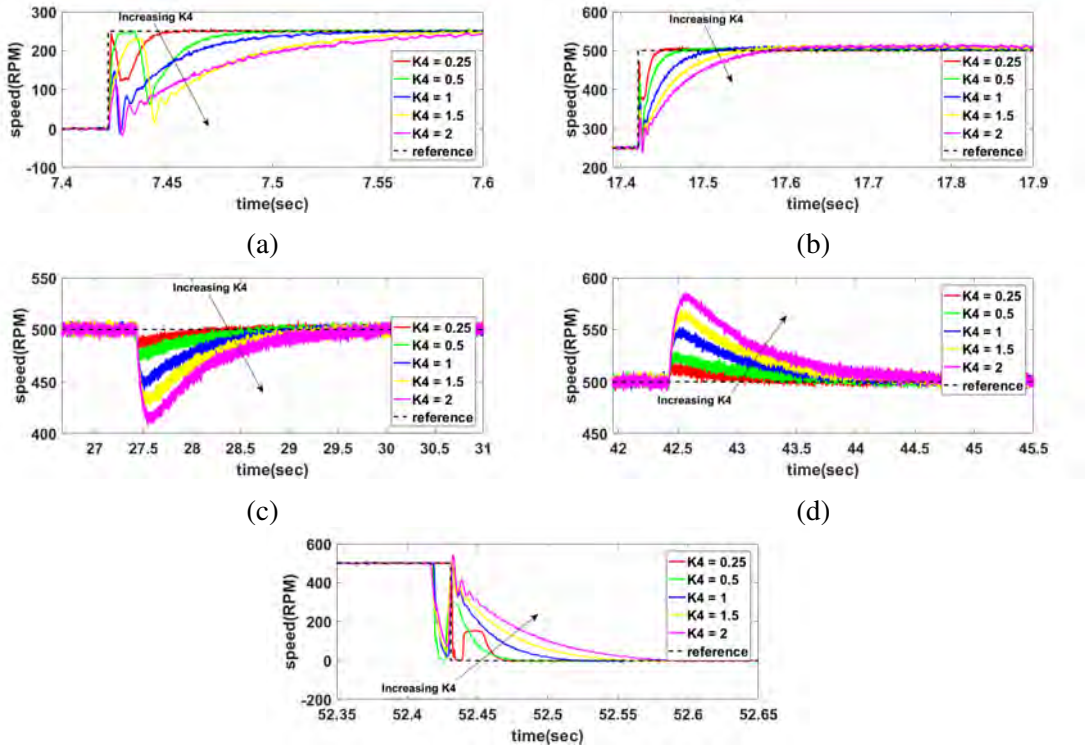

Figure 70: Zoomed views of each transient period of the motor speed response (a) 1st speed step (b) 2nd speed step (c) Applying load (d) Removing load (e) Braking

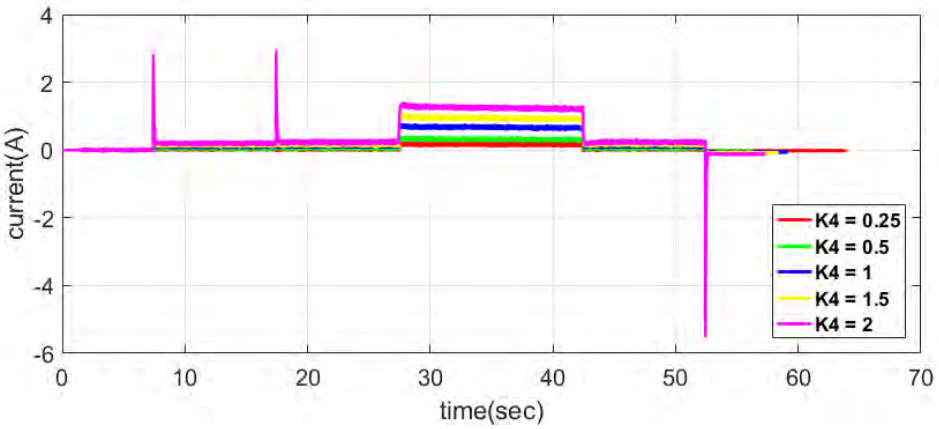

Figure 71: Generated i_q^* upon changing K_4

error. This leads to less current being actually absorbed by the motor since it reaches its speed reference without the need for excess energy. Therefore, the speed of the motor converges slowly, because the motor draws less current. To confirm this, the actual q-axis current i_q drawn by the motor in this experiment is displayed in Figure 73. As shown in the figure, the lower values of K_4 consume much higher currents and vice

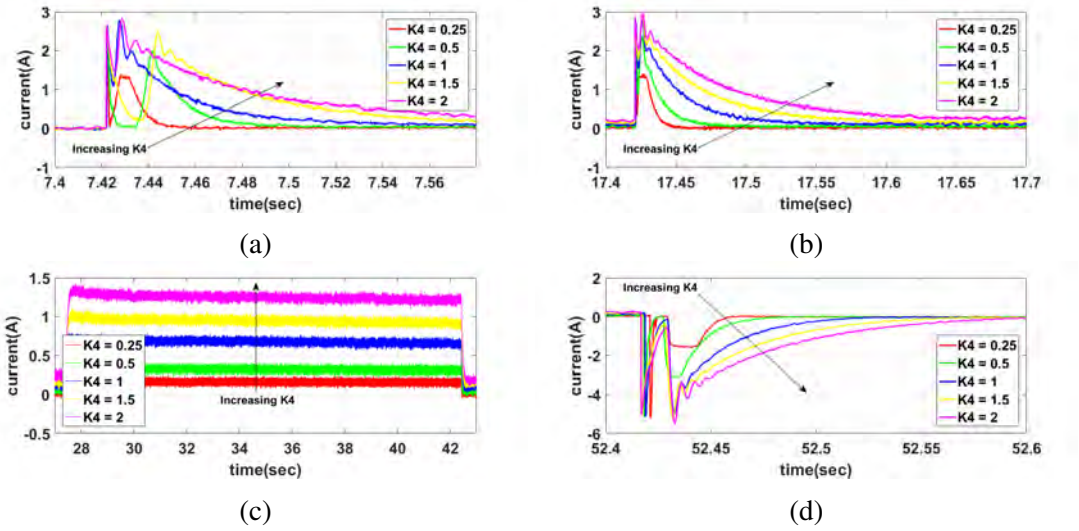

Figure 72: Zoomed views of each transient period of the generated i_q^* (a) 1st speed step (b) 2nd speed step (c) Applying and removing load (d) Braking

versa. This speed step was halved compared to any of the other experiments because the system drew higher currents. The figure shows that the lowest value of K_4 consumes almost $10A$ when the speed step was 250 RPM only.

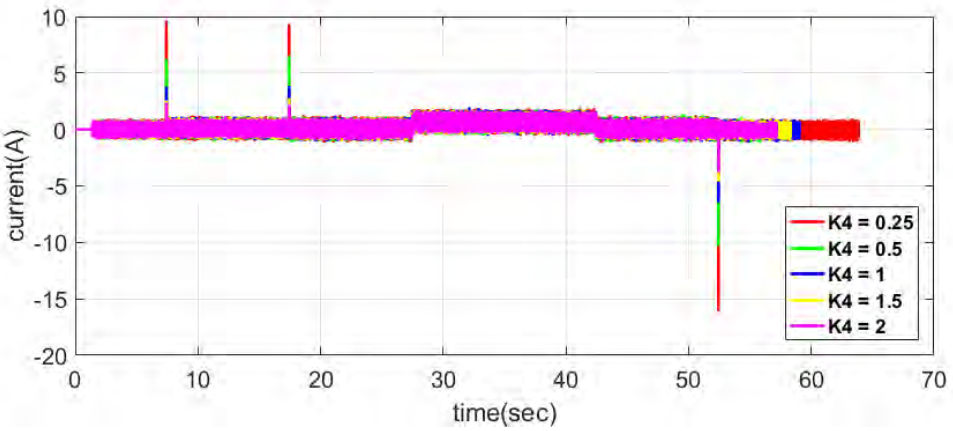

Figure 73: Actual i_q consumed upon changing K_4

Finally, the value of the constant T_q in Eq. 35 is changed to investigate its effect. Table 9 shows the selected values of this constant in this experiment. This constant affects the convergence speed of ψ_2 to 0. Faster convergence speeds will consume more energy. Figures 74 and 75 show the response of ψ_2 for different values of T_q. Upon decreasing the value of T_q, ψ_2 converges faster to 0 and shows less steady state

Table 9: Summary of the selected values for T_q inspection

Experiment	K_3	K_4	K_5	T_q
1	0.1	1	0.15	0.003
2	0.1	1	0.15	0.001
3	0.1	1	0.15	0.0007

error when load torque is applied. This in fact will be at the cost of using more energy which will be shown in the i_q^* plots.

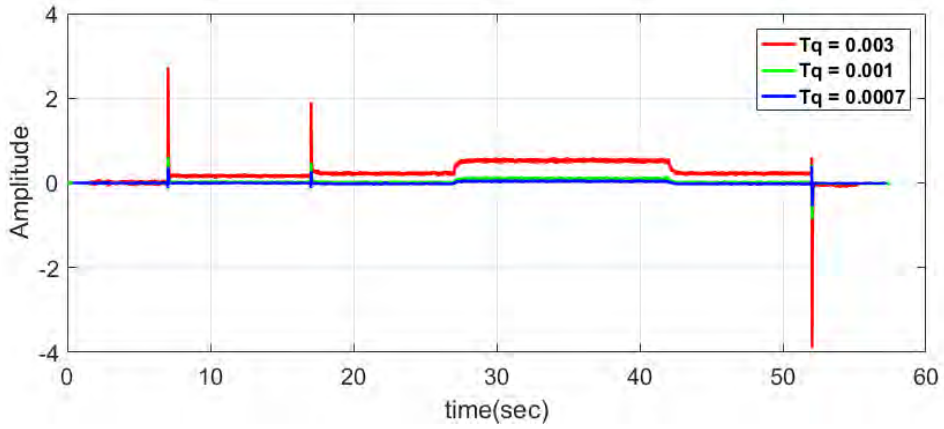

Figure 74: ψ_2 response to changing the constant T_q

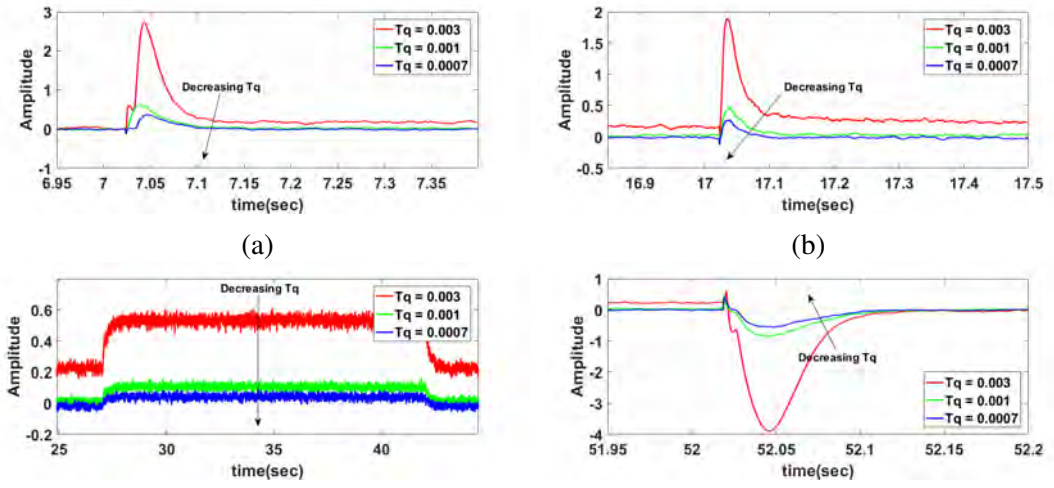

Figure 75: Zoomed views of each transient period of ψ_2 response (a) 1st speed step (b) 2nd speed step (c) Applying and removing load (d) Braking

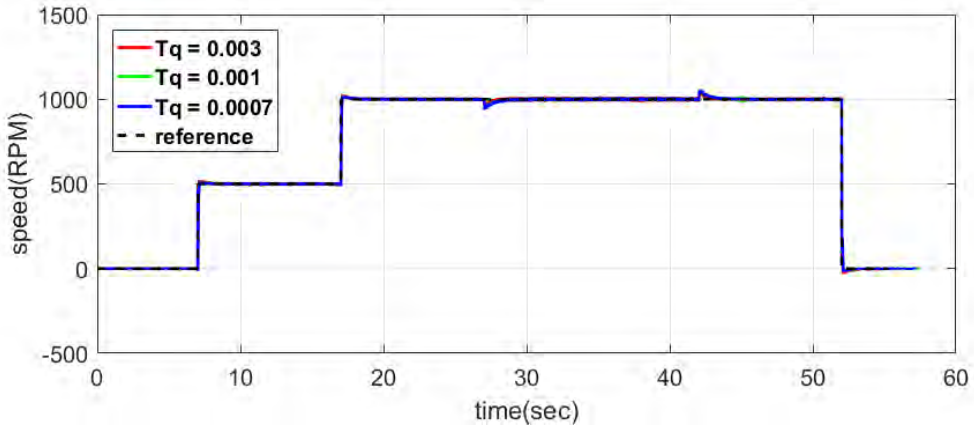

Figure 76: Motor speed response upon changing T_q

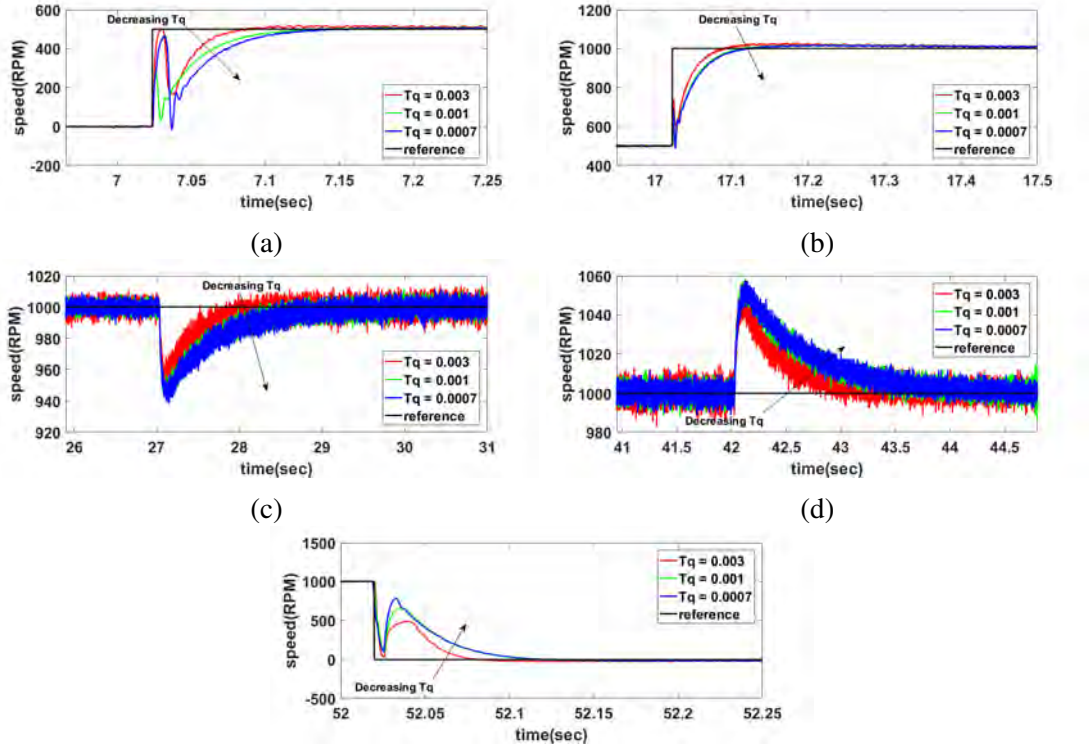

Figure 77: Zoomed views of each transient period of the motor speed response (a) 1st speed step (b) 2nd speed step (c) Applying load (d) Removing load (e) Braking

Faster convergence of ψ_2 means faster convergence of the motor speed. Figures 76 and 77 show the response of the motor speed for different values of T_q. As expected, the motor speeds settles faster at lower values of T_q. The motor speed in case of $T_q = 0.003$ (shown in red) exhibits a slight overshoot before it converges to its reference, while the other two cases converge faster without any overshoot. However, in the case

of adding some disturbance, the speed is less affected when T_q is higher as shown in Figures 77c and 77d. With regards to the generated i_q^*, the faster convergence requires more energy and this higher generated i_q^* values. This can be seen in Figures 78 and 79. The convergence time constant T_q should be carefully selected to not draw a great deal of energy or select a very slow response. A good compromise must be found between both options.

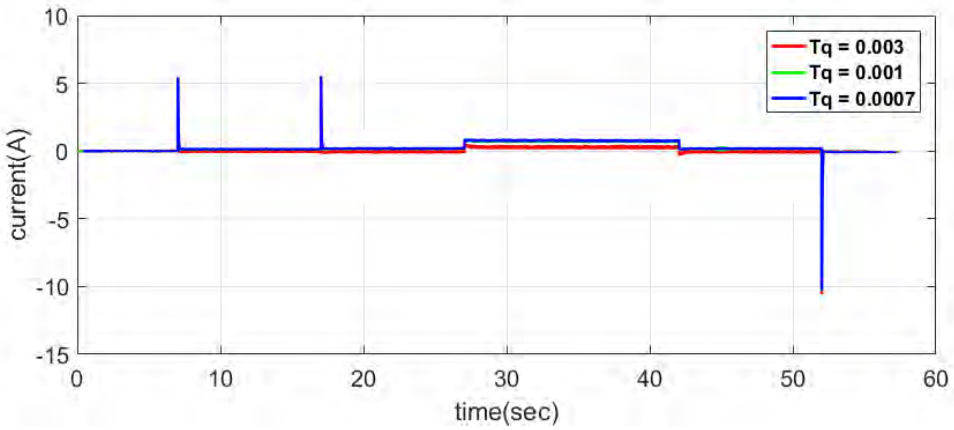

Figure 78: Generated i_q^* upon changing T_q

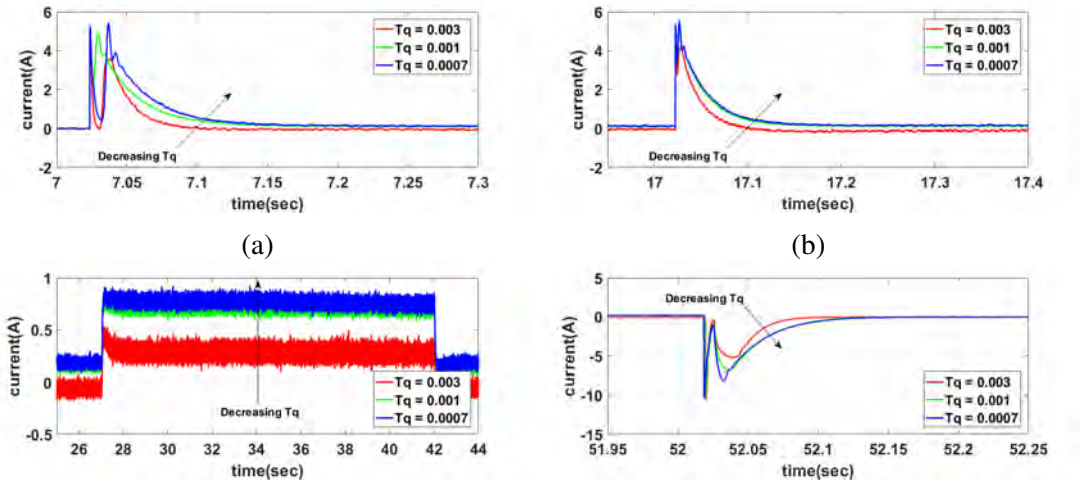

Figure 79: Zoomed views of each transient period of the generated i_q^* (a) 1st speed step (b) 2nd speed step (c) Applying and removing load (d) Braking

5.5.3. Comparing Field Oriented Control and Synergetic Control. In this section, the performance of the synergetic controller is compared to that of the field oriented controller. The FOC is used as a benchmark to test the synergetic controller's performance. Both controllers are tuned so that they have approximately similar settling time of about 0.05s. Table 10 shows the selected values of controllers' gains. The controllers are subjected to the same experimental sequence. Figure 80 shows the speed response of both controllers.

Table 10: Selected controller gains

FOC			SC					
Speed Controller	K_p	0.2	ψ_1	K_1	0.1	ψ_2	K_3	0.1
	K_i	0.6		K_2	0.3		K_4	1
Current Controllers	K_p	0.3		T_d	0.001		K_5	0.15
	K_i	0.9					T_q	0.001

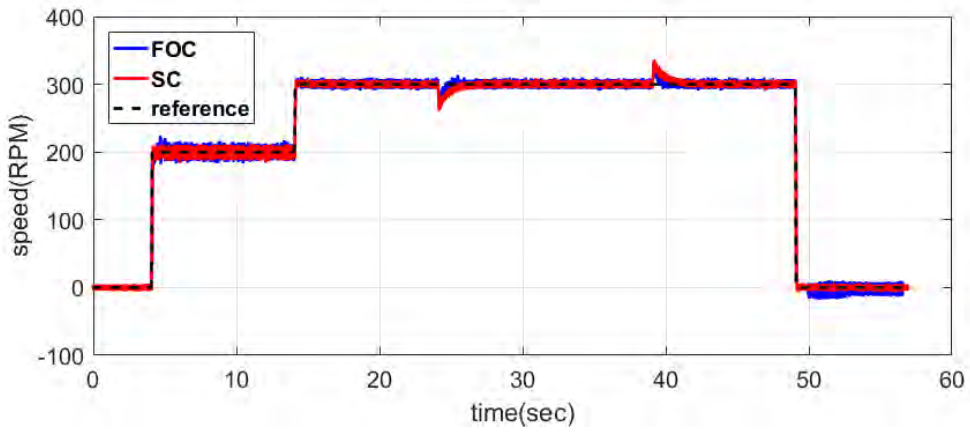

Figure 80: Speed response of FOC and SC

It indicates that both controllers track the speed reference as desired without any steady state errors. Both controllers are able to correct the speed after adding or removing the load. Zooming in on the transient periods shown in Figure 81, it can be seen in Figure 81a that starting from rest, the SC shows a slightly faster settling time (0.076s) as opposed to the FOC (0.117s). This shows that speed of convergence in case of the SC is better than that of the FOC by 35.042% although both controllers are tuned

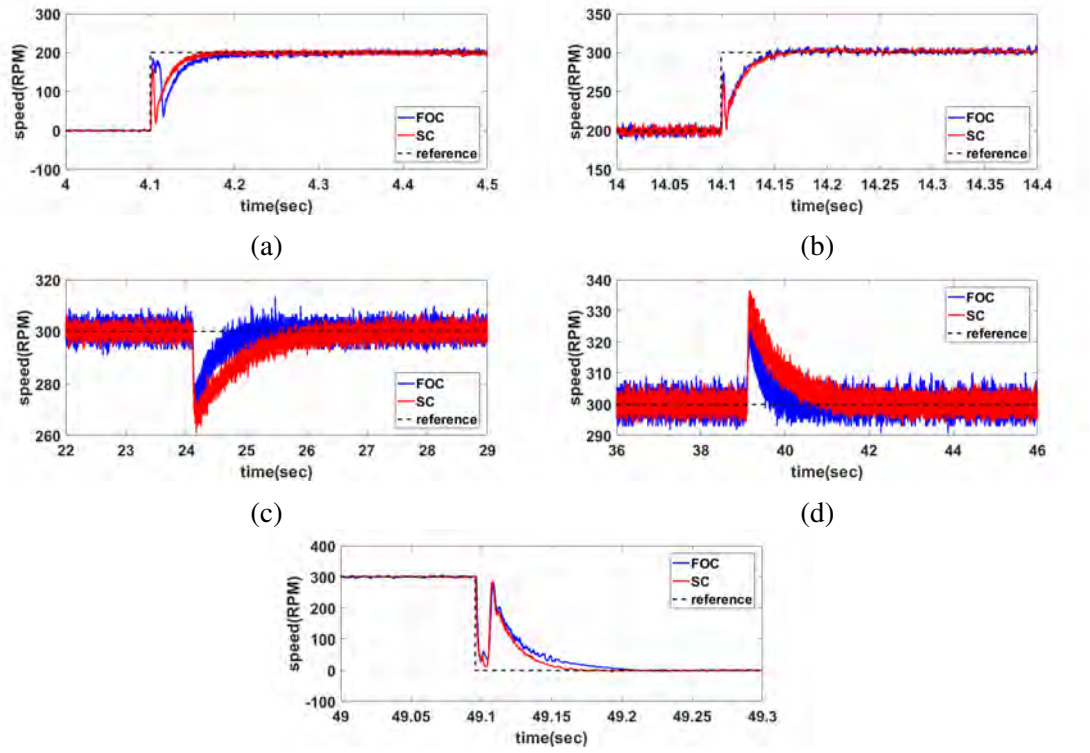

Figure 81: Zoomed views of each transient period of the motor speed response (a) 1st speed step (b) 2nd speed step (c) Applying load (d) Removing load (e) Braking

to give the same settling time, which can be shown at the second transient displayed in Figure 81b. This means that the SC was able to overcome the static friction that resists the motion of the motor when at rest faster than the FOC. When both controllers are running at a fixed speed and the reference is increased, they both exhibit the same settling time. Static friction acts as a disturbance to the system. The SC is able to overcome this disturbance more efficiently.

To confirm this, a small test was conducted, where, the motor is initially kept at rest and various speed step references are input to both controllers. The experiment is conducted at step reference values of 50, 100, 150, 200, 300, 400 and 500 rpm. The response of the motor speed under each control scheme is analyzed. Figure 82 shows the response of the motor speed in each case. Analyzing the results, it can be noticed that the speed response in case of the FOC scheme lags that in case of the SC scheme in Figure 82a. As the speed step increases, the magnitude of this lag starts decreasing as shown in Figures 82b to 82e. At higher speed references, the motor speed

response under FOC scheme starts overlapping the response under SC scheme as shown in Figures 82f and 82g. This concludes that the SC has better performance during motor startup under low speed references. At higher speed references, both controllers show the same response. The 5% settling time is calculated for each controller in each case, and the results are tabulated and shown in Table 11.

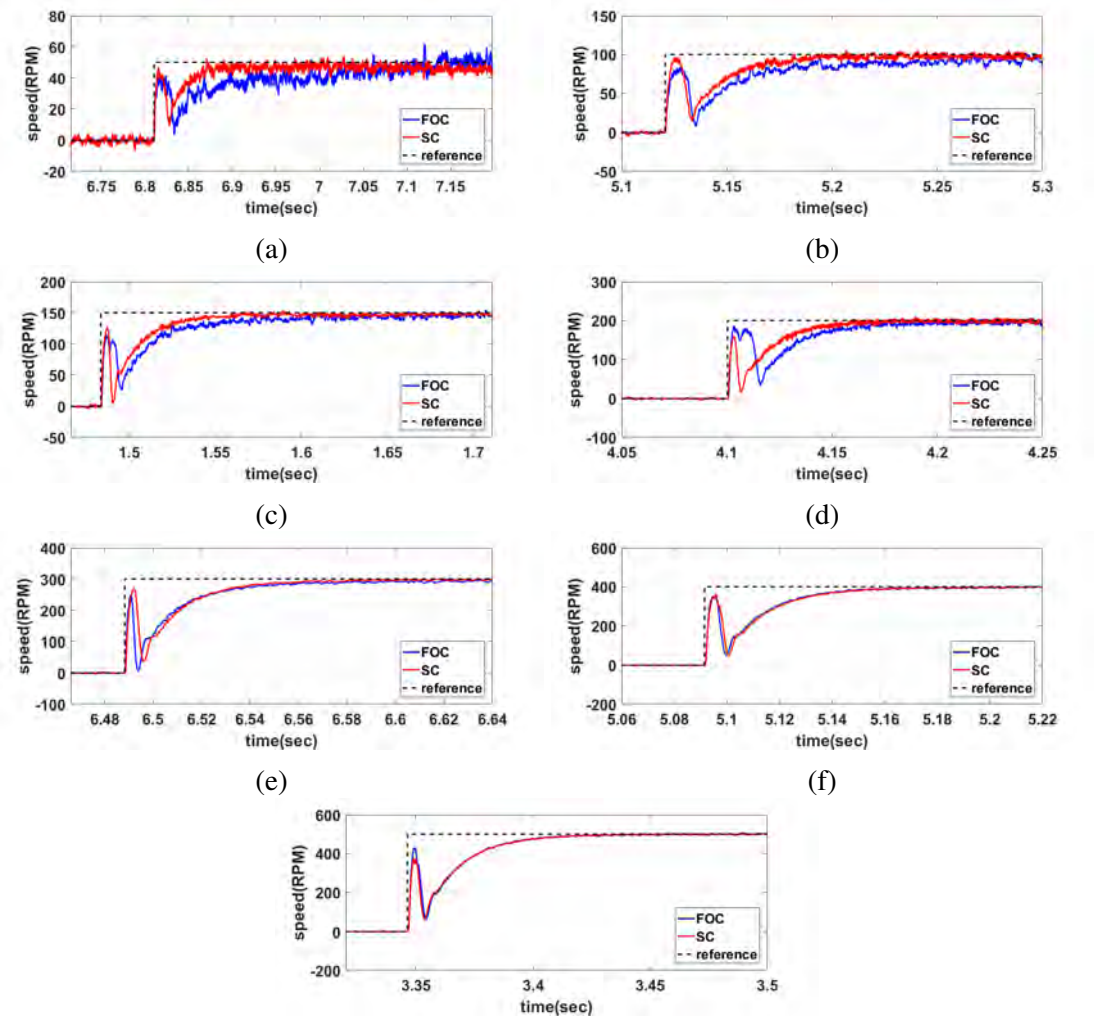

Figure 82: Zoomed views of the motor speed response starting from rest for a reference speed step of (a) 50 rpm (b) 100 rpm (c) 150 rpm (d) 200 rpm (e) 300 rpm (f) 400 rpm (g) 500 rpm

The table shows that the SC provides faster motor speed responses at low speed references. The FOC starts to catch up with the SC as the reference speed step value increases. The table also shows that, in general, the settling time for both controllers de-

creases as the speed step value increases. At very low speeds (50 rpm) both controllers show slower responses but the SC still manages to force the motor speed to settle to its reference faster than the FOC. At high speed steps (400 and 500 rpm), both controllers show almost the exact same settling time. From these results, it can be concluded that the SC offers faster motor speed responses compared to the FOC at low-speed step reference inputs.

Table 11: Summary of the motor speed settling time

Speed	Controller	Settling time ($t_{s_{5\%}}$)	SC improvement (%)
50	SC	0.1680	48.14
	FOC	0.3240	
100	SC	0.0790	67.755
	FOC	0.2450	
150	SC	0.0740	53.459
	FOC	0.1590	
200	SC	0.076	35.042
	FOC	0.117	
300	SC	0.061	30.681
	FOC	0.088	
400	SC	0.0589	-0.34
	FOC	0.0587	
500	SC	0.0560	-0.71
	FOC	0.0556	

Figure 83 shows the response of i_d. It indicates shows that both controllers are able to maintain i_d at 0 without any steady state errors. However, it can be seen that i_d shows less current ripples in steady state with SC, as well as lower error peaks during the transient periods and faster convergence times.

Figure 84 shows the transient periods of the response. It can be seen that the SC records less error for the transient steps as well as faster convergence times opposed to the FOC. Upon adding or removing a load, both controllers correct the error in i_d. The response of i_d in case of the FOC is hindered by the current ripples; however, the average value increases above zero before converging back to 0. The waveforms in Figures 83 and 84 have been filtered by means of a low pass filter with cutoff frequency at 20 Hz.

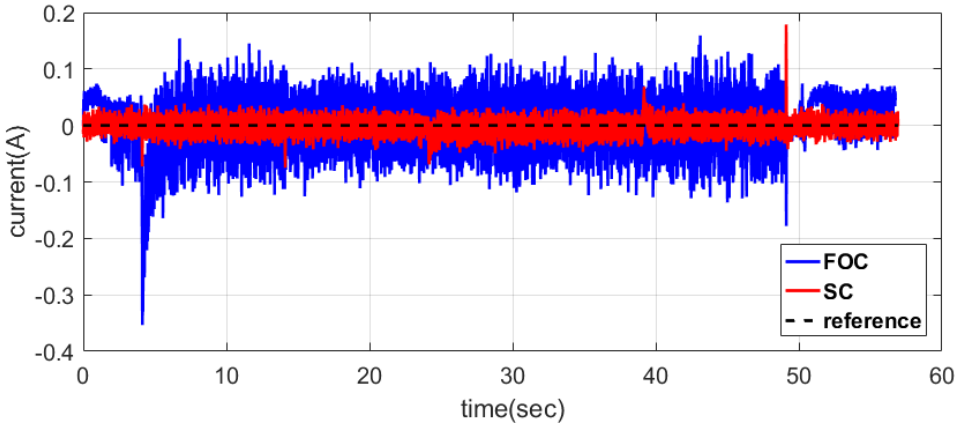

Figure 83: Response of i_d

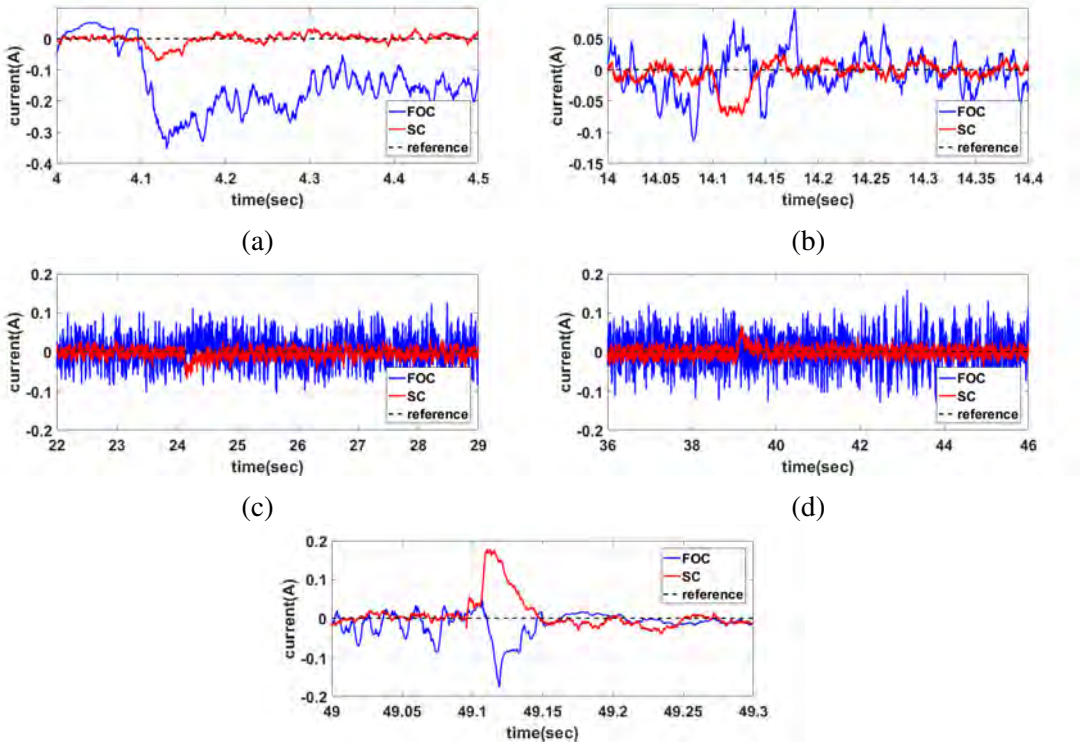

Figure 84: Zoomed views of each transient period of i_d response (a) 1st speed step (b) 2nd speed step (c) Applying load (d) Removing load (e) Braking

Figure 85 shows the response of i_q for both controllers. The waveforms of both controllers are overlapping. For the transient responses, the peaks reached by both controllers are almost identical since both controllers are tuned to have the same response speed. When a load torque is added, i_q increases to compensate for the added

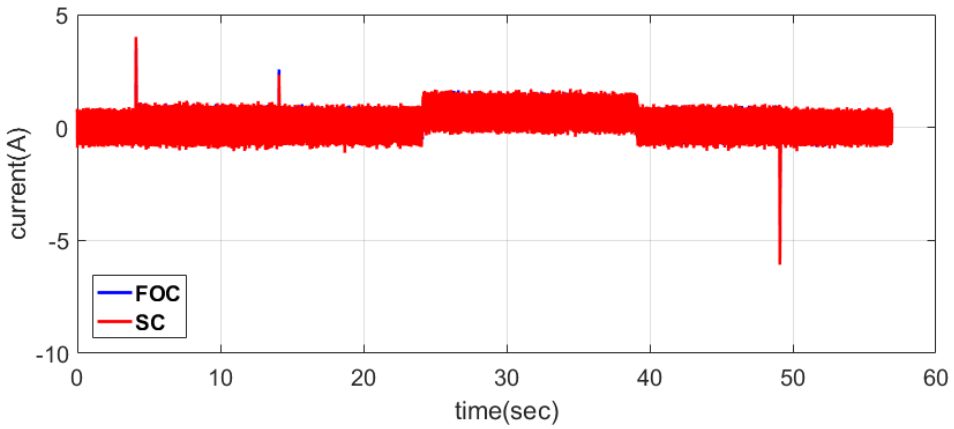

Figure 85: Response of i_q

torque and produce sufficient electromagnetic torque in order to maintain the speed of the motor at the desired value. Transient responses are shown in Figure 86.

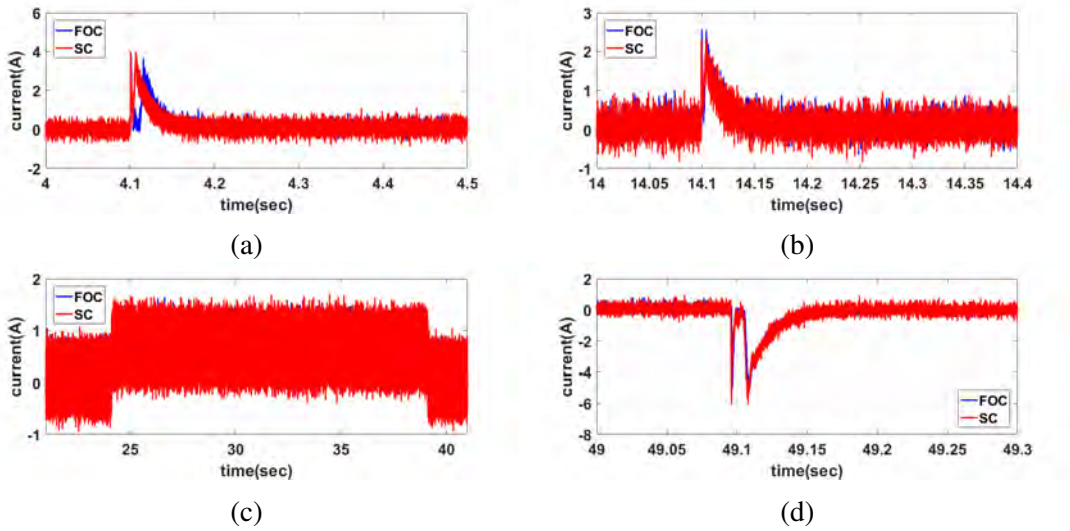

Figure 86: Zoomed views of each transient period of i_q response (a) 1st speed step (b) 2nd speed step (c) Applying and removing load (d) Braking

The maximum value of i_q during each transient step for both controllers is equal, with the exception of the first transient, when the motor starts from rest, as shown in Figure 86a. The extra amount of current (approximately 0.5A) used by the SC is used to overcome the static friction quicker, which results in faster convergence of the motor speed as shown in Figure 81a.

Finally, the three phase currents are displayed in Figure 87. The motor draws more current when a load torque is applied to the system. Figure 88 shows a section of

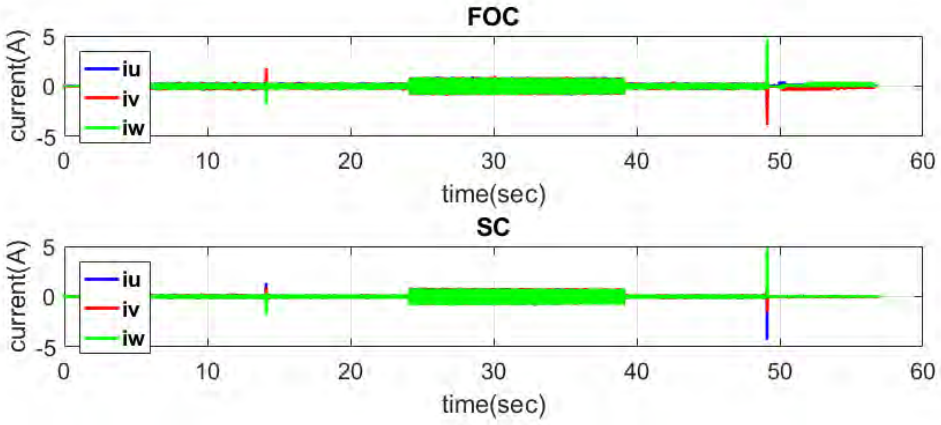

Figure 87: Three phase currents response

the three phase currents. The current waveforms from both controllers are sinusoidal. The shown waveforms are filtered by means of a moving averaging filter which traverses the signal in increments of 16 samples. However, i_{uvw} waveforms by the FOC controller are a slightly distorted compared to the smoother waveforms obtained by the SC. This means that the SC results in less harmonics in the output waveforms. This is to be expected since the SC operates at low bandwidths as stated in the literature [23–25].

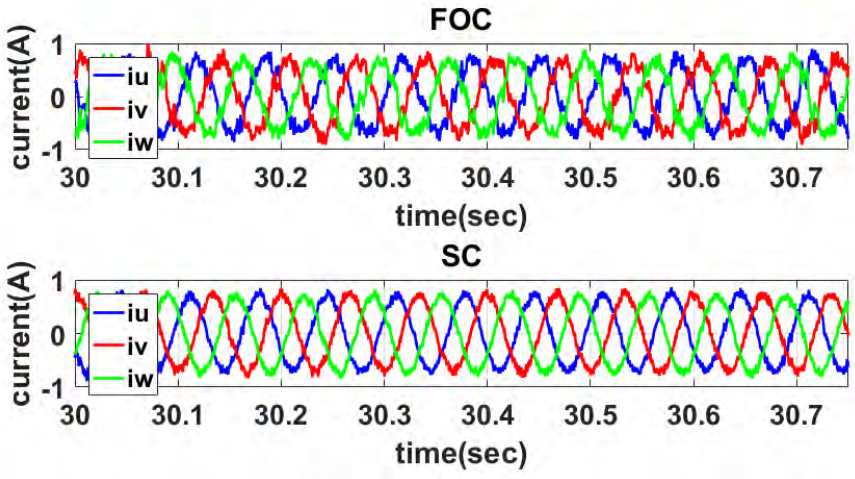

Figure 88: Zoomed in section of the three phase currents response

To confirm this SC property, the Fourier transform is used to observe the frequency response of phase current i_u resulting from each controller. Twenty sinusoidal, unfiltered periods under the same conditions are used for this analysis as shown in Figure 89. The motor speed in this analysis is 300 RPM, which is equivalent to 15 Hz based on the conversion given by Eq. (78).

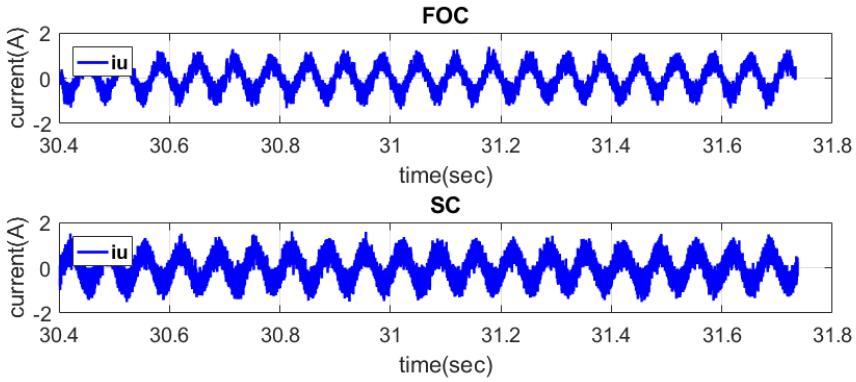

Figure 89: View of the cropped, unfiltered i_u waveforms used in FFT analysis

$$f(Hz) = \frac{np}{120} \tag{78}$$

Where n is the motor speed in RPM, and p is the number of poles of the machine.

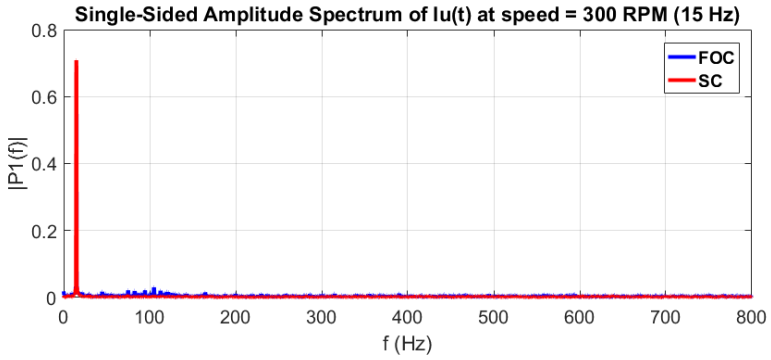

Figure 90: Magnitude response of the FFT

The Fourier transform is used to analyze the harmonics present in each waveform. Figure 90 shows the single-sided amplitude spectrum of i_u for both controllers. Both controllers have the maximum magnitude at 15 Hz which is the fundamental fre-

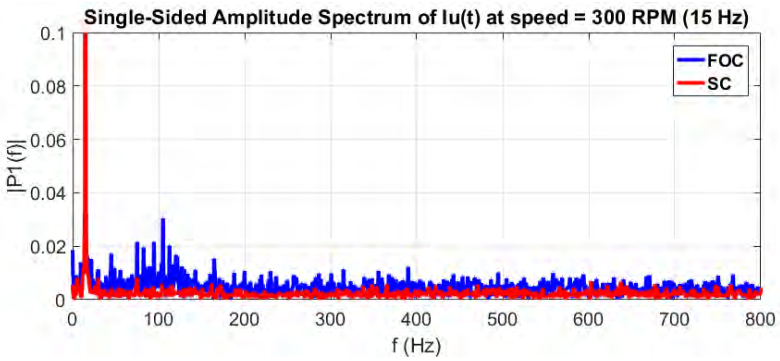

Figure 91: Magnitude response of the FFT (zoomed in)

quency. However, the FOC amplitude spectrum shows higher magnitudes at higher frequencies as opposed to the SC. The FOC adds harmonics at multiples of the fundamental frequency. The added harmonics distort the applied three-phase voltages which results in distorted current waveforms. The SC is able to suppress these harmonics which leads to smoother motor operation.

Figure 92 shows the raw and filtered inverter leg and line to line voltages in case of the FOC controller. A low pass filter with cutoff frequency of 150 Hz is used, which is the rated motor frequency. The motor in these figures is running at 15 Hz (300 rpm).

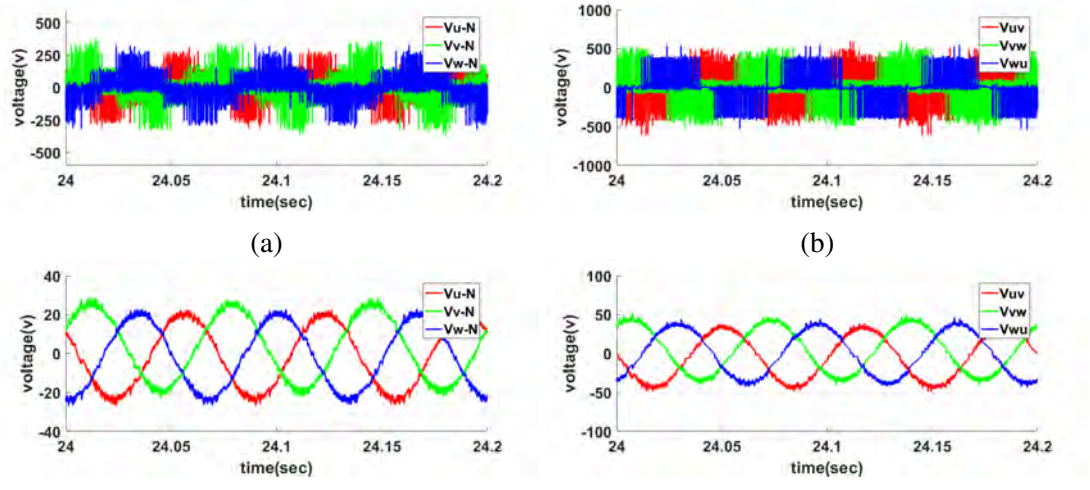

Figure 92: (a) Leg voltages (b) line-line voltages (c) filtered leg voltages (d) filtered line-line voltages: under FOC

The figure shows that the output voltage waveforms are as expected, where the leg voltages have a waveform similar to that of the six-step operation. The line-line

voltages' fundamental component is sinusoidal, which can be seen in the filtered waveforms. However, the effect of added harmonics is visible in the waveforms of the filtered line-line voltages in figure 92d. The waveform is slightly distorted because of the added harmonics, which is the reason behind the distorted current waveforms discussed earlier.

Figure 93 shows the raw and filtered inverter leg and line-line voltages in case of the SC. The same filter used in case of FOC is applied to the waveforms and the motor speed is running under the same conditions (15 Hz or 300 rpm).

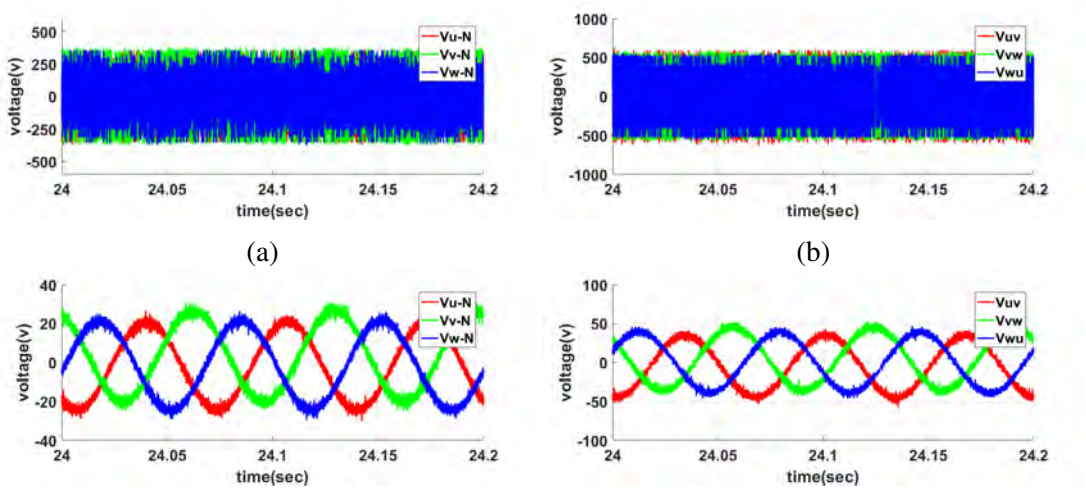

Figure 93: (a) Leg voltages (b) line-line voltages (c) filtered leg voltages (d) filtered line-line voltages: under SC

The figure shows that the output voltage waveforms under SC do not match that of the FOC. However, the filtered voltages, or the fundamental component, are sinusoidal as desired. This is caused because of the non-linear dq command voltage outputs (V_{dq}^{*}) that are generated by the SC.

The FFT of the voltage waveforms of each of FOC and SC is implemented. Figure 94 shows the amplitude spectrum of the phase and line-line voltages under FOC and SC.

The figure shows that both controllers have a maximum amplitude at the fundamental frequency, $15Hz$. FOC shows higher magnitudes at higher frequencies. This

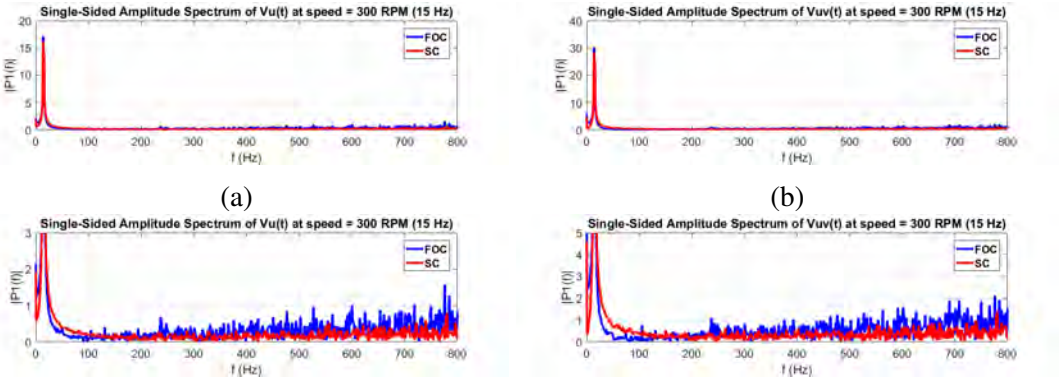

(a) (b)

(c) (d)

Figure 94: (a) FFT of $V_u(t)$ (b) FFT of $V_{uv}(t)$ (c) Zoomed view of FFT of $V_u(t)$ (d) Zoomed view of FFT of $V_{uv}(t)$

means that FOC exhibits more harmonics in the system and once again proves the strength of SC in suppressing noise.

The performance of the controllers is tested under wider speed variation settings. A square wave speed reference is input to both controllers ranging between -1000 to 1000 rpm as shown in figure 95. The controller gains of each of FOC and SC were reduced due to the larger speed steps in this experiment. This is done to avoid large current absorption beyond the motor's ratings. The selected gains are shown in table 12.

Table 12: Selected controller gains

FOC			SC					
Speed Controller	K_p	0.085	ψ_1	K_1	0.06	ψ_2	K_3	0.05
	K_i	0.04		K_2	0.5		K_4	1
Current Controllers	K_p	0.3		T_d	0.001		K_5	0.035
	K_i	0.9					T_q	0.001

The figure shows that both controllers are able to track the speed reference and reach zero steady state error. However, looking at the transient periods shown in figure 96, it can be shown that both controllers show an overdamped response as they reach their references with no overshoot. The SC reaches its reference faster. However, this may be adjusted by tuning the FOC for faster responses.

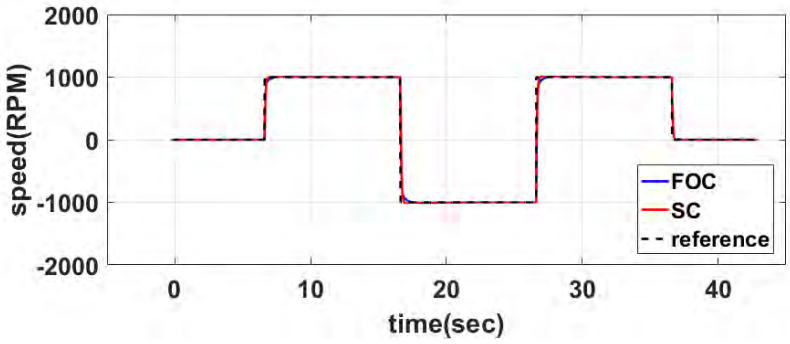

Figure 95: Speed reference and response of FOC and SC under wide speed variations

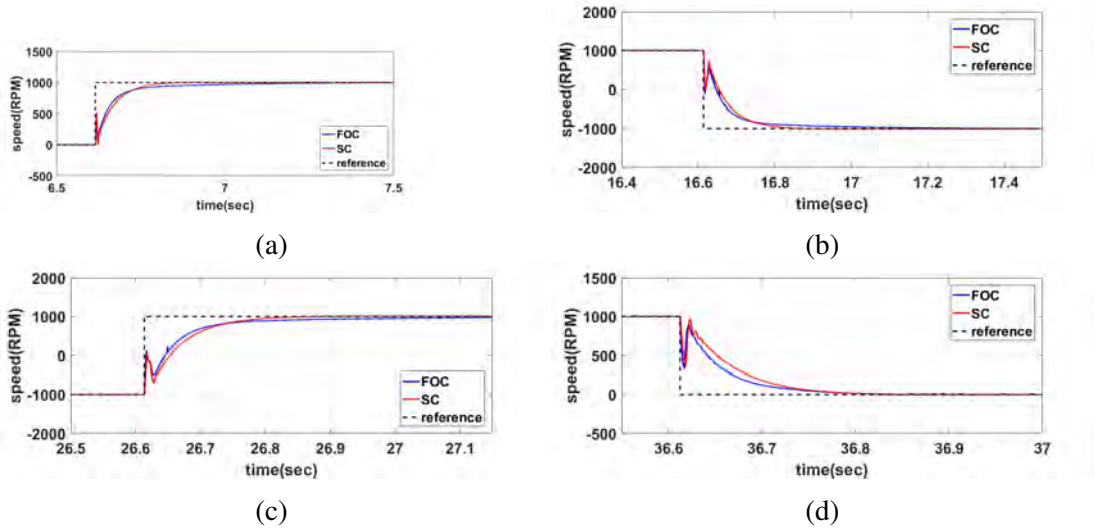

Figure 96: Zoomed views of each transient period of the motor speed response (a) 1st speed step (b) 2nd speed step (c) 3rd step (d) Braking

Despite having a faster response than the FOC, the SC shows less current consumption in each speed step. Figure 97 shows the response of i_q for each controller. Figures 97b-97e show the response of i_q in transient periods. The figure shows that in all speed steps, the motor draws more current under FOC. The motor speed converges to its reference faster, while consuming less current in case of SC. This shows the power of the SC in motor drive applications; since it is a non-linear controller, which uses the system's nonlinearity to devise a control law. This makes the controller more robust in wide signal variations, as mentioned in the literature [26, 36], as opposed to the FOC which uses linear PI controllers. The linear controllers need more control effort to overcome this large variation, thus it draws more current. But the SC is able to handle this variation with ease and even reaches faster than FOC. Signal variation in general is an

advantage of non-linear controllers over linear controllers when dealing with non-linear systems, since linear controllers linearize the system around one equilibrium point in order to be able to generate a proper control law.

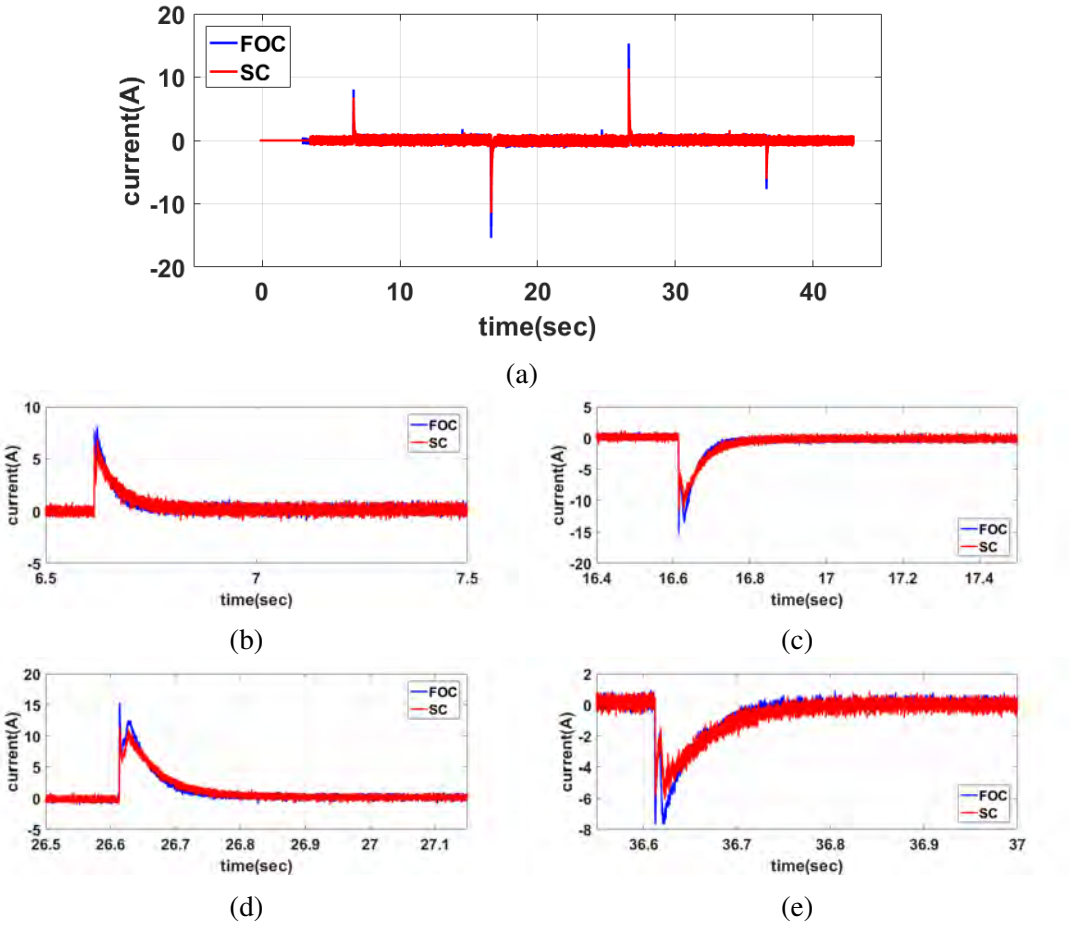

Figure 97: Response of i_q (a) Overall response (b-e) Transient periods

The response of i_d, however, is different. Figure 98 shows that both controllers have an underdamped response of i_d, however, i_d exhibits less error in transient periods in case of FOC. In case of SC, the large speed steps lead to large transient peaks of i_d. This is because as opposed to FOC, the SC does not control the currents directly. The dq currents are controller indirectly as the control effort forces the macro-variable to converge to zero.

Looking at the three phase currents in Figure 99, it can be seen that the FOC consumes more current, where the peak values of all phase currents in case of FOC

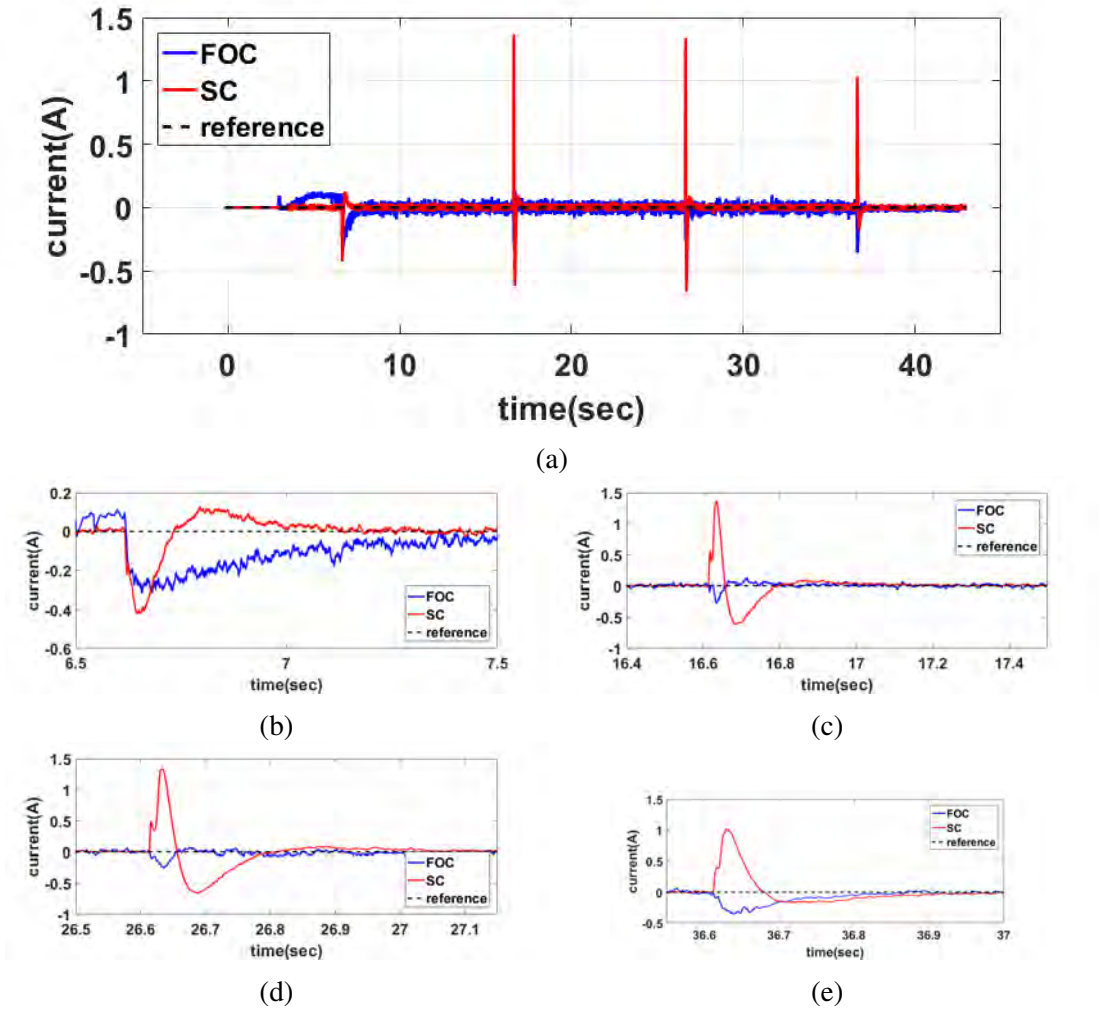

Figure 98: Response of i_d (a) Overall response (b-e) Transient periods

exceed those in case of SC. Table 13 shows the maximum magnitude of the phase currents under each controller during the second and third transient periods (since these are the biggest speed steps). The table shows that the SC uses less current with significant factors. This shows that the SC performs better under wide signal variations, where it consumes less current and still converges faster than FOC.

Table 13: Phase currents magnitudes summary

Transient Period	Phase Current	FOC	SC	SC Improvement Percentage
Second Speed Step	i_u	-11.63	-11.51	1.03%
	i_v	-13.38	-10.49	21.6%
	i_w	14.62	10.76	26.40%
Third Speed Step	i_u	11.52	11.41	0.95%
	i_v	14.91	8.297	44.35%
	i_w	-12.41	-11.73	5.5%

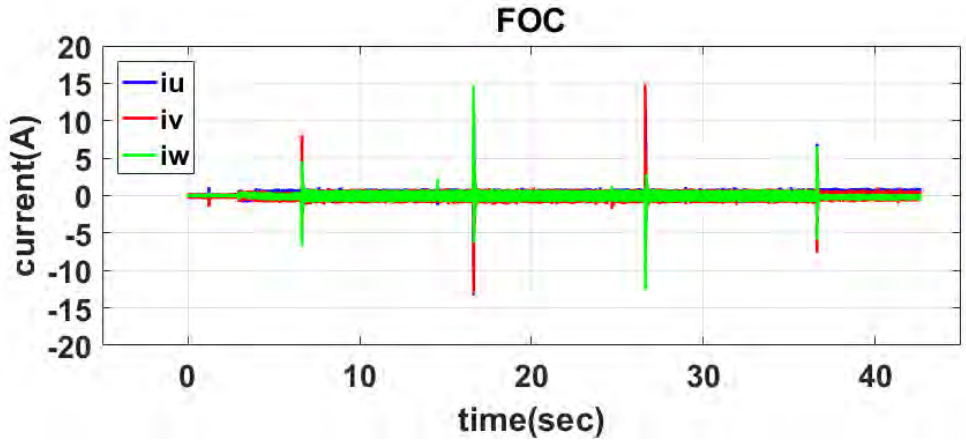

(a)

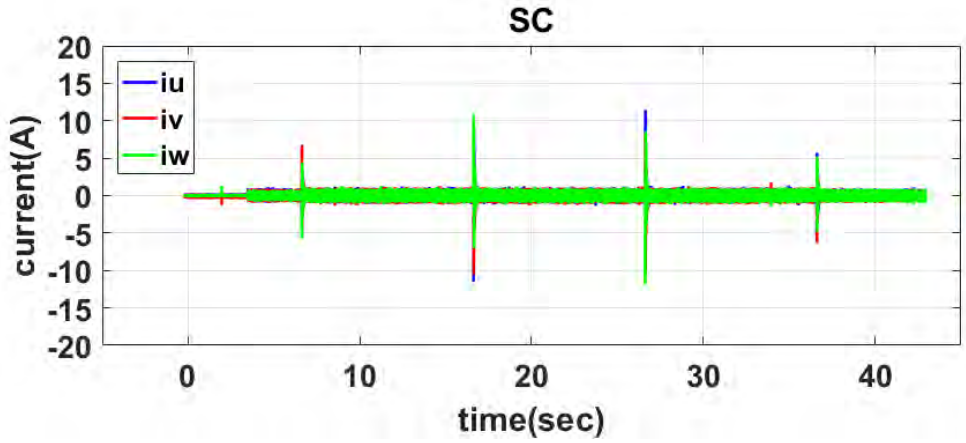

(b)

Figure 99: Response of three-phase currents under (a) FOC (b) SC

5.6. Regenerative Braking

In this section, regenerative braking under FOC and SC are implemented, and its performance is analyzed. Two techniques are used to apply regenerative braking. First, speed control of the motor is used to brake the motor, where a decreasing speed ramp is received by each controller as the speed reference. As the motor decelerates, energy is recovered to the DC source. The DC-bus voltage and current are monitored to evaluate the amount of energy recovered. Secondly, torque control is used to brake the motor. The command currents evaluated in section 4.2 are used to generate the electromagnetic torque given by Eq. (65). This torque guarantees maximum recovered power and DC current. The speed controllers are disconnected, and only current is controlled

to bring the motor to a complete stop. The DC link voltage in the inverter topology shown in Figure 25 is rectified from a 3-phase line supplying the inverter. This process maintains the DC link voltage at 575 V. In order to observe the voltage increase during regenerative braking, the three phase line is disconnected from the inverter and the DC link voltage starts to drop.The motor is operating under a constant speed control in this period. Once the DC link voltage reaches 300V, the regenerative braking command signal is triggered and the motor operates under braking mode.

5.6.1. Regenerative Braking using Speed Control. In this experiment, the motor speed is maintained constant at different initial speeds(1000, 1500 and 2000 rpm). The motor is then decelerated as explained previously. During this period, the motor acts as a generator and current flows back from the motor to the DC power source. This reverse current will charge the capacitor and increase the DC link voltage. This experiment is implemented using FOC and SC. Figure 100 shows the speed, DC link voltage, DC link current and the motor i_q during the braking period under FOC at an initial speed of 1000 rpm.

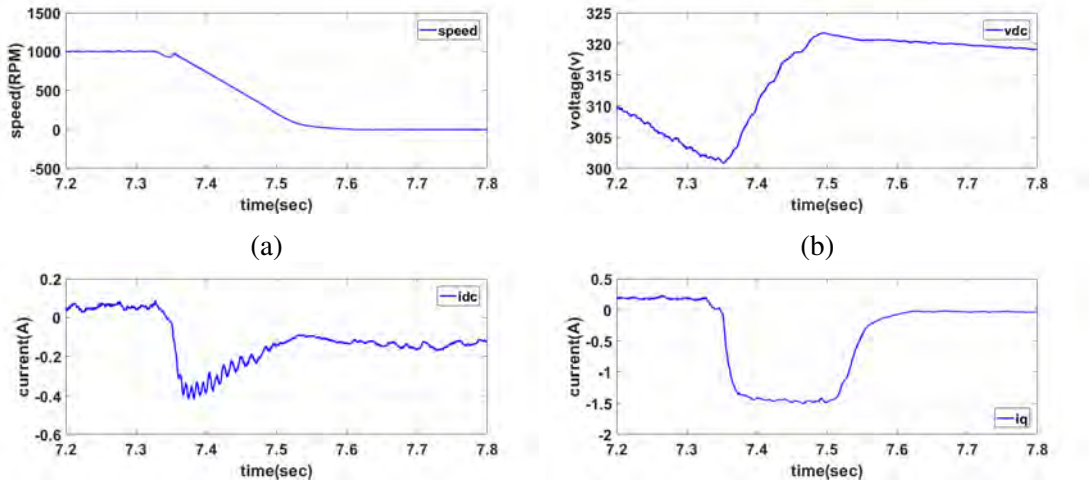

Figure 100: Regenerative braking under speed control using FOC at 1000 rpm(a) Motor speed (b) DC link voltage (c) DC link current (d) Motor i_q

The regenerated power is calculated by multiplying the DC link voltage by the DC link current during regenerative braking as shown in Eq. (79).

$$P = V_{DC} * i_{DC} \tag{79}$$

To find the regenerated energy, the power is integrated by means of numerical integration following the trapezoidal rule as shown in Eq. (80).

$$E_{regen}(k) = E_{regen}(k-1) + \frac{T_s}{2}[P(k) + P(k-1)] \tag{80}$$

However, the braking period is divided into two intervals: regenerative braking and non-regenerative braking. In other words, the braking period does not fall entirely under regenerative braking; based on the boundaries of the regenerative braking region in the fourth quadrant in the speed-torque plane. Whenever the electromagnetic torque does not satisfy the condition $-\frac{(\frac{3}{4}P\lambda_{PM})^2}{R}\omega < T_{em} < 0$ as proven in Eq. (61), the braking falls outside the regenerative braking region and the braking energy is lost as heat in the armature resistance. Therefore, in order to compute the regenerated energy, the integration of power is only computed until the point of maximum DC-bus voltage only instead of the entire braking period. This period is referred to as recovery time and denoted by (t_r). The mechanical energy of the motor is given by Eq. (81)

$$E_{mech} = \frac{1}{2}J\omega^2 \tag{81}$$

The efficiency of the regenerative braking process in terms of harvested energy is computed as given by Eq. (82)

$$\eta = \frac{E_{regen}}{E_{mech}} * 100 \tag{82}$$

Figure 101 shows the regenerated power and energy on the DC link voltage.

The same experiments are repeated using SC. Figure 102 shows the speed of the motor, DC link voltage, DC link current and motor i_q, DC link power and DC link energy during the braking period under SC at an initial speed of 1000 rpm. It is noticed

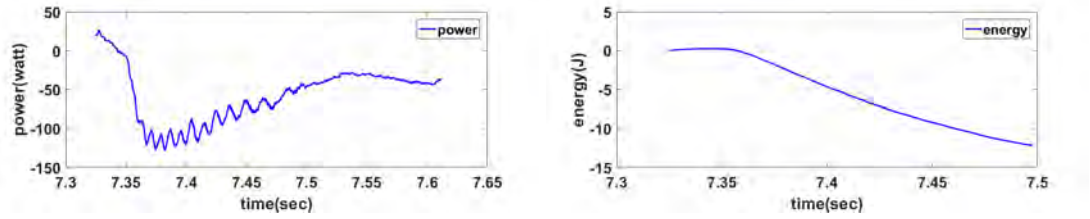

(a) (b)

Figure 101: Regenerative braking under speed control using FOC at 1000 rpm (a) DC link power (b) DC link energy

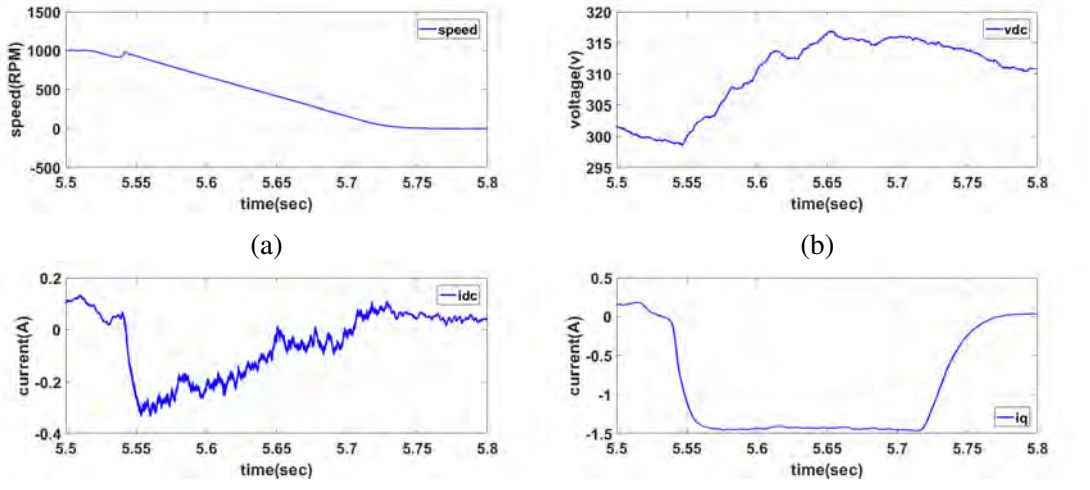

(a) (b) (c) (d) (e) (f)

Figure 102: Regenerative braking under speed control using SC at 1000 rpm(a) Motor speed (b) DC link voltage (c) DC link current (d) Motor i_q (e) DC link power (f) DC link energy

that both controllers yield similar waveforms for all variables. Table 14 summarizes the results of both experiments.

Table 14: Summary of the regenerative braking results under speed control

Controller	Initial Speed	Max i_{dc} (A)	$\Delta V_{dc}(V)$	Recovery Time (t_r)	Energy (J)	Max Power (P)	Max i_q (A)	Mech. Energy (J)	Efficiency(%)
FOC	1000	-0.419	21.4	0.145	12.18	128.5	-1.508	17.2718	70.4961
	1500	-1.005	54.9	0.169	27.73	310.8	-2.312	38.8616	71.3563
	2000	-1.575	96.8	0.221	50.62	502.6	-2.958	69.0872	73.2736
SC	1000	-0.3344	18.4	0.107	6.336	101.2	-1.468	17.2718	36.6842
	1500	-0.8352	51.4	0.178	17.7	256	-2.249	38.8616	45.5466
	2000	-1.329	90.8	0.193	37	432.5	-3.064	69.0872	53.5507

The table shows that FOC generates higher magnitude values of all variables than SC. FOC also shows higher efficiency in terms of energy harvested from the mechanical energy of the motor at all given initial speeds. One observation though, is that the efficiency of the FOC is approximately constant and consistent. On the other hand, the efficiency of the SC increases as the initial speed increases. Both controllers show that the speed control technique returns low values of DC link current and DC link power. It also consumes low values of i_q to generate the reverse electromagnetic torque. However, the harvested energy and DC link voltage are considerably higher than the harvested current.

5.6.2. Regenerative Braking using Torque Control. In this section, the motor's electromagnetic torque is controlled to brake the motor. The motor dq currents are controlled to follow the command currents i_d^* and i_q^* given by Eq. (63) and (64) respectively. These command currents will generate an electromagnetic torque that will guarantee the maximum absorbed power and DC-link current. Figure 103 shows the motor's speed, DC link voltage, DC link current, motor's i_q, regenerated power and energy on the DC link during the braking period under FOC. The figure indicates that the regenerated voltage and energy are much less than those in their counterparts in case of the speed control technique. However, more power and current are absorbed on the DC link. The motor comes to rest in a shorter period of time as well. The motor's i_q is also much higher than that used in case of speed control. This indicates that the generated electromagnetic torque is much higher as well (hence the faster braking). The same experimental procedure is repeated under the SC. The macro-variables designed in section 4.2.2 are used to control the motor in the braking period. Figure 104 shows the motor's speed, DC link voltage, DC link current, motor's i_q, regenerated power and energy on the DC link during the braking period under SC. Comparing the waveforms resulting from both controllers, the motor behaves the same way under both controllers and waveforms are highly similar. Table 15 summarizes the results of the regenerative braking process under torque control using both controllers.

The oscillations in the motor speed caused by the flexible coupling hinder the controllers' performances, since the generated i_q^* is a function of the motor speed.

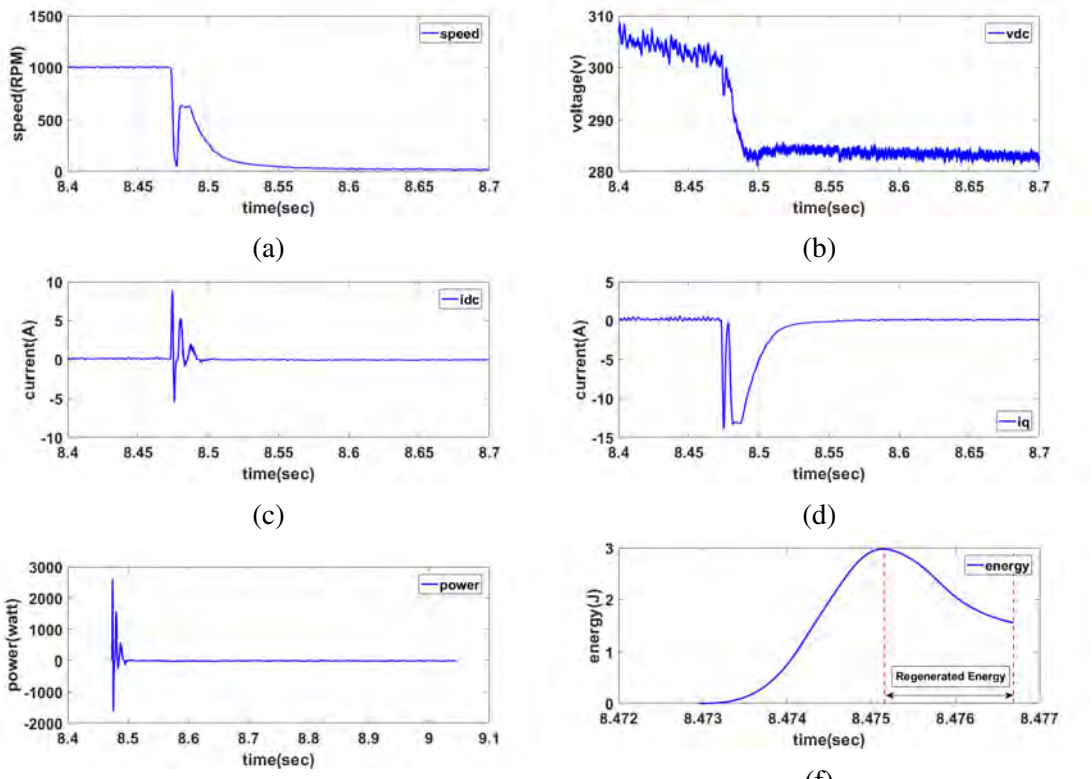

Figure 103: Regenerative braking under torque control using FOC (a) Motor speed (b) DC link voltage (c) DC link current (d) Motor i_q (e) DC link power (f) DC link energy

Table 15: Summary of the regenerative braking results under torque control

Controller	Max i_{dc} (A)	$\Delta V_{dc}(V)$	Energy (J)	Max Power (P)	Max i_q (A)	Mechanical Energy (J)	Efficiency(%)
FOC	-5.485	5.6	1.45	1626	-13.97	17.2718	8.395
SC	-4.893	6	1.801	1452	-12.44		10.42

Therefore, the performance of the controllers in regenerative braking using this technique cannot be assessed properly.

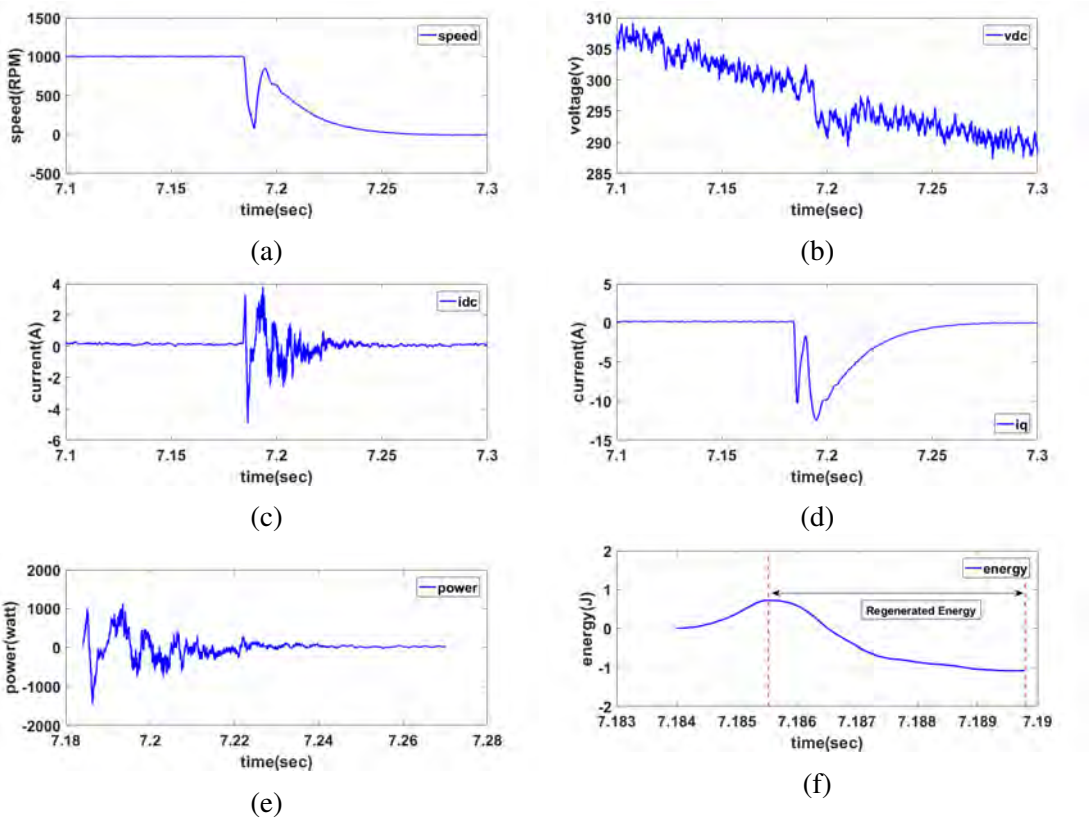

Figure 104: Regenerative braking under torque control using SC (a) Motor speed (b) DC link voltage (c) DC link current (d) Motor i_q (e) DC link power (f) DC link energy

Chapter 6: Conclusion

This study explores a new non-linear controller, the synergetic controller, and its application in AC motor drive control. A synergetic controller is designed and implemented. To implement the synergetic control on a PMSM drive, the drive system was assembled and interfaced with dSPACE. The flux alignment technique was implemented since the absolute position of the rotor cannot be determined using the available SinCos encoder. The PMSM drive is coupled with a DC motor, which acts as a load. The DC motor armature current is controlled using Hysteresis Current Control in order to regulate the load torque as desired. Field oriented control of PMSM was implemented in order to assess the performance of the synergetic controller (SC). The SC was designed and implemented for the PMSM. Two macro-variables were designed to control the speed of the motor. A new macro-variable is proposed to control the d-axis variables. The controller performance is also investigated by tuning each gain used by the controller separately. In addition, regenerative braking of PMSM is investigated. Two techniques are implemented to operate the motor under regenerative braking: speed control mode and torque control mode. Speed control mode generates a decreasing ramp reference speed to decelerate the motor. On the other hand, the torque control mode controls the quadrature axis current i_q in order to generate an electromagnetic torque that lies inside the regenerative braking region. In order to implement this under SC, another set of macro-variables is proposed to operate the PMSM in regenerative braking mode.

The results show that the alignment of the rotor flux was successful and the rotor position could be determined using the SinCos encoder. Field orientation was successful and the FOC is capable of tracking any input reference speed. The proposed macro-variable of the SC improves the performance of the synergetic controller significantly compared to the controllers proposed in the literature, where any steady state errors in the direct axis current i_d were eliminated. The results also show that the error in ψ_1 was improved by 90%. The synergetic controller is more robust against disturbances, such as static friction, than the field oriented controller. Upon starting from rest, conducted experiments show that the SC performs better than FOC in terms of

convergence speed at low speed reference values. The synergetic controller also reduces the harmonics of the system compared to the field oriented controller using the same SPWM modulator and same switching frequency. Since one of the advantages of the SC is operating in low bandwidths, this was validated using the Fourier transform of the phase currents, where SC waveforms show fewer distortions. The results show that FOC adds more harmonics at multiples of the fundamental frequency of the motor. The voltage waveforms resulting from the SC are different from those resulting from FOC due to the non-linear output command law. However, the fundamental component remains sinusoidal as desired. Both controllers have been tested in case of wide signal variations, the results show that the SC shows better performance against wide variations, where it is able to converge in shorter time periods while using lesser amounts of energy compared to FOC. This confirms the benefit of using a non-linear controller in non-linear systems, where the linear PI controllers used in FOC respond poorly to wide signal variations as opposed to the SC. Finally, the results indicate that regenerative braking using speed control mode allows more energy harvesting. The FOC shows better energy harvesting efficiency compared to the SC. The SC's efficiency increases as the initial motor speed increases. Torque control technique focuses on increasing the electric power and the maximum peaks of the current absorbed by the DC source.

The following is a list of possible work that can be conducted to improve and further develop this research:

- Using adaptive gains in the synthesis of the synergetic controller to improve its performance and expand its ability to overcome disturbances.
- Keeping in mind load variations in the design of the macro-variables to eliminate any steady state errors in the system upon applying load torque.
- Including a separate energy storage module in the system topology dedicated to storing any harvested energy from the motor during regenerative braking.
- Implementing the three-switches braking technique to improve the regenerative braking process and harvest more energy from the motor's rotation.

References

[1] C. D. Schauder, F. H. Choo, and M. T. Roberts, "High performance torque-controlled induction motor drives," *IEEE Transactions on Industry Applications*, vol. IA-19, no. 3, pp. 349–355, May 1983.

[2] T. Finken, M. Felden, and K. Hameyer, "Comparison and design of different electrical machine types regarding their applicability in hybrid electrical vehicles," in *2008 18th International Conference on Electrical Machines*, pp. 1–5, Sept 2008.

[3] T. M. Jahns and V. Blasko, "Recent advances in power electronics technology for industrial and traction machine drives," *Proceedings of the IEEE*, vol. 89, no. 6, pp. 963–975, Jun 2001.

[4] C. C. Chan, "The state of the art of electric and hybrid vehicles," *Proceedings of the IEEE*, vol. 90, no. 2, pp. 247–275, Feb 2002.

[5] C. C. Chan and K. T. Chau, "An overview of power electronics in electric vehicles," *IEEE Transactions on Industrial Electronics*, vol. 44, no. 1, pp. 3–13, Feb 1997.

[6] K. Rajashekara, "History of electric vehicles in general motors," *IEEE Transactions on Industry Applications*, vol. 30, no. 4, pp. 897–904, Jul 1994.

[7] M. Zeraoulia, M. E. H. Benbouzid, and D. Diallo, "Electric motor drive selection issues for HEV propulsion systems: A comparative study," *IEEE Transactions on Vehicular Technology*, vol. 55, no. 6, pp. 1756–1764, Nov 2006.

[8] B. Li and C. Wang, "Comparative analysis on PMSM control system based on SPWM and SVPWM," in *2016 Chinese Control and Decision Conference (CCDC)*, pp. 5071–5075, May 2016.

[9] X. Li and Z. Zhang, "SVPWM control of frequency-variable speed-adjustable system," in *2017 IEEE International Conference on Mechatronics and Automation (ICMA)*, pp. 113–118, Aug 2017.

[10] K. W. Lee, S. Park, and S. Jeong, "A seamless transition control of sensorless pmsm compressor drives for improving efficiency based on a dual-mode operation," *IEEE Transactions on Power Electronics*, vol. 30, no. 3, pp. 1446–1456, March 2015.

[11] A. Khurram, "Performance enhancement of field oriented induction motor drive system," Master's thesis, American University of Sharjah, 2016.

[12] R. S. Colby and D. W. Novotny, "An efficiency-optimizing permanent-magnet synchronous motor drive," *IEEE Transactions on Industry Applications*, vol. 24, no. 3, pp. 462–469, May 1988.

[13] C. Perera, F. Blaabjerg, J. K. Pedersen, and P. Thøgersen, "Open loop stability and stabilization of permanent magnet synchronous motor drives using DC-link current," in *Open Loop Stability and Stabilization of Permanent Magnet Synchronous Motor Drives using DC-Link Current*. Institut for Energiteknik, Aalborg Universitet, pp. 47–53, 2000.

[14] Y. Nakamura, T. Kudo, F. Ishibashi, and S. Hibino, "High-efficiency drive due to power factor control of a permanent magnet synchronous motor," *IEEE Transactions on Power Electronics*, vol. 10, no. 2, pp. 247–253, Mar 1995.

[15] P. D. C. Perera, F. Blaabjerg, J. K. Pedersen, and P. Thogersen, "A sensorless, stable V/f control method for permanent-magnet synchronous motor drives," *IEEE Transactions on Industry Applications*, vol. 39, no. 3, pp. 783–791, May 2003.

[16] S. Dwivedi and B. Singh, "Vector control vs direct torque control comparative evaluation for PMSM drive," in *2010 Joint International Conference on Power Electronics, Drives and Energy Systems 2010 Power India*, pp. 1–8, Dec 2010.

[17] L. Meng and X. Yang, "Comparative analysis of direct torque control and DTC based on sliding mode control for PMSM drive," in *2017 29th Chinese Control And Decision Conference (CCDC)*, pp. 736–741, May 2017.

[18] N. Mohan, *Advanced Electric Drives: Analysis, Control, and Modeling Using MATLAB/Simulink*. John Wiley & Sons, 2014.

[19] F. Blaschke, "Das prinzip der feldorientierung, grundlage fur die transvektor-regelung von drehfeldmaschinen," *Siemens-Z.*, vol. 45, p. 757, 1971.

[20] M. Yano, S. Abe, and E. Ohno, "History of power electronics for motor drives in japan," in *IEEE Conference on the History of Electronics*, 2004, pp. 1–11.

[21] K. Hasse, "Zum dynamischen verhalten der asynchron maschine bei betrieb mit variabler standerfreqenz und standerspannung," *ETZ-A*, vol. 89, 1968.

[22] L. Amezquita-Brooks, J. Liceaga-Castro, and E. Liceaga-Castro, "Speed and position controllers using indirect field-oriented control: A classical control approach," *IEEE Transactions on Industrial Electronics*, vol. 61, no. 4, pp. 1928–1943, April 2014.

[23] E. Santi, A. Monti, D. Li, K. Proddutur, and R. A. Dougal, "Synergetic control for dc-dc boost converter: implementation options," *IEEE Transactions on Industry Applications*, vol. 39, no. 6, pp. 1803–1813, Nov 2003.

[24] A. Kolesnikov, G. Veselov, A. Kolesnikov, A. Monti, F. Ponci, E. Santi, and R. Dougal, "Synergetic synthesis of DC-DC boost converter controllers: theory and experimental analysis," in *APEC. Seventeenth Annual IEEE Applied Power Electronics Conference and Exposition (Cat. No.02CH37335)*, vol. 1, pp. 409–415 vol.1, 2002.

[25] A. Monti, R. Dougal, E. Santi, D. Li, and K. Proddutur, "Compensation for step-load variations when applying synergetic control," in *Applied Power Electronics Conference and Exposition, 2003. APEC '03. Eighteenth Annual IEEE*, vol. 1, pp. 334–340 vol.1, Feb 2003.

[26] J. Bastos, A. Monti, and E. Santi, "Design and implementation of a nonlinear speed control for a PM synchronous motor using the synergetic approach to control theory," in *2004 IEEE 35th Annual Power Electronics Specialists Conference (IEEE Cat. No.04CH37551)*, vol. 5, pp. 3397–3402 Vol.5, June 2004.

[27] T. Bogani, A. Lidozzi, L. Solero, and A. D. Napoli, "Synergetic control of PMSM drives for high dynamic applications," in *IEEE International Conference on Electric Machines and Drives, 2005.*, pp. 710–717, May 2005.

[28] A. R. Noei and H. A. Kholerdi, "Robust speed control of induction machine using synergetic controller," in *2015 2nd International Conference on Knowledge-Based Engineering and Innovation (KBEI)*, pp. 880–885, Nov 2015.

[29] M. z. Niu, T. Wang, Q. Zhang, X. He, and M. l. Zhao, "A new speed control method of induction motor," in *2016 35th Chinese Control Conference (CCC)*, pp. 10 140–10 143, July 2016.

[30] M. Laribi, M. S. A. Cheikh, C. Larbes, N. Essounbouli, and A. Hamzaoui, "A sliding mode and synergetic control approaches applied to induction motor," in *3rd International Conference on Systems and Control*, pp. 212–217, Oct 2013.

[31] A. Arias, "PMSM Control (FOC & DTC) for WECS & Drives,", Universitat Politécnica de Catalunya, May 2013.

[32] S. Chapman, *Electric machinery fundamentals*. Tata McGraw-Hill Education, 2005.

[33] W. C. Duesterhoeft, M. W. Schulz, and E. Clarke, "Determination of instantaneous currents and voltages by means of alpha, beta, and zero components," *Transactions of the American Institute of Electrical Engineers*, vol. 70, no. 2, pp. 1248–1255, July 1951.

[34] P. Pillay and R. Krishnan, "Modeling of permanent magnet motor drives," *IEEE Transactions on industrial electronics*, vol. 35, no. 4, pp. 537–541, 1988.

[35] M. H. Takrouri, "Nonlinear friction identification of a linear voice coil DC motor," Master's thesis, American University of Sharjah, 2015.

[36] E. Santi, A. Monti, D. Li, K. Proddutur, and R. Dougal, "Synergetic control for power electronics applications: a comparison with the sliding mode approach," *Journal of Circuits, Systems, and Computers*, vol. 13, no. 04, pp. 737–760, 2004.

[37] A. Samba Murthy, "Analysis of regenerative braking in electric machines," Master's thesis, Georgia Institute of Technology, 2013.

[38] F. Naseri, E. Farjah, and T. Ghanbari, "An efficient regenerative braking system based on battery/supercapacitor for electric, hybrid, and plug-in hybrid electric vehicles with BLDC motor," *IEEE Transactions on Vehicular Technology*, vol. 66, no. 5, pp. 3724–3738, 2017.

[39] C.-H. Chen, W.-C. Chi, and M.-Y. Cheng, "Regenerative braking control for light electric vehicles," in *2011 IEEE Ninth International Conference on Power Electronics and Drive Systems (PEDS)*, pp. 631–636, 2011.

[40] *Unitmotor UM product Datasheet*, Emerson Industrial Automation.

[41] *DS1103 Hardware Installation and Configuration*, dSPACE GmbH, 5 2014, rev. 1.

[42] *Interface to Sin/Cos Encoders With High-Resolution Position Interpolation*, Texas Instruments, 6 2015, rev. 1.

[43] V. Slapak, K. Kyslan, F. Mejdr, and F. Durovsky, "Determination of initial commutation angle offset of permanent magnet synchronous machine-an overview and simulation," *Acta Electrotechnica et Informatica*, vol. 14, no. 4, pp. 17–22, 2014.

[44] *Inverter Unit MWINV-9R144 Hardware User's Manual*, MYWAY Plus Co., 4 2012, rev. 1.

[45] R. Dhaouadi, "Scalar Control of IM,", American University of Sharjah, October 2014.

Appendix A: Motor Paramters

Table A1: DC motor parameters

Variable	Value	Unit
Torque Constant (K_t)	0.055	Nm/A
Rated Torque(τ_{rated})	0.6	Nm
Rated Current (I)	12	A
Rated Speed (ω_{rated})	3200	RPM
Rated Power (P_{rated})	200	W
Terminal Resistance (R)	0.4	Ohms
Inductance (L)	0.8	mH
Inertia (J)	1.8	$kgcm^2$
Poles (P)	2	-
Rated Voltage (V)	24	volts

Appendix B: SIMULINK models

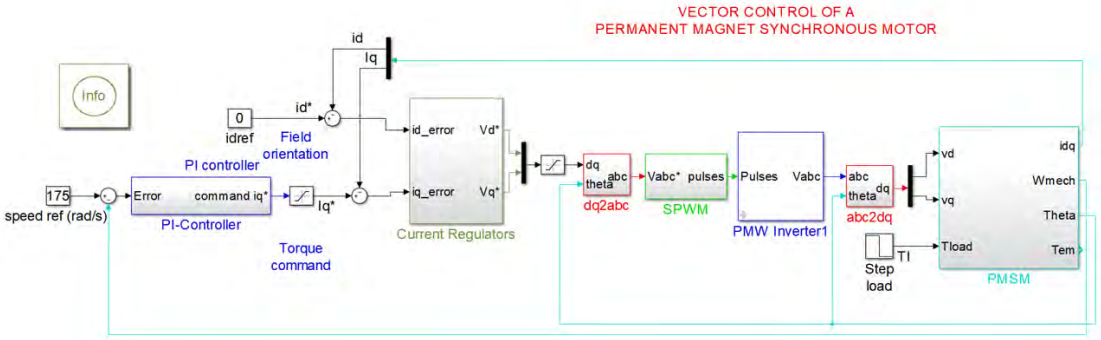

Figure B1: Simulink model of the FOC scheme

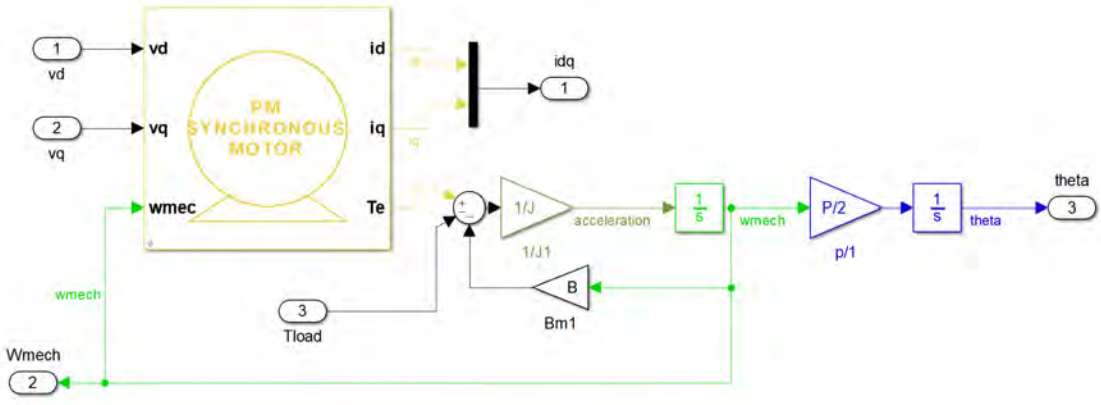

Figure B2: Contents of the PMSM block

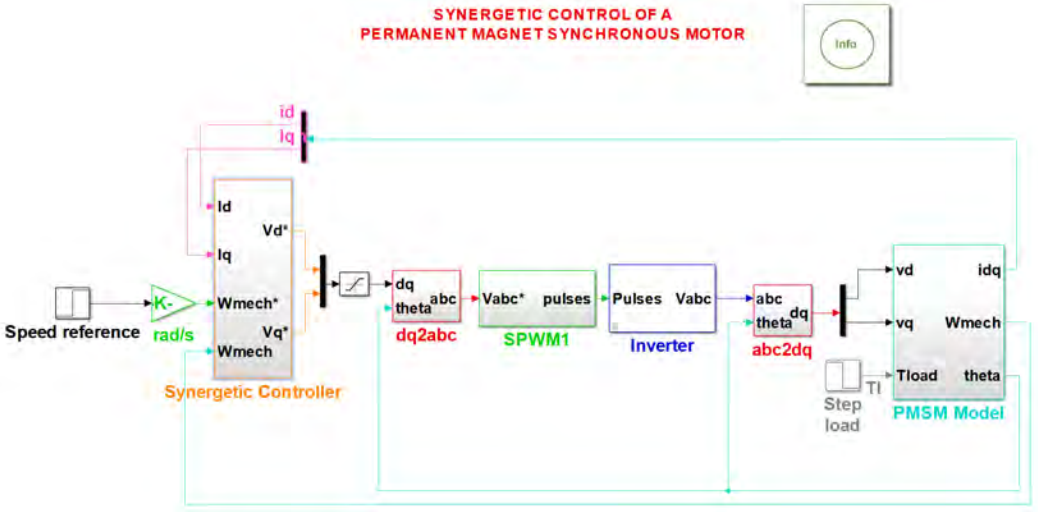

Figure B3: Simulink model of the synergetic control scheme

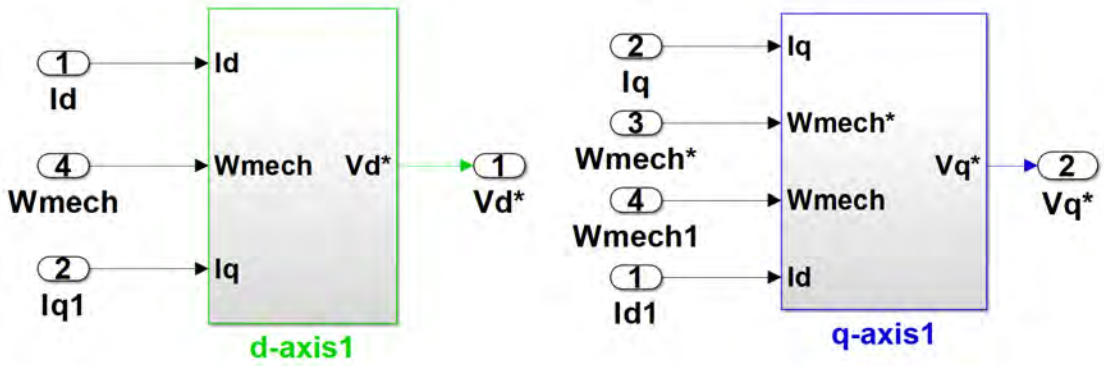

Figure B4: Contents of the synergetic controller block

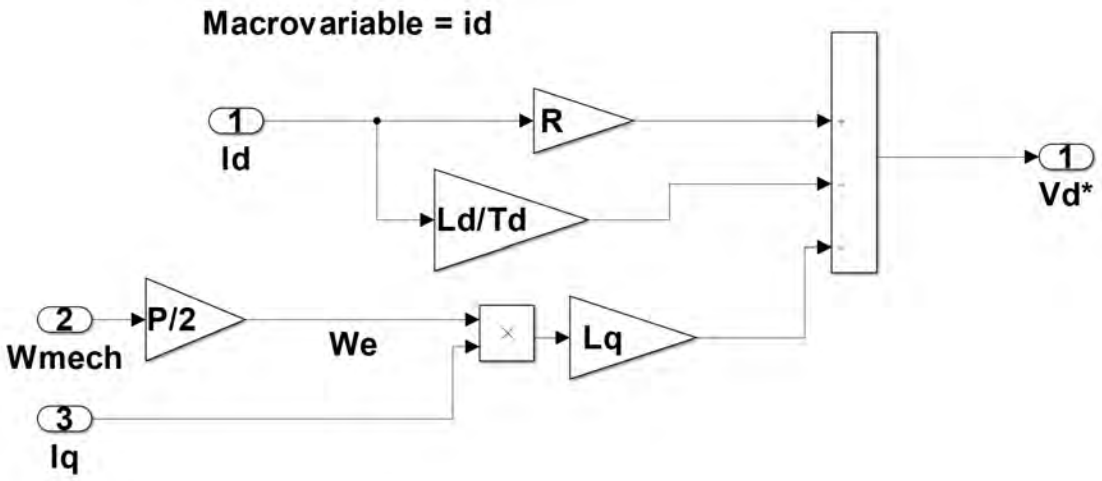

Figure B5: Contents of d-axis1 block

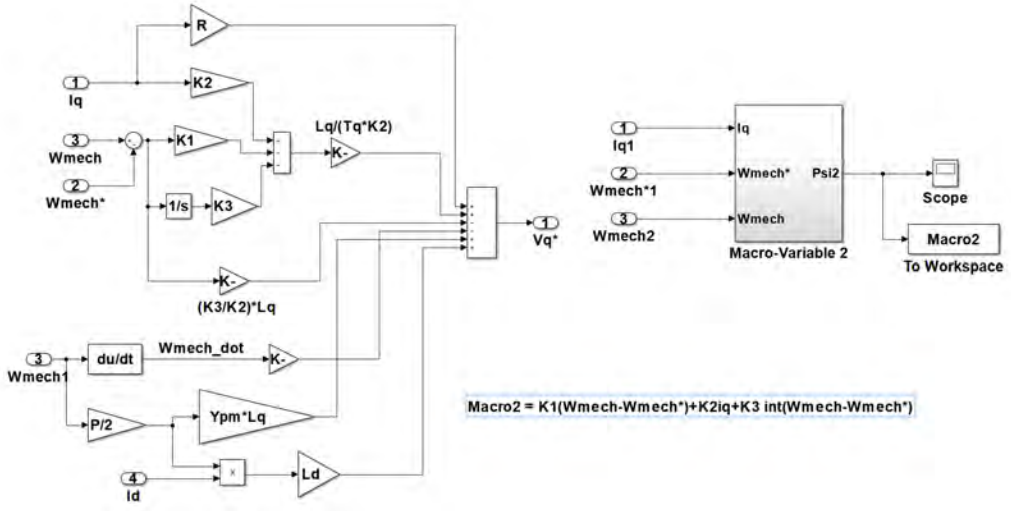

Figure B6: Contents of q-axis1 block

Vita

Andrew Adib was born in 1992 in Cairo, Egypt where he completed his education from Nefertari International Schools, Cairo. He graduated from the German University in Cairo (GUC) with a degree in Mechatronics Engineering. Post graduation, Andrew moved to Sharjah, UAE where he enrolled in the fully funded M.Sc. program of Mechatronics Engineering in the American University of Sharjah, where he worked as a graduate teaching assistant from January 2015 - May 2017. His research interests include AC motors, field oriented control, synergetic control and control of three phase inverters. He is also interested in computer programming.